DEVELOPMENT OF OPTIMAL ICE CLOUD OPTICAL PROPERTY MODELS FOR REMOTE SENSING APPLICATIONS

A Dissertation

by

YI WANG

Submitted to the Office of Graduate and Professional Studies of
Texas A&M University
in partial fulfillment of the requirements for the degree of

DOCTOR OF PHILOSOPHY

Chair of Committee,	Ping Yang
Committee Members,	Kenneth P. Bowman
	Anita Rapp
	Edward S. Fry
Head of Department,	Ramalingam Saravanan

December 2020

Major Subject: Atmospheric Sciences

ABSTRACT

This dissertation develops optimal cloud ice particle optical property models used for remotely sensed data from multi-angular satellite sensors. The optimal degree of surface roughness is inferred from Multi-angle Imaging SpectroRadiometer (MISR) measurements. The results show a latitudinal dependency in the optimal degree of ice particle roughness on a global scale. The optimal model for thick homogeneous clouds corresponds to more roughened ice particles in the tropics than in the extra-tropics. Furthermore, the inferred optimal ice particle roughness model is applied to the Moderate Resolution Imaging Spectroradiometer (MODIS) and MISR data to retrieve the optical thickness and effective radius of the ice cloud. The retrievals indicate a larger median optical thickness by 10.1% and a smaller median effective radius by 6.5% on the pixel-level, compared to the operational MODIS Collection 6 products.

In addition to these results, two algorithms are developed to infer the optimal ice particle model. The first algorithm is designed to work with a multi-angular sensor with polarimetric measurements and has been tested using data from a prototype aircraft-mounted sensor. The other algorithm uses multispectral measurements, specifically a combination of shortwave bands and thermal infrared (IR) bands, for performing retrievals of the optimal ice particle shape. This analysis includes a comparison of retrievals between multispectral and multi-angular techniques.

ACKNOWLEDGEMENTS

I would like to thank my committee chair, Dr. Yang, and my committee members, Dr. Bowman, Dr. Rapp, and Dr. Fry for their guidance and support throughout the course of this research. I also wish to acknowledge Dr. King, Dr. Di Girolamo, and Dr. Baum who gave me important guidance throughout this work.

I would especially like to thank Dr. Souichiro Hioki for his help in my research and study. I am grateful to my group members, especially Dr. Bingqiang Sun, Dr. Guanglin Tang, Dr. Chia-Pang Kuo, Dr. Masanori Saito, Dr. Guanglang Xu, Dr. Tong Ren, Dr. Jiachen Ding, Mr. Adam Bell, Mr. Jeffrey Mast, Mr. Jinjun Liu, and Mr. JiAn Wei, for all their help on both my research and my life. I would like to thank Dr. Steven Schroeder for his proofreading and many suggestions in the past years. Thanks also go to my friends and colleagues and the department faculty and staff for making my time at Texas A&M University a great experience.

I would like to thank my family for their love throughout my life. Finally, thanks to my wife Li Su for the loving support and patience she given me all these years.

During the pandemic, I hope everyone stays safe and well.

CONTRIBUTORS AND FUNDING SOURCES

The work was supported by a dissertation committee consisting of Professors Ping Yang, Kenneth P. Bowman, and Anita Rapp of the Department of Atmospheric Sciences, and Professor Edward S. Fry of the Department of Physics.

The research effort reported in this dissertation was partly supported by NASA Grants NNX15AQ25G, and the endowment funds related to the David Bullock Harris Chair in Geosciences at the College of Geoscences, Texas A&M University.

The computations were conducted at the Texas A&M University Supercomputing Facility. The authors thank the NASA Langley Research Center Atmospheric Sciences Data Center for providing MISR data (https://earthdata.nasa.gov/eosdis/daacs/asdc), the NASA LAADS system for providing MODIS atmosphere products (https://ladsweb.modaps.eosdis.nasa.gov), NASA Airborne Science Program for providing AirMSPI data, and the European Centre for Medium-Range Weather Forecasts (ECMWF) for providing Interim Re-Analysis (ERA-Interim) products.

TABLE OF CONTENTS

Page

ABSTRACT ii

ACKNOWLEDGEMENTS iii

CONTRIBUTORS AND FUNDING SOURCES iv

TABLE OF CONTENTS v

LIST OF FIGURES vii

LIST OF TABLES xi

1. INTRODUCTION 1

2. INFERENCE OF AN OPTIMAL ICE PARTICLE MODEL THROUGH LATITUDINAL ANALYSIS OF MISR AND MODIS DATA 9

- 2.1. Introduction 10
- 2.2. Data and Methods 13
  - 2.2.1. Satellite Data 13
  - 2.2.2. Ice Particle Model 15
  - 2.2.3. Look-Up Table Approach 19
  - 2.2.4. The SAD Method 20
- 2.3. Results 22
  - 2.3.1. Sampling Scattering Geometry Characteristics 22
  - 2.3.2. Latitudinal Variations in Consistency between Ice Models and Observations 24
- 2.4. Discussion 39
- 2.5. Summary and Conclusion 43

3. ICE CLOUD OPTICAL THICKNESS, EFFECTIVE RADIUS, AND ICE WATER PATH INFERRED FROM FUSED MISR AND MODIS MEASUREMENTS BASED ON A PIXEL-LEVEL OPTIMAL ICE PARTICLE ROUGHNESS MODEL 45

- 3.1. Introduction 46
- 3.2. Data and Methods 48
- 3.3. Results and Discussions 60

3.3.1. Global statistics of the optimal ice model for different cloud regimes 60
3.3.2. Retrievals with the optimal ice model 68
3.3.3. Seasonal Cycles of Retrievals and its Potential Implications.....73
3.4. Summary 79

4. REMOTE SENSING ICE PARTICLE MODEL FOR CIRRUS CLOUDS: METHODOLOGY AND VIEWING ANGLE DEPENDENCE IN RETRIEVALS USING AIRBORNE MULTI-ANGLE POLARIZATION MEASUREMENTS.....81

4.1. Introduction 82
4.2. Methodology 84
4.2.1. Ice Habit Models 84
4.2.2. Algorithm 87
4.3. Case Study.....93
4.3.1. Observations 93
4.3.2. Inference of ice particle shape.....97
4.4. Summary and Conclusions.....104

5. THE RETRIEVALS OF ICE CLOUD OPTICAL THICKNESS USING MULTI-ANGULAR AND MULTI-SPECTRAL TECHNIQUES.....106

5.1. Introduction 106
5.2. Data and Methods 107
5.2.1. Thermal infrared retrievals.....107
5.2.2. Multi-angle retrievals 107
5.2.3. Shortwave retrievals.....109
5.2.4. Data selection 110
5.2.5. Ice model 110
5.3. Results and discussions 111

6. CONCLUSIONS.....121

REFERENCES.....124

LIST OF FIGURES

Page

Figure 2.1 The phase functions of an aggregate of eight randomly attached hexagonal particles with an effective radius of 30 μm for six different degrees of surface roughness (σ2): 0.001 (R0001), 0.03 (R003), 0.14 (R014), 0.5 (R05), 1.0 (R10), and 3.5 (R35). The asymmetry factor (g) of each ice model is listed in the legend. The Moderate Resolution Imaging Spectroradiometer (MODIS) Collection 6 ice particle model (MC6 model) is the same as the R05 model here. The phase functions are at the wavelength of 0.86 μm. 18

Figure 2.2 Multi-angle Imaging SpectroRadiometer (MISR) camera (a) names and (b) normalized frequency of occurrences as a function of scattering angle and latitude on the four December solstice days (2012–2015) from the MISR-MODIS fused datasets over ocean. (c) The median value of the solar zenith angle (SZA) as a function of latitude on the same dates. 23

Figure 2.3 (a) The residual sum of squares of mean spherical albedo differences value (χ2) using the R0001, R003, R014, R05, R10, and R35 ice particle models on December solstices from 2012 to 2015. The dotted curve (and top scale) is the median SZA as a function of latitude. (b) The residual sum of squares of mean spherical albedo differences value using each corresponding model minus the residual sum of squares of mean spherical albedo differences value using the R05 ice particle model as a function of latitude.....26

Figure 2.4 The median value of all spherical albedo differences in latitude-scattering angle bins on December solstices from 2012 to 2015 using (a) R0001, (b) R003, (c) R014, (d) R05, (e) R10, and (f) R35 ice particle models. The dashed and solid lines correspond to solar zenith angle (SZA) 50° and 30°, respectively. 28

Figure 2.5 The variations of median spherical albedo differences values with latitude and scattering angle computed from a synthetic dataset generated with the R05 model (a, b), the R10 model (c, d), and the R35 model (e, f), and then retrieved using the LUTs with the other two models. 30

Figure 2.6 The median spherical albedo differences values for ranges of cloud optical thickness as a function of cloud heterogeneity index on December solstices from 2012 to 2015 stratified by (from left to right) cloud optical thickness bins of 0–3, 3–8, 8–16, and 16–64; and (from top to bottom) cloud heterogeneity index bins of 0–0.4, 0.4–1.6, 1.6–3.2, and 3.2–15. 33

Figure 2.7 The same as Figure 2.3 but computed for thick homogeneous clouds only. (a) The χ2 using the R0001, R003, R014, R05, R10, and R35 ice particle

models on December solstices from 2012 to 2015. The dotted curve (and top scale) is the median SZA as a function of latitude. (b) The $\chi 2$ value using each corresponding model minus the $\chi 2$ value using the R05 ice particle model as a function of latitude. 36

Figure 2.8 The same as Figure 2.4 but computed for thick homogeneous clouds only. The spherical albedo differences value in latitude-scattering angle bins on December solstices from 2012 to 2015 using (a) R0001, (b) R003, (c) R014, (d) R05, (e) R10, and (f) R35 ice particle models. The dashed and solid lines correspond to SZA 50° and 30°, respectively. 38

Figure 3.1 The phase functions of the MODIS Collection 6 (MC6) ice cloud model consisting of aggregate columns having an effective radius of 30 μm for 12 different degrees of surface roughness (σ^2) at 0.86 μm. The asymmetry factor (g) of each roughness value is also listed in the inset panel. 52

Figure 3.2 The normalized frequency of scattering angle sampled by three MISR cameras (i.e., AA, AN, and AF) for the entire measurements in 2013 between 60°N and 60°S. 54

Figure 3.3 The schematic data flowchart in the retrieval system. 57

Figure 3.4 The response of the retrieval system based on analysis of synthetic data for each degree of roughness (abscissa) with (a) 0.5% noise, and (b) 0.1% noise, as shown in a distribution of the roughness parameter (ordinate). The values in each bin are the fractions for each degree of roughness; the values in each column sum to 1 59

Figure 3.5 The normalized probability density distributions of four ice cloud property variables over the ocean: (a) ice cloud optical thickness (τ), (b) cloud particle effective radius (R_{eff}), (c) cloud heterogeneity index (H_σ), and (d) cloud top temperature. 61

Figure 3.6 The percentages of retrieved best-fit ice particle roughness models are shown for ranges of four ice cloud property variables over the ocean: (a) ice cloud optical thickness (τ), (b) cloud particle effective radius (R_{eff}), (c) cloud heterogeneity index (H_σ), and (d) cloud top temperature. The magenta curve shows the normalized probability of the number of pixels in every bin. 63

Figure 3.7 The standard deviations (in quadrature) between measured reflectance and model reflectance (χ^2) obtained using the optimal model and MC6 model for (a) ice cloud optical thickness (τ), (b) effective radius (R_{eff}), (c) cloud heterogeneity index (H_σ), and (d) cloud top temperature. 66

Figure 3.8 (a) The proportion of ice cloud pixels, and (b) the median cloud heterogeneity index (H_σ) value (solid is median and dashes are upper and lower quartiles) as a function of cloud top temperature. 70

Figure 3.9 The median retrieved ice cloud optical thickness (τ), cloud particle effective radius (R_{eff}), and ice water path using the optimal model and MC6 model over the range of values for the cloud heterogeneity index (H_σ) and cloud top temperature. 72

Figure 3.10 The annual cycles (monthly averages in 2013) of retrieved ice cloud optical thickness (τ), cloud particle effective radius (R_{eff}) and ice water path using the optimal model and MC6 model averaged over the tropics (0-30° latitude) and the mid-latitudes (30°-60° latitude) for both hemispheres. 75

Figure 3.11 The seasonal normalized frequencies of retrieved ice cloud optical thickness (τ) and cloud particle effective radius (R_{eff}) obtained from the optimal model and MC6 model. The results are averaged globally for each season (MAM: Mar-May, JJA: Jun-Aug, SON: Sep-Nov, and DJF: Dec-Feb). 77

Figure 4.1 The a) phase function and b) P12/P11 phase matrix elements as functions of scattering angle for 8 ice particle models and 3 liquid water models with different effective radii (R_{eff} = 4 μm, 8 μm, and 16 μm) used in this study. The 8 ice particle models are 4 ice particle habits, which are bullet rosette (rosett in the figure), 10 plates aggregate (plate), solid hexagonal column (column), and 8 hexagonal columns aggregate (hexagr) with smooth surface (m) and roughened surface (r) particles computed separately for each habit. 86

Figure 4.2 The a) total reflectivity and b) polarized reflectivity as functions of cloud optical thickness for ice particle models used in this study. The geometry angles (solar zenith angle of 51.5°, viewing zenith angle of 0°, and relative azimuthal angle of 130°) of the AirMSPI nadir camera (000N) in the chosen case study are assumed here. 89

Figure 4.3 The flow chart for inferring optimal ice particle models of cirrus clouds in this study 91

Figure 4.4 The geometry angle range of the sun and AirMSPI camera views in the selected case in this study. The azimuth angle range (solar azimuth angle plus 180° or viewing azimuth angle) and zenith angle (solar zenith angle or viewing zenith angle) are plotted clockwise from north (0°) and radial distance (angle from vertical), respectively. The color bar shows the solar scattering angle for each pixel. 96

Figure 4.5 The proportion of inferred ice particle shapes in different camera selection cases using a) total reflectivity and b) polarized reflectivity. 99

Figure 4.6 The inconsistency between model reflectivity with inferred ice particle models and measurement from a) total reflectivity and b) polarized reflectivity, for each different camera selection case. 103

Figure 5.1 Comparison of the retrieved optical thickness from applying the split window method in shortwave and thermal IR bands, assuming each ice particle model, (a) MC6 model, (b) Two Habit Model. 113

Figure 5.2 The deviation of spherical albedo values from the average over all scattering angles (spherical albedo difference) with assuming ice particle model (a) MC6 and (b) THM. 115

Figure 5.3 The proportions of pixels where the MC6 and THM ice particle models produce the best fitting optical thickness retrievals with both multi-spectral and multi-angular retrieval methods. 117

Figure 5.4 The histogram of cloud optical thickness for different cloud regimes (top row: optical thickness from 0 to 5, and bottom row: cloud top from 5000 to 10000 m) from (left panels) multi-spectral and (right panels) multi-angular retrieval methods. 119

LIST OF TABLES

Page

Table 4.1 The camera selection in each group. Cameras with a plus sign are included in a group, and with a minus sign are not included. 98

1. INTRODUCTION

Covering about 20% of the world, ice clouds exert a significant influence on the global energy budget and climate system feedbacks (Liou, 1986; Stephens et al., 1990; Yang et al., 2018). The two primary methods for performing a quantitative analysis of ice cloud properties are remote sensing and climate/weather numerical simulations or called general circulation model (GCM). Most contemporary GCM and remote sensing techniques compute radiative properties of ice clouds based on ice particle assumptions.

A GCM normally simulates cloud ice particles by parameterization, often by describing ice particle characteristics in a volume using 3 scattering parameters (Hioki, 2018). These 3 parameters are single scattering albedo, extinction cross section, and asymmetry factor (also called asymmetry parameter). Compared to GCM, remote sensing applications to interpret satellite images replace the asymmetry factor with the phase function. The phase function describes the angular distribution of scattered radiation energy in terms of the scattering angle (such as the angle by which incident sunlight reflects from the cloud to the satellite sensor). The phase function integrated over all scattering angles is the asymmetry factor. So, the phase function includes scattering information for all viewing directions, but the asymmetry factor just indicates the ratio of forward-scattered to backward-scattered light (van de Hulst, 1957). A GCM can use the asymmetry factor instead of the phase function because a GCM normally focuses on a directional flux calculation. However, the remote sensing approach cannot consider only one direction because as the satellite orbits, the viewing scattering geometry constantly

changes and all the scattering geometries of sensors need to be computed. So the phase function is needed.

Compared to a GCM, remote sensing measurements have higher spatial resolution and include information from more scattering geometries, which potentially leads to less uncertainty in cloud retrievals. Thus, the remote sensing technique is very popular for studying actual ice cloud properties.

Early ice particle model applications in remote sensing retrievals assumed that an ice particle has a spherical shape (Houghton and Hunt, 1971), which can be calculated by Mie theory scattering calculations. However, field and lab measurement studies (Heymsfield et al., 2013; Bailey and Hallett 2009) show that ice cloud particle shapes are rarely spherical but have complex shapes. With the development of scattering calculations and modern high-performance computing techniques, the cloud ice particle model becomes more complex to better mimic the shapes found in experimental sampling in recent years.

In current satellite operational products, various cloud ice particle models are used. An inhomogeneous hexagonal ice particle model (IHM) is used to process data from the POLDER (POLarization and Directionality of the Earth's Reflectance) sensor onboard the PARASOL (Polarization & Anisotropy of Reflectances for Atmospheric Sciences coupled with Observations from a Lidar) satellite. The IHM model is a hexagonal column with air bubbles inside. The MODIS (Moderate Resolution Imaging Spectroradiometer) Collection 6 products use a hexagonal column aggregate model, which is an aggregate composed of eight hexagonal columns with a specified degree of surface roughness

(Platnick et al., 2015). The Clouds and the Earth's Radiant Energy System (CERES) Edition 5 selects a two-habit model, a mixture of two ice particle shapes with proportions of each shape varying with atmospheric conditions (Loeb et al., 2018).

These current mainstream ice particle models used in satellite operational products all assume a plane-parallel homogeneous cloud with no variation in the ice particle shape. However, ice cloud particle shapes are more complex in a cloud and are affected by temperature and supersaturation variations (Heymsfield et al., 2013; Bailey and Hallett 2009), which indicates that the representation of these clouds in satellite retrieval algorithms is primitive so far. This inconsistency between the ice particle model in a simulation and actual ice particle shapes causes large uncertainties of ice cloud properties in remote sensing retrievals and their effects on weather and climate studies and GCM simulations. Therefore, understanding the uncertainties and developing an optimal ice particle model are necessary for studies of ice clouds in remote sensing and weather and climate numerical simulations.

Moreover, the selection of an appropriate ice particle model is critical for retrieving cloud optical thickness (τ) and cloud particle effective radius (R_{eff}). These two important ice cloud radiative and microphysical properties primarily determine the shortwave ice cloud radiative properties and therefore exert a significant role in modulating the Earth's radiation budget (Liou, 1986; Stephens et al., 1990; Yang et al., 2018). The precise estimation of these two cloud properties is fundamental in the study of parameterizing and constraining cloud radiative effects in GCMs and is important for understanding physical mechanisms of cloud radiative variability and the hydrological

cycle. Therefore, the selection of an appropriate ice particle model and subsequent generation of the corresponding bulk single-scattering properties are very important to the implementation of ice cloud property retrievals and, subsequently, to the assessment of the ice cloud radiative forcing effect (Mishchenko et al., 1996; Baran et al., 2009; Yang et al., 2015; Loeb et al., 2018).

The most straightforward method to develop a realistic ice particle model shape and size distribution is to use in situ aircraft measurements to sample ice particles in the clouds. However, it is already known that lab generated and in situ aircraft measured ice particle shapes strongly depend on local environmental variations, such as wind speed and relative humidity. Also, the instrument may shatter or otherwise damage the particles so the shape and size distributions are inaccurate (Heymsfield et al., 2013; Bailey and Hallett 2009). Furthermore, in situ aircraft measurements have been taken predominantly in mid-latitudes. Because many ice cloud environments have never been adequately sampled, using satellite observations to investigate ice particle shapes globally is necessary.

A satellite retrieval infers ice cloud properties from a set of remote sensing measurements, generally multiple images (in different spectral bands; each band is usually referred to as a channel) of a swath or other area as a satellite passes overhead. This study uses spectral bands in the visible, infrared, and microwave (radio) ranges. An “image” is composed of pixels (scan spots) whose sizes depend on the instrument resolution. Each pixel records the amount of energy received from each scan spot in a specific spectral band, which is transmitted in digital form. Extracting the information from these pixels in the satellite images is called satellite retrieval.

Typically, an inversion program is applied to remote sensing data by performing a radiative transfer calculation. Most radiative transfer formulas are stated in the "forward" form, where from a set of physical assumptions about a viewed location (such as atmospheric profile, particle sizes, particle shapes, particle types [ice, water, dust, etc.], sun angle, and satellite viewing angle), the amounts of energy (generally radiances) are computed in the instrument spectral bands. However, a satellite view obtains the radiances (a single instrument may make millions of radiance measurements per hour), and it is desired to obtain the physical conditions that produced the observed radiances. Therefore, an "inverse" radiative transfer calculation, also called a retrieval, is performed to infer that physical condition.

One method to retrieve ice particle shapes on the pixel scale is to obtain information using multi-angle satellite measurements. Unlike a common cross-track scanning sensor such as MODIS, a multi-angle imaging satellite sensor detects reflectivities from the same target cloud at different satellite viewing angles. The different geometries provide measurements for a given location over a wide scattering-angle range, which captures more ice cloud scattering information about clouds. Therefore, this scattering information from a multi-angle sensor provides a great opportunity to distinguish various ice particle shapes.

Doutriaus-Boucher et al. (2000) developed the spherical albedo differences (SAD) method by using multi-directional observations from the POLDER sensor, which contains a single camera viewing the same region from different angles below the satellite orbit. The study found that the inhomogeneous hexagonal monocrystal (IHM) ice particle model

is more appropriate than a fractal polycrystal to analyze observations of ice clouds over oceans. Briefly, the SAD method compares the scattering properties computed with different ice particle shape models to the scattering signals from all of the cameras to evaluate which ice particle shape model provides the best consistency to the multi-angle measurements. This algorithm was well tested by studies aimed at testing cloud particle models and their scattering properties using the POLDER sensor (Doutriaus-Boucher et al., 2000).

POLDER operated from December 2004 until it was decommissioned in December 2013, but another multi-angle sensor, MISR (Multi-angle Imaging SpectroRadiometer, is still observing. MISR, onboard NASA's Terra satellite platform, has 9 cameras each having a different viewing zenith angle (Diner et al., 1998). One of the advantages of MISR data is a long dataset. Another advantage of MISR compared to POLDER is that both MODIS and MISR are aboard the Terra satellite. With both instruments, other cloud optical properties including cloud optical thickness and effective radius are also retrieved, and evaluating MODIS products from multi-angular measurement is available. Specifically, fusing MISR and MODIS measurements could first identify the best ice particle shape using multi-angle imaging measurements from MISR, and then retrieve the other cloud properties using visible and near infrared measurements from MODIS to be consistent with the identified best ice particle shape. Therefore, investigating ice cloud properties by applying the SAD method to MISR measurements is helpful and necessary.

Another method used in the evaluation of the ice particle model is based on multiple spectral channel measurements. For retrieving ice cloud properties, shortwave bands and thermal infrared (IR) bands have been extensively used. It is essential for an ice crystal model to provide consistent cloud property retrievals based on these shortwave bands and thermal IR bands. Because ice crystal shape has a smaller impact on retrievals in the thermal IR spectral regime than in the shortwave regime, the differences of cloud property retrievals based on different ice crystal models in the IR bands are smaller than in the counterparts' shortwave bands. An optimal ice model must lead to consistency in cloud retrievals between both shortwave bands and thermal IR bands. By checking this consistency between these two bands, the ice particle shape model is also able to be tested in satellite retrievals.

This doctoral project is aimed at validating existing ice particle models using these two methods from satellite-based remote sensing measurements and understanding the uncertainties in satellite products of ice cloud properties by assuming different ice particle models in retrievals. In addition, the effect of cloud inhomogeneity or the 3-D effect in satellite retrievals is discussed. This difficult-to-quantify variation in appearance of a cloud viewed from the side may introduce bias in the cloud property retrievals. Finally, an improved satellite retrieval technique involving a polarization approach is attempted.

This dissertation is structured as follows. Section 2 applies multi-angle image techniques to MISR measurements to validate ice particle models and analyze the geospatial distribution of optimal ice particle models. Section 3 further investigates the uncertainties of retrieved ice cloud properties introduced when different ice particle

models are assumed. Section 4 introduces a remote sensing retrieval prototype by using polarization to validate ice particle models. Section 5 presents the optimal ice particle model inferred by multi-channel techniques and compares the results with multi-angle techniques. A brief summary is given in Section 6.

2. INFERENCE OF AN OPTIMAL ICE PARTICLE MODEL THROUGH LATITUDINAL ANALYSIS OF MISR AND MODIS DATA*

The inference of ice cloud properties from remote sensing data depends on the assumed forward ice particle model, as they are used in the radiative transfer simulations that are part of the retrieval process. The Moderate Resolution Imaging Spectroradiometer (MODIS) Collection 6 (MC6) ice cloud property retrievals are produced in conjunction with a single-habit ice particle model with a fixed degree of ice particle surface roughness (the MC6 model). In this study, we examine the MC6 model and five other ice models with either smoother or rougher surface textures to determine an optimal model to reproduce the angular variation of the radiation field sampled by the Multi-angle Imaging Spectroradiometer (MISR) as a function of latitude. The spherical albedo difference (SAD) method is used to infer an optimal ice particle model. The method is applied to collocated MISR and MODIS data over ocean for clouds with temperatures ≤233 K during December solstice from 2012–2015. The range of solar zenith angles covered by the MISR cameras is broader at the solstices than at other times of the year, with fewer scattering angles associated with sun glint during the December solstice than the June solstice. The results suggest a clear latitudinal dependence in an optimal ice particle model, and an additional dependence on the solar zenith angle (SZA) at the time of the observations. The

* Edited and reprinted with permission from "Inference of an optimal ice particle model through latitudinal analysis of MISR and MODIS data" by Yi Wang, Souichiro Hioki, Ping Yang, Michael D. King, Larry Di Girolamo, Dongwei Fu, and Bryan A. Baum, 2018. Remote Sensing 10, no. 12 (2018): 1981. Copyright [2018] by MDPI AG

MC6 model is one of the most optimal models on the global scale. In further analysis, the results are filtered by a cloud heterogeneity index to investigate cloudy scenarios that are less susceptible to potential 3D effects. Compared to results for global data, the consistency between measurements and a given model can be distinguished in both the tropics and extra-tropics. The SAD analysis suggests that the optimal model for thick homogeneous clouds corresponds to more roughened ice particles in the tropics than in the extra-tropics. While the MC6 model is one of the models most consistent with the global data, it may not be the optimal model for the tropics.

2.1. Introduction

The inference of ice cloud optical thickness τ and effective particle size reff from passive spaceborne radiometric measurements requires an assumed forward ice particle model that provides the bulk scattering and absorption properties. Based on the ice particle model, look-up tables (LUTs) for cloud property retrieval are generated by using radiative transfer simulations. The LUTs provide the transmission, scattering, and emission characteristics as functions of, for example, optical thickness and the sun-satellite geometric configuration (e.g., solar zenith angle, viewing zenith angle, and relative azimuth angle). In practice, the LUTs are applied to global satellite measurements so the assumed ice particle model should be applicable to a large spatial domain.

There are numerous constraints on choosing an ice particle model for global data processing. For operational retrievals, the Clouds and the Earth's Radiant Energy System (CERES) and Moderate Resolution Imaging Spectroradiometer (MODIS) adopted single-habit models. Specifically, CERES Edition 4 adopted a severely roughened hexagonal

column model, whereas MODIS Collection 6 (MC6) adopted a model with aggregates consisting of severely roughened columns (Holz et al., 2016; Platnick et al., 2017). In addition, a Voronoi particle model was suggested for use with geostationary satellite data (Letu et al., 2016) and the inhomogeneous hexagon model (IHM) was defined for the Polarization and Directionality of the Earth's Reflectances (POLDER) on the Polarization and Anisotropy of Reflectances for Atmospheric Sciences coupled with Observations from a Lidar (PARASOL) satellite ice cloud property retrievals. Multiple models are not generally adopted by an individual team to avoid potential discontinuities in retrievals resulting from the transition between models.

Recent research suggests that the ice particle models should have a substantial degree of surface roughness (Cole et al., 2014; Hioki et al., 2016), or at least some amount of inhomogeneity. The IHM model employs a different approach than surface roughening to increase photon dispersion by including air bubbles. Generally speaking, the surface roughness or inhomogeneity of ice crystals particles tends to smooth the phase function and results in a relatively low asymmetry factor at solar wavelengths. Because the phase function is fundamental to the remote sensing of global cloud properties, a better understanding of the appropriate degree of ice particle surface roughness for a given ice particle habit is important for improving the consistency of the retrievals based on observations by different sensors.

The overarching goal of this study is to identify an appropriate degree of surface roughness adopted for ice particle models through the use of collocated Multi-angle Imaging Spectro Radiometer (MISR) and MODIS data. Compared to a satellite sensor

with only a nadir-viewing camera, multi-angle cameras measure the reflectance of a cloud over a wide range of scattering angles as the satellite passes over a location. Because different physical ice particle habits lead to significantly different angular distributions of reflectance simulated at the top of the atmosphere (TOA), comparing theoretical radiative transfer simulations with multi-angle camera measurements provides valuable constraints on the particle morphology. Several previous studies (Doutriaux-Boucher et al., 2000; McFarlane et al., 2005; Sun et al., 2006; Xie et al., 2014) attempted to infer the predominant atmospheric ice particle habits based on multi-angle satellite measurements. In particular, the spherical albedo difference (SAD) method (Doutriaux-Boucher et al., 2000) was developed to quantify the comparison between spherical albedo values computed with an assumed ice particle model and their counterparts derived from multi-angle satellite measurements. Furthermore, this algorithm was used to validate cloud particle models and their single-scattering properties (Baran et al., 2001; Baran and Labonnote 2006; Baran and Labonnote 2007).

This study assesses the latitudinal dependence of six ice cloud models based on the application of the SAD method to the fused MISR and MODIS 0.86-μm channel data. Chapter 2.2 describes the satellite measurements and the SAD method. Chapter 2.3 presents the results, including the latitudinal consistency of ice particle models with MISR observations via the SAD method, including analyses under different cloud heterogeneity conditions. Chapter 2.4 discusses potential uncertainties of the results. A summary and conclusions are given in Chapter 2.5.

2.2. Data and Methods

In the SAD method, the spherical albedo difference value (A_{diff}) is computed for every pixel in the spatial domain of interest by comparing theoretical radiances and the measured counterparts. To compute A_{diff} values for ice clouds based on MISR observations, we apply a look-up table approach in this study.

2.2.1. Satellite Data

In this study, we use collocated datasets obtained by the MISR and MODIS instruments onboard the Terra satellite during December solstices from 2012–2015. The details of collocation are described by Liang et al. (Liang et al., 2009) and Liang and Di Girolamo (2013). The MODIS product at 1-km resolution and all MISR camera views are co-registered to the MISR nadir camera (AN) pixel positions to generate a 1.1-km resolution fused dataset. Measured radiances used in this study are from the MISR observations, and the MC6 products are used to classify cloud pixels.

MISR uses nine cameras to measure radiance along the satellite track (Diner et al.,1998; Diner et al., 2002). In addition to one nadir-viewing camera (AN), four cameras (AF, BF, CF, DF) point forward and four cameras (AA, BA, CA, DA) point aft along the orbital track. The viewing zenith angles (VZAs) for the AA/AF, BA/BF, CA/CF, DA/DF cameras are 26.1°, 45.6°, 60.0°, and 75.0°, respectively. The three near-nadir-viewing cameras (AA, AN, AF) are used to avoid potential 3D effects due to large VZAs. Each camera measures radiances in four narrow spectral bands. The band centered at 0.86 μm is selected because this channel is less affected by ozone and ice absorption. The measured radiances are converted to reflectances ($\widetilde{R}$) as follows:

$$\tilde{R}(P, \mu_0, \mu, \phi_0, \phi) = \frac{\pi \cdot d^2}{\mu_0 \cdot E_0} \tilde{I}(P, \mu_0, \mu, \phi_0, \phi) \quad (2.1)$$

where $\tilde{I}$ is the measured radiance, P is the phase function, μ_0 is the cosine of solar zenith angle (SZA), μ is the cosine of VZA, ϕ_0 is solar azimuthal angle, ϕ is viewing azimuthal angle, d is Sun-Earth distance in astronomical units (AU), and E_0 is the solar irradiance at 1 AU.

To avoid cloud pixels containing liquid phase particles, pixels are selected by applying two criteria based on the MODIS products: (1) cloud phase identified with infrared channels as ice; and (2) cloud top temperature lower than 233 K. To avoid potential effects of land reflectance and associated complexity for radiative transfer computations, observations are limited to an ocean surface. All MISR camera measurements are removed that have sun glint angles smaller than 35°, or specifically satellite-viewing directions within a 35° cone around the sunlight direction. Avoiding sun glint reduces the number of selected camera views (n_c) for some pixels. Moreover, pixel locations are restricted to 60° N–60° S to avoid the effects of sea ice since an ice-free ocean surface is assumed.

The cloud optical thickness (τ) and cloud heterogeneity index (H_σ) from MODIS products are used to stratify clouds for statistical analysis. The MODIS cloud optical thickness product is not used elsewhere in this study, such as in Sections 2.3 and 2.4. H_σ estimates the degree of cloud horizontal heterogeneity, which is computed with the 4 × 4 sub-pixel array composing a MODIS 1-km pixel (MODIS has two channels at 0.25-km

resolution). The H_σ is defined as the standard deviation divided by the mean measured reflectance for such a pixel (Platnick et al., 2018).

SZA generally increases with increasing latitude. To reduce differences in the SZAs at the same latitude, data are collected and analyzed on nearly the same date for four years. Due to the solar–earth–satellite viewing geometry, the range of SZA values covered by the MISR cameras is broader at the solstices than at other times of the year, and fewer scattering angles are associated with sun glint on the December solstice in comparison to the June solstice. In other words, using data on the December solstice provides information over the broadest scattering angle range with fewer sun glint issues. For these reasons, this study uses data during December solstices from 2012–2015, except 2013. In 2013, we selected 25 December 2013, not the solstice, to avoid complexities caused by a cyclonic storm over the Indian Ocean. The specific dates chosen for detailed analyses are December 21, 2012, December 25, 2013, December 21, 2014, and December 22, 2015.

2.2.2. Ice Particle Model

Before applying the SAD method to the MISR datasets, LUTs are prepared by assuming specific ice particle models. Six ice particle models are employed in this study to examine the consistency between the theoretical radiances and the MISR observations at various latitudes.

The MC6 roughened hexagonal ice aggregate model is used in the MODIS Collection 6 operational products (Platnick et al., 2015), which assume ice cloud particles to be an ensemble of randomly oriented aggregates. Each aggregate is composed of eight hexagonal columns with a fixed degree of surface roughness σ2 = 0.5. The roughness

parameter σ2 in the light scattering calculations is defined as the standard deviation of a two-dimensional Gaussian distribution for the tilting of a particle facet (Yang and Liou, 1998). The standard deviation of this roughness parameter σ is approximately equivalent in value to the roughness parameter δ defined by Macke et al. (1996) (Neshyba et al., 2013; Geogdzhayev et al., 2016). A higher degree of roughness means a higher probability density of strongly distorted surfaces. Detailed descriptions of the ice particle habit and associated degree of surface roughness are discussed by Yang and Liou (1998) and Yang et al. (2013). In general, the ice particle phase function at scattering angles between 50° and 175° becomes more featureless with an increasing degree of surface roughness (Figure 2.1) for six models assuming a range of surface roughness of σ2 = 0.001, 0.03, 0.14, 0.5, 1.0, and 3.5 (hereafter, R0001, R003, R014, R05, R10, and R35, respectively). Note that the MC6 model corresponds to the R05 model. Both the ice particle habit and ice particle surface roughness can modify the single-scattering properties (Yang et al., 2018), although other factors are also important, such as particle impurities, internal fractures, and air bubbles. The asymmetry factor (g) for each model is also included in Figure 1. Among these selected models, the asymmetry factor decreases with an increasing degree of roughness until σ2 = 0.14, beyond which the asymmetry factor increases in even rougher models. Perhaps some of this behavior in the most severely roughened models could be a modeling artifact associated with the ray-tracing technique when it is applied to a very rough particle surface. Although the MC6 ice particle habit model has a better match to global satellite measurements than other ice particle habits (Holz et al., 2016; Cole et al., 2014; McFarlane and Marchand 2008), the “optimal” degree of ice particle surface

roughness for the MC6 ice model has not been studied rigorously yet. To test the degree of roughness used in MC6, we developed five other ice particle models using the MC6 ice particle habit, but with different degrees of ice particle surface roughness. The additional five degrees of roughness have different phase functions over the MISR observational range of scattering angles in comparison with the case of $\sigma 2 = 0.5$.

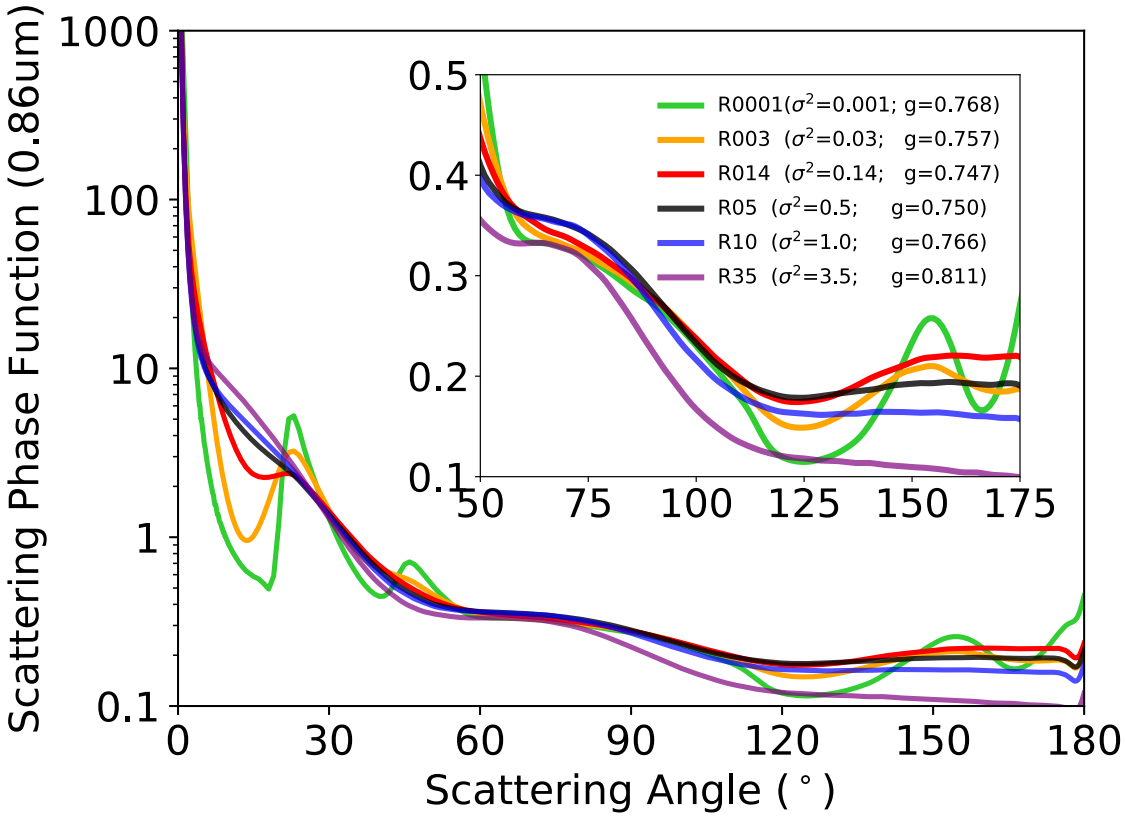

Figure 2.1 The phase functions of an aggregate of eight randomly attached hexagonal particles with an effective radius of 30 µm for six different degrees of surface roughness (σ2): 0.001 (R0001), 0.03 (R003), 0.14 (R014), 0.5 (R05), 1.0 (R10), and 3.5 (R35). The asymmetry factor (g) of each ice model is listed in the legend. The Moderate Resolution Imaging Spectroradiometer (MODIS) Collection 6 ice particle model (MC6 model) is the same as the R05 model here. The phase functions are at the wavelength of 0.86 µm.

2.2.3. Look-Up Table Approach

LUTs are developed separately for each ice particle model, i.e., R0001, R003, R014, R05, R10, and R35. For each ice cloud particle model, the LUTs are calculated using an adding–doubling radiative transfer model (Huang et al, 2015). The LUTs include model reflectances as a function of solar geometry, viewing geometry, and τ; the model reflectance R is equivalent to the reflectance $\tilde{R}$ from MISR measurements in Equation (2.1). The bulk scattering properties for each ice particle model are the ensemble-mean single-scattering properties integrated over a Gamma distribution with an effective variance of 0.1 and an effective radius of 30 μm. The reflectance at wavelength 0.86 μm is insensitive to the particle effective size due to weak ice absorption. Atmospheric molecular scattering is considered in the model, but aerosols are neglected. The ocean surface reflection is based on the Cox-Munk model (Cox and Munk 1954) with a wind speed of 10 m s^{-1}. The reflectance for each MISR camera is calculated by assuming a homogeneous cloud layer with a cloud-top pressure of 200 hPa. A sensitivity study shows that the effect of cloud-top pressure on retrievals is not substantial.

The R values can be integrated over μ and ϕ (viewing directions) to obtain the planetary albedo (A_{p}):

$$A_p(P, \mu_0, \phi_0, \tau) = \frac{1}{\pi} \int_0^{2\pi} \int_0^1 R(P, \mu_0, \phi_0, \tau) \cdot \mu \cdot d\mu \cdot d\phi \qquad 2.2)$$

The cloud spherical albedo, A_{s}, is the integration of A_p over all incident directions (μ_0, ϕ_0):

$$A_s(P,\tau) = \frac{1}{\pi}\int_0^{2\pi}\int_0^{1} A_p(P,\mu_0,\phi_0,\tau)\cdot\mu_0\cdot d\mu_0\cdot d\phi_0 \qquad 2.3)$$

By carrying out the integrals in Equations (2.2) and (2.3), R is converted to A_s for a given τ in conjunction with a specific ice particle model. LUTs are developed for each ice particle model and contain both R and the corresponding A_s as functions of τ.

2.2.4. The SAD Method

The SAD method for examining angular variations of ice particle phase functions is described by Doutriaux-Boucher et al. (2000) and C.-Labonnote et al. (2000), who applied this method to POLDER data. These studies found that A_s has a one-to-one relationship with τ for a given ice particle model (Doutriaux-Boucher et al., 2000), implying that there is a one-to-one theoretical relationship between A_s and $\tilde{R}$. Because R and A_s are provided in the LUTs, an $\tilde{R}$ value from each MISR camera measurement is used to search for the corresponding value of R in the LUTs. The associated A_s in the LUTs is identified as the retrieved cloud spherical albedo ($\widetilde{A_s}$) for this camera. This procedure is iteratively performed for every camera measurement to compute $\widetilde{A_s}$. Because only three near-nadir cameras are selected from a set of MISR measurements, one cloudy pixel may correspond to 3 $\widetilde{A_s}$ values.

Each MISR camera retrieves $\tilde{R}$ for a pixel at a different scattering angle (Θ). If an assumed ice particle model matches observations accurately over the range of three observed Θ values, the model R values would be equal to the observed $\tilde{R}$ values for every Θ. When τ is identical for all cameras, the same $\widetilde{A_s}$ could be obtained. Given that idealized

ice models may not fit a real cloud perfectly for every available Θ, there may be differences in the computed $\widetilde{A_s}$ values. A_{diff} is defined as the difference between the $\widetilde{A_s}$ of a selected camera and the mean of $\widetilde{A_s}$ averaged for the selected cameras for a given pixel:

$$[A_{diff}(P)]_i = [\tilde{A}_s(P)]_i - \frac{1}{n_c}\sum_{i=1}^{n_c}[\tilde{A}_s(P)]_i \quad (2.4)$$

where i is the camera index in the pixel and n_c is the total number of selected cameras in the given pixel. Because of the sun glint screening process, n_c is not necessarily 3. As defined in Equations (2.2) and (2.3), A_s does not depend on either solar or viewing geometries but solely on P for a given τ. Therefore, smaller absolute values of A_{diff} indicate better consistency between simulations and observations.

To identify an optimal ice particle model, the same procedure is applied to each pixel using all LUTs. The smallest A_{diff} value from the six LUTs is chosen as the optimal model for that pixel. Finally, to quantify the consistency between ice particle models with observations, the standard deviation of A_{diff} (χ^2) for each ice particle model in a given latitude bin is defined as follows:

$$\chi^2{}_{\sigma^2} = \sqrt{\frac{1}{(\sum_{k=1}^{n_b} n_R)}\sum_{k=1}^{n_b}\sum_{j=1}^{n_R}[(A_{diff})_{j,k}]^2} \quad (2.5)$$

where n_R is the total number of selected reflectances in a latitude-scattering angle bin and n_b is the total number of selected latitude-scattering angle bins in a particular latitude band.

2.3. Results

2.3.1. Sampling Scattering Geometry Characteristics

Figure 2.2a,b show the MISR camera names that are used and the normalized frequency of occurrences of Θ and latitude based on the four chosen December solstice days during 2012–2015 from the MISR-MODIS fused dataset over oceans. Due to the varying SZA with latitude and different VZAs of each MISR camera, the cameras provide reflectances at different Θ for a given pixel, and the Θ changes with latitude. The minimum available Θ is 76° and the maximum available Θ is 172° in these selected pixels. Because the daytime orbit of the Terra satellite is from north to south with an equator crossing time at 10:30 am, the forward camera measures at smaller Θ than the aft camera in the northern high latitudes. The three cameras primarily take measurements in the side and backward scattering directions. Note that the presence of arc-shaped strips in Figure 2.2a is a result of filtering out the pixels with sun glint. For the same reason, some bins in Figure 2.2b have no observations.

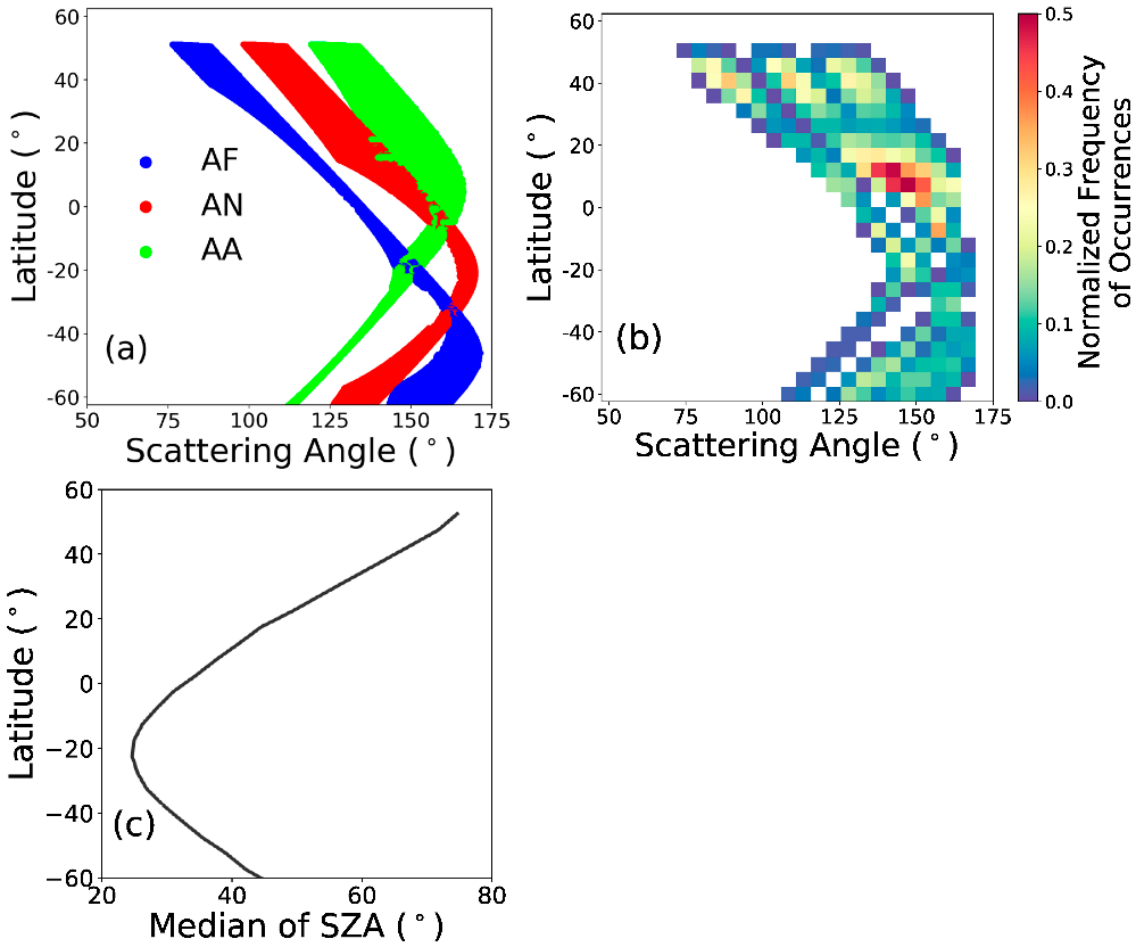

Figure 2.2 Multi-angle Imaging SpectroRadiometer (MISR) camera (a) names and (b) normalized frequency of occurrences as a function of scattering angle and latitude on the four December solstice days (2012–2015) from the MISR-MODIS fused datasets over ocean. (c) The median value of the solar zenith angle (SZA) as a function of latitude on the same dates.

The detected range of Θ changes with latitude, in large part due to changes in SZA, as shown in Figure 2.2c. The camera geometry discussed above causes the detected range of Θ variation with SZA. The narrowest range of scattering angle measurements occurs at the lowest SZA (~20° S), where no reflectances are measured at Θ < 140°. However, all reflectances are measured at Θ < 140° at the highest SZA (~50°–60° N). The latitudes where measurements are made at the largest Θ are different for each camera, but roughly speaking, all three cameras measure in side scattering to backscattering directions with increasing SZA. The frequencies of Θ observations also reveal latitudinal variations. When the SZA is low, the same scattering angles can be recorded by two cameras viewing the same pixel.

2.3.2. Latitudinal Variations in Consistency between Ice Models and Observations

2.3.2.1. Consistency of Models and to Measurements with Latitude

The quantity χ^2 in Equation (2.5) as a function of latitude for each particle model is shown in Figure 3a, and quantitative comparisons between the R05 and other models based on Equation (2.5) are displayed in Figure 2.3b. The χ^2 values for all models in the Northern Hemisphere are larger than in the Southern Hemisphere and decrease with latitude from north to south. The six χ^2 values are more similar in value to each other in the low latitudes than in the high latitudes of both hemispheres. Figure 2.3 shows that the R05 and R014 models have similar χ^2 values over the latitude range, and both models have lower χ^2 values than the other models in all latitudes. Note that these two models have lower g than the other models (Figure 2.1). However, the relationships between χ^2 and g are not simple. The R35 model has the highest g but has a lower χ^2 value than the

R0001 model in most latitudes. Also, the R0001 and R10 models have similar g values, but the consistency of A_{diff} results for the R0001 model is much less than in the case of the R10 model.

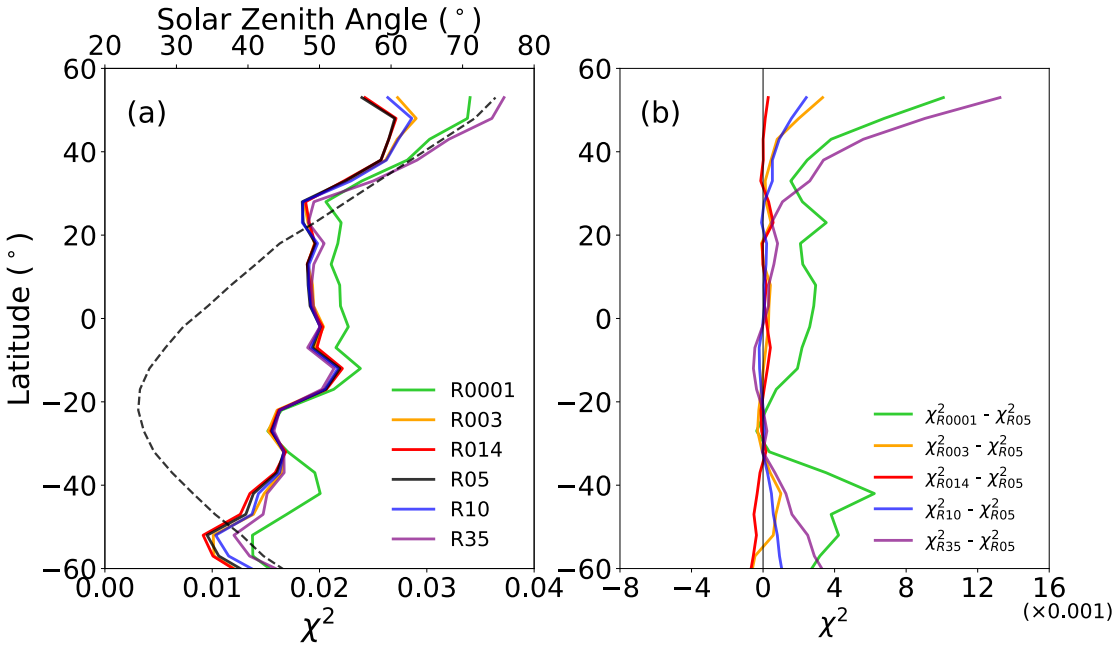

Figure 2.3 (a) The residual sum of squares of mean A_{diff} value (χ^2; see Equation (2.5)) using the R0001, R003, R014, R05, R10, and R35 ice particle models on December solstices from 2012 to 2015. The dotted curve (and top scale) is the median SZA as a function of latitude. (b) The residual sum of squares of mean A_{diff} value using each corresponding model minus the residual sum of squares of mean A_{diff} value using the R05 ice particle model as a function of latitude.

To better understand the contributions of A_{diff} to χ^2, Figure 2.4 shows the median value of A_{diff} (hereafter, A_{diff} indicates the median value in 5° × 5° latitude-Θ bins) on December solstices during 2012–2015. The variations of A_{diff} values more closely follow the changes in SZA. The axis of symmetry of A_{diff} is located at about 20° S, where there is a minimum in the Θ range. For SZA < 30°, the A_{diff} values computed with all six models display nearly the same pattern. The A_{diff} values are close to zero for most Θ, but slightly negative at the highest Θ (Θ~170°). As SZA increases, A_{diff} values are still close to zero when 30° < SZA < 50°. However, A_{diff} values become positive for the largest measurable Θ with an increasing degree of roughness and become negative for the smallest measurable Θ with a decreasing degree of roughness. At high latitudes (SZA > 50°), the A_{diff} values broadly become highly positive or negative as shown in Figure 2.4a,b,e,f (especially in Figure 2.4a,f), but not in Figure 2.4c,d. The absence of large extreme values at high latitudes in Figure 2.4c,d indicate that the R014 and R05 models have lower χ^2 values than the other models in high latitudes in Figure 2.3. Some of the latitudinal A_{diff} value differences could be a result of the change of measurable Θ as shown in Figure 2.2a. Another issue that might influence the results is incomplete filtering of sun glint regions. Note that Figure 2.4a has significantly negative A_{diff} values in most latitudes at Θ~150° where the phase function of the R0001 model has an obvious peak in Figure 2.1. In general, the consistency of A_{diff} results for the R05 and R014 models is better than for the other models in high latitudes, and similar in the tropics.

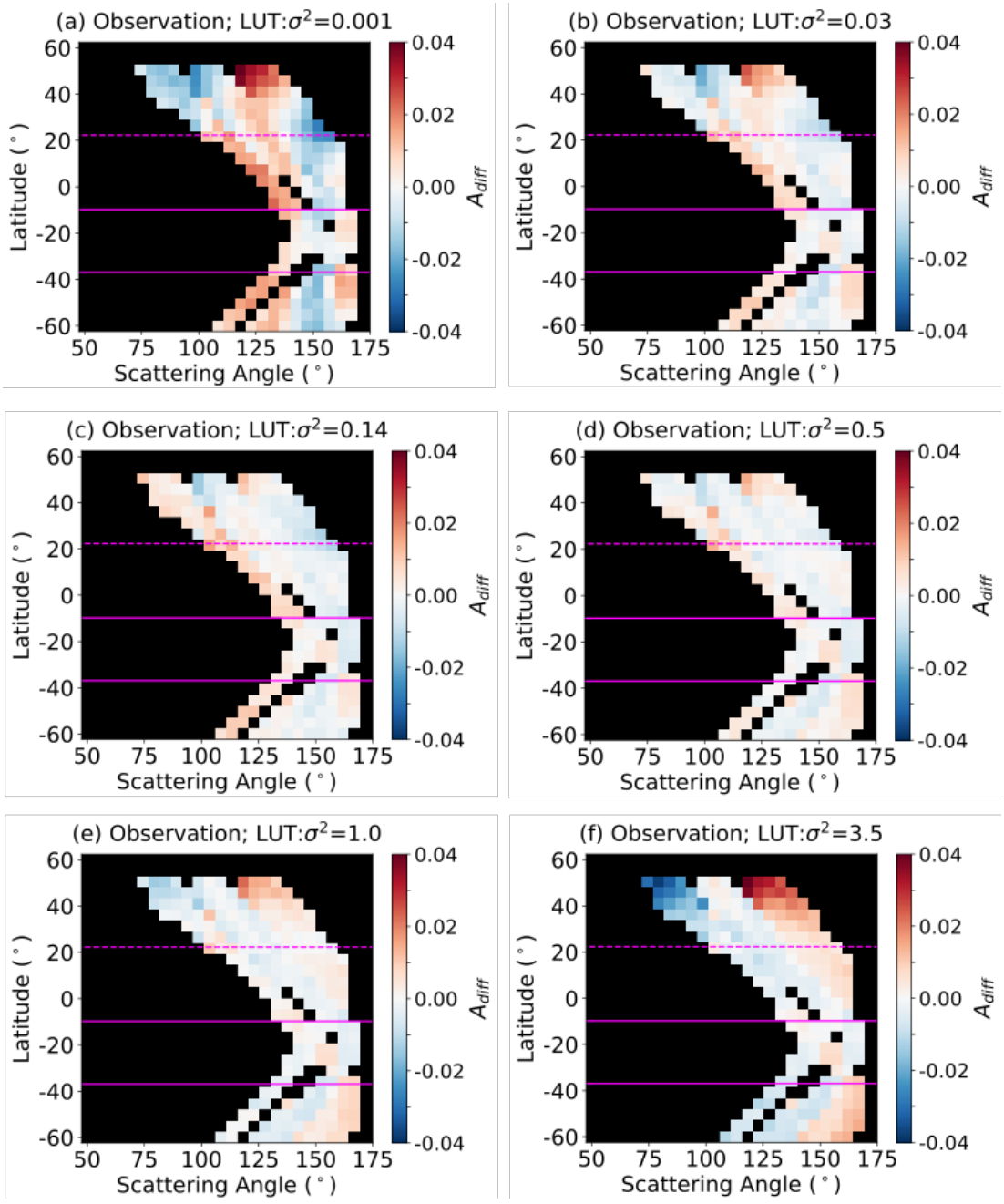

Figure 2.4 The median value of all spherical albedo differences (A_{diff}) in latitude-scattering angle bins on December solstices from 2012 to 2015 using (a) R0001, (b) R003, (c) R014, (d) R05, (e) R10, and (f) R35 ice particle models. The dashed and solid lines correspond to solar zenith angle (SZA) 50° and 30°, respectively.

2.3.2.2. Sensitivity Test with Synthetic Dataset

To investigate which ice particle model produced A_{diff} values at high SZAs such as the case shown in Figure 2.4, a sensitivity study is performed with simulated data (Figure 2.5). The simulated radiances are generated using the same December solstice observations and the same pixel filtering process as in Section 2.2.1, the viewing geometry from each MISR camera observation, and the τ from MODIS with the R05, R10, and R35 models. In other words, the simulated radiances are constructed using the same satellite geometry as the MISR data but the reflectances are generated with the R05, R10, and R35 model LUTs using the τ from the collocated MODIS MC6 product. Subsequently, A_{diff} values are computed using the LUTs from the other two ice particle models.

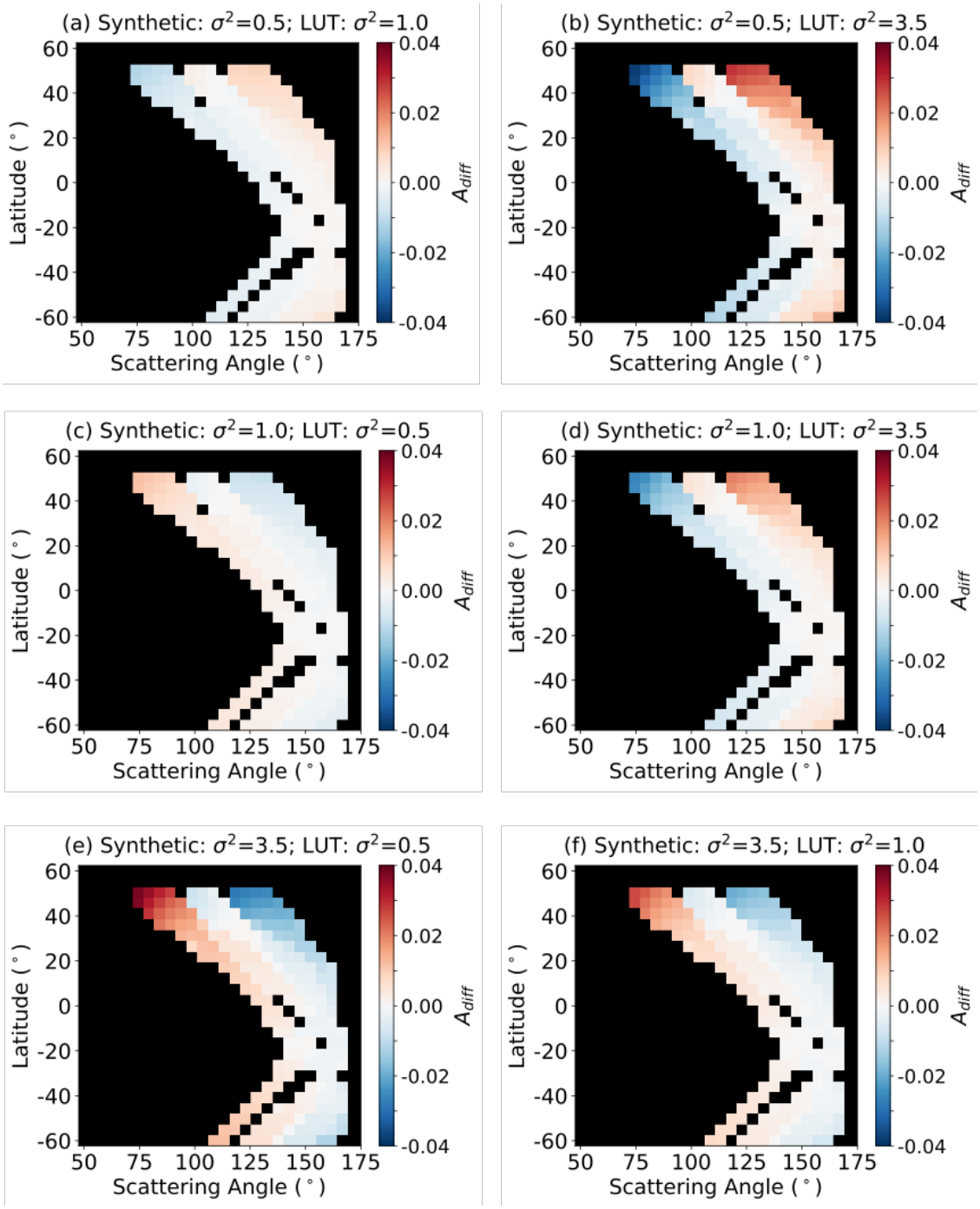

Figure 2.5 The variations of median A_{diff} values with latitude and scattering angle computed from a synthetic dataset generated with the R05 model (a, b), the R10 model (c, d), and the R35 model (e, f), and then retrieved using the LUTs with the other two models.

Compared to the simulated dataset produced by the R10 model (Figure 2.5c,d) and the R35 model (Figure 2.5e,f), A_{diff} values computed from the simulated dataset produced by the R05 model (Figure 2.5a,b) have better consistency with A_{diff} values computed with real data (Figure 2.4) at high SZAs. Specifically, Figures 2.5a and 2.4e illustrate A_{diff} values based on the same R10 LUTs. The simulated A_{diff} pattern in Figure 2.5a reproduces the negative–positive patterns of A_{diff} values (i.e., positive values of A_{diff} become negative with increasing Θ in a latitude) at high latitudes in Figure 2.4e. Similar negative–positive patterns in high latitudes are seen in both Figures 2.4f and 2.5b, which use the same R35 LUTs. However, neither Figure 2.5d nor Figure 2.5f are similar to Figure 2.4f even using the same R35 LUTs. The similarity of using the same LUTs between Figures 2.4 and 2.5 indicate that the R05 model is closer to the actual ice particle in the measurable range of scattering angles at high latitudes. With use of the same approach to compare Figures 2.4 and 2.5 under SZA < 30°, it is found that both the R05 and R10 models do not match the actual ice cloud particle as well as the R35 model when SZA < 30°, but the difference with the R35 results are rather small. To summarize, the similarity between Figures 2.4 and 2.5 implies that the R05 model fits observations better than the R10 and R35 models for SZA > 30°. However, it is not straightforward to select the most optimal model when SZA < 30°.

2.3.2.3. Classification by Heterogeneity of Clouds

To better understand the effect of cloud heterogeneity on variations of A_{diff} values in latitude, we further classify the A_{diff} values by H_σ and τ. Figure 2.6 shows A_{diff} computed with the R05 model in a 4×4 matrix with four τ bins: 0–3, 3–8, 8–16, and 16–

64, and four H_σ bins: <0.4, 0.4–1.6, 1.6–3.2, and 3.2–15. A previous study (Zhang et al., 2012) selected 0.3 as the threshold for a homogenous cloud, but very few selected pixels in this study meet this threshold. Therefore, a higher threshold (i.e., H_σ = 0.4) was used here to select homogeneous clouds (i.e., the first row in Figure 2.6). The same pixel filtering process as in Section 2.2.1 was applied here.

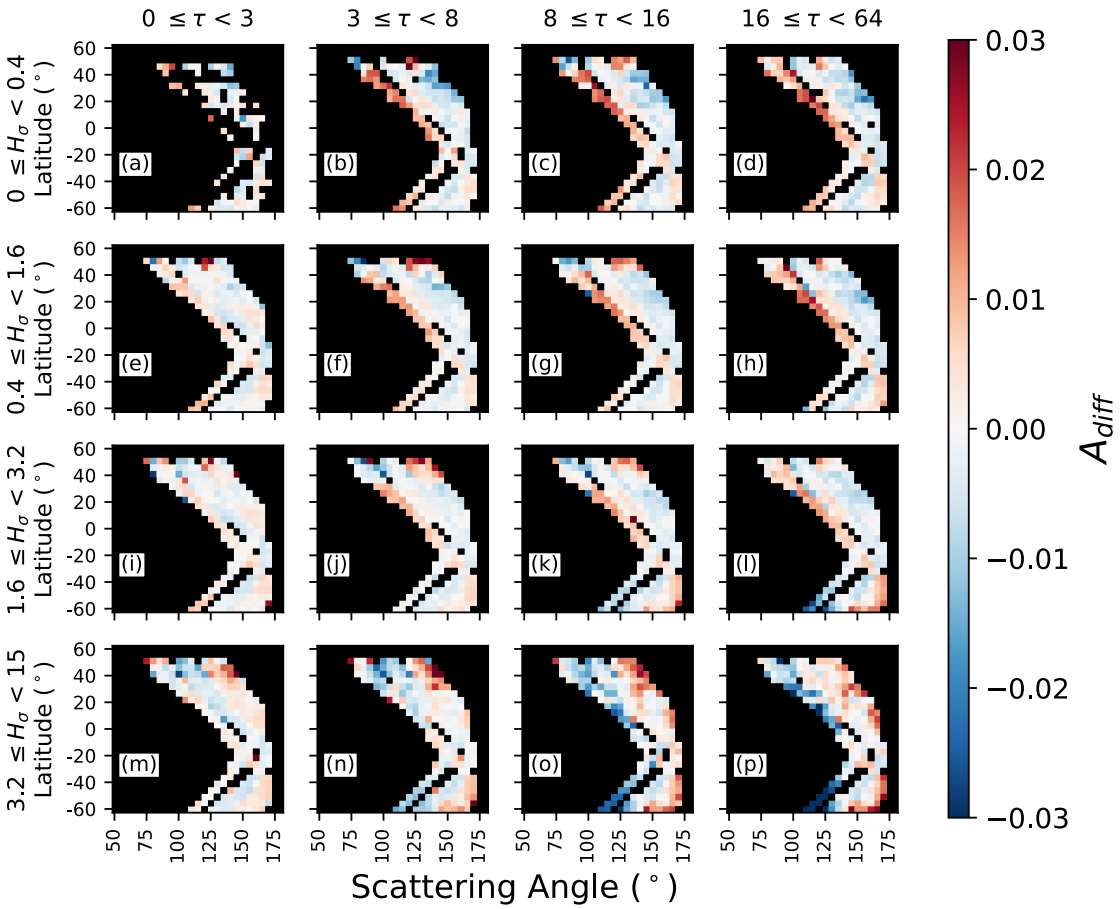

Figure 2.6 The median A_{diff} values for ranges of cloud optical thickness as a function of cloud heterogeneity index (H_{σ}) on December solstices from 2012 to 2015 stratified by (from left to right) cloud optical thickness bins of 0–3, 3–8, 8–16, and 16–64; and (from top to bottom) H_{σ} bins of 0–0.4, 0.4–1.6, 1.6–3.2, and 3.2–15.

The A_{diff} values become more negative or more positive with increasing τ in Figure 2.6. The larger absolute value of A_{diff} for larger τ show the R05 results are more consistent with measurements for optically thin clouds than in optically thick clouds. Unlike the impact of increasing τ, the sign of A_{diff} changes with increasing H_σ. In a broad sense, A_{diff} decreases with increasing Θ in low H_σ bins but increases with increasing Θ in high H_σ bins. Compared with all H_σ bins, $1.6 < H_\sigma < 3.2$ bins have a trend of A_{diff} with increasing Θ that is similar to the trend in Figure 2.4a. When H_σ increases, the decreasing trend of A_{diff} values with increasing Θ reverses to an increasing trend, indicating that the scattering angular distribution of reflectance depends on cloud homogeneity.

2.3.2.4. Latitudinal Variations of Consistency to in Measurements for of Thick Homogeneous Clouds

Since low H_σ clouds are less likely to be influenced by 3D effects, the results are recomputed for thick homogeneous clouds ($H_\sigma < 0.4$ and $\tau > 16$). Figures 2.7 and 2.8 are the same as Figures 2.3 and 2.4, but only for thick homogeneous clouds. Compared to the results for global clouds (Figure 2.3), the results for thick homogeneous clouds show that: (1) the χ^2 of all selected models are significantly lower in thick homogeneous clouds; (2) the absolute differences of χ^2 among models are much larger in both the tropics and extra-tropics; and (3) the χ^2 of each model in the Northern Hemisphere is not significantly larger than χ^2 in the Southern Hemisphere. While the R05 model generally has the lowest χ^2 in all latitudes in Figure 2.3, the χ^2_{R10} and χ^2_{R35} results are smaller than the χ^2_{R05} counterparts at latitudes between 20° S and 30° N in Figure 2.7. In latitudes between 20° S–60° S and between 30° N–60° N, the R05 model and the less roughened ice models produce better

fits among the six. In other words, the optimal model suggests the need for rougher ice particles in the tropics than in the extra-tropics. Furthermore, Figure 2.7 does not show a simple relationship between χ^2 and g. For instance, at latitudes between 20° S and 30° N, χ^2 of the R14 model, which has the lowest g, is within the range of the other models, and χ^2 of the R0001 and R35 models are not similar even though these two models have similar g values.

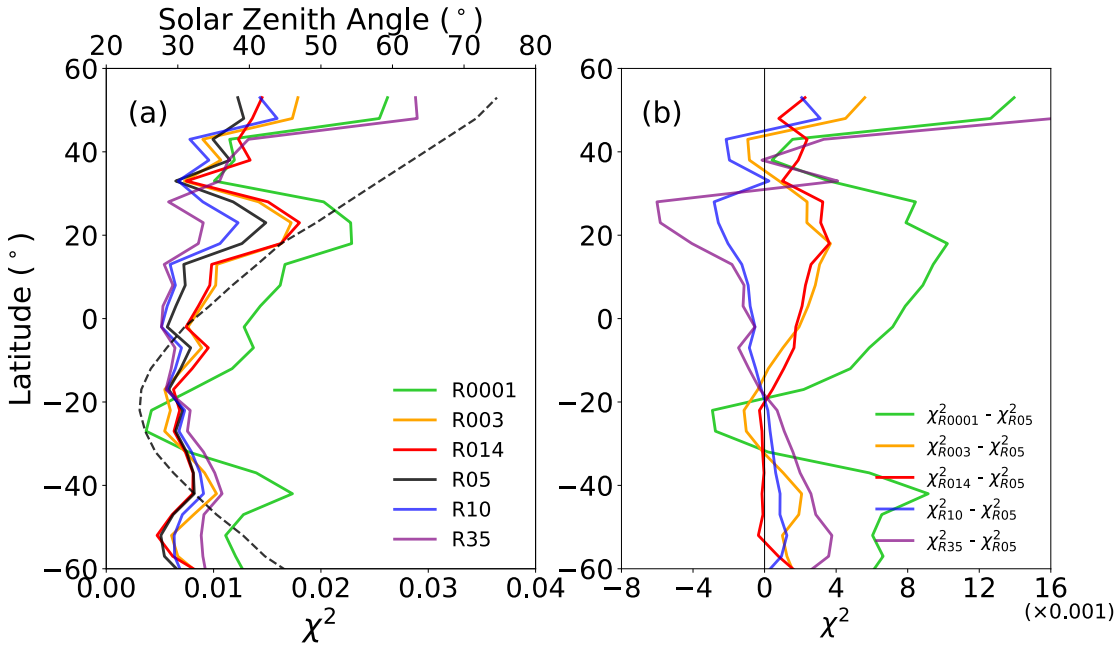

Figure 2.7 The same as Figure 2.3 but computed for thick homogeneous clouds only. (a) The χ^2 using the R0001, R003, R014, R05, R10, and R35 ice particle models on December solstices from 2012 to 2015. The dotted curve (and top scale) is the median SZA as a function of latitude. (b) The χ^2 value using each corresponding model minus the χ^2 value using the R05 ice particle model as a function of latitude.

Figure 2.8 is the same as Figure 2.4 but computed for thick homogeneous clouds ($H_\sigma < 0.4$ and $\tau > 16$). For SZA < 30°, the A_{diff} values computed with all six models display nearly the same pattern as shown in Figure 2.4, and values are close to zero at most measurable scattering angles. Every model in Figure 2.8 shows positive A_{diff} values for the lowest measurable Θ in each latitude when 30° < SZA < 50°, particularly with less roughened models. At high latitudes (SZA > 50°), the A_{diff} values show a relationship with g. Specifically, the A_{diff} values at the smallest measurable Θ turn negative with a higher g model and at the largest measurable Θ turn positive.

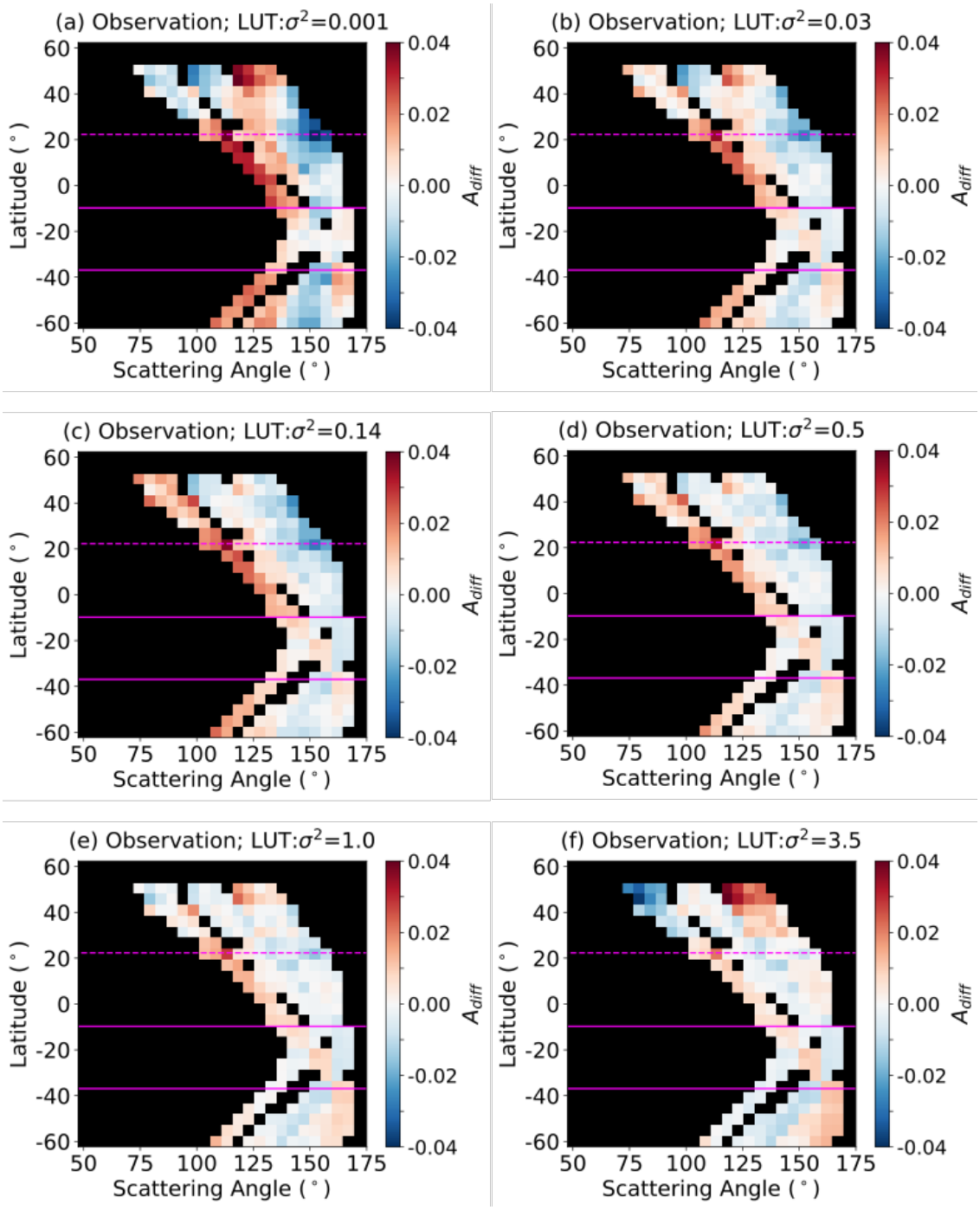

Figure 2.8 The same as Figure 2.4 but computed for thick homogeneous clouds only. The A_{diff} value in latitude-scattering angle bins on December solstices from 2012 to 2015 using (a) R0001, (b) R003, (c) R014, (d) R05, (e) R10, and (f) R35 ice particle models. The dashed and solid lines correspond to SZA 50° and 30°, respectively.

2.4. Discussion

To examine the latitudinal variations of six ice particle models with a range of surface roughness, we compute spherical albedo difference (A_{diff}) values using different LUTs for each model. We then compute the χ^2 (the residual sum of squares of mean A_{diff}) in latitude. The A_{diff} is defined as the difference between the cloud spherical albedo ($\widetilde{A_{\mathrm{s}}}$) of a selected MISR camera and the mean of $\widetilde{A_{\mathrm{s}}}$ averaged across all available cameras for a given pixel. The χ^2 values in the extra-tropics are significantly larger than the counterparts in the tropics. Hexagonal column ice particles occur more frequently at low latitudes than high latitudes (Chepfer et al., 2001), and this may be a possible reason that the aggregated hexagonal column habit better explains the ice particle in the tropics than in the extra-tropics. The differences of χ^2 values among ice models in the global data are not significant in the tropics, and MISR data are unable to discriminate between the models. However, in the thick homogeneous cloud regime, the differences of χ^2 values among models were significantly heightened in both the tropics and extra-tropics. The optimal particles are more roughened in the tropics than in the extra-tropics in thick homogeneous clouds, which is in agreement with previous results (Cole et al., 2014). The high frequency of strong convection in the tropics likely has an influence on the MISR observations, leading to an indication of heightened surface roughening.

In addition to the χ^2 variation with latitude, the variation of A_{diff} as a function of increasing scattering angle Θ also varies with latitude but more precisely changes with SZA when using any of the LUTs. These differences of A_{diff} also appear in the clouds stratified by cloud homogeneity index H_σ and optical thickness τ. If a given camera-

retrieved τ is higher than the counterparts associated with the other cameras, a higher A_s value would be computed for this one camera than for the other cameras, and this higher A_s value leads to a positive A_{diff} value. Therefore, the magnitudes of A_{diff} values at different Θ imply differences between the retrieved τ and the mean τ of all cameras in each Θ. A positive (negative) A_{diff} value broadly means that the retrieved τ is larger (smaller) than mean τ of all cameras. Furthermore, the inference of τ is determined primarily by phase function, and the impact of ice particle phase function on reflectance is important (C-Labonnote et al, 2001; Zhang et al., 2009), particularly for optically thin clouds. Thus, the sign of the A_{diff} value is related to the variation of the phase function with a scattering angle. Note that the A_{diff} method is not sensitive to the absolute value of the phase function, but only to the relative variation of the phase function with scattering angle. This approach, also described in C.-Labonnote et al. (2001), is able to explain why the A_{diff} value at Θ~150° in Figure 2.4a is negative at almost every latitude, but this difference does not appear in other panels in Figure 2.4 because the phase function of the R0001 model has a significant peak at Θ~150°. Similarly, this is the reason that the R05 model fits the measurements better than the other models at most latitudes. The phase function of the R05 model fits the measurements better than the other selected models over the MISR available Θ range.

High latitudes tend to have a high SZA, and the 3D radiative effect is one potential explanation for how the A_{diff} appears to change with SZA. Previous studies (Liang and Di Girolamo 2013; Loeb and Davies 1997; Varnai and Marshak 2007) investigate the impact of solar geometry on the 3D effect, particularly variations of the retrieved τ with SZA.

Since τ can easily be converted to A_s, there may be a similar potential impact of the 3D effect on the results. In general, low H_σ clouds have uniform cloud tops, which approximately satisfy the plane-parallel approximation. Thus, the impact of the 3D effect on reflectance of this type of cloud is not as strong as on a high H_σ cloud. Therefore, low H_σ clouds are usually less susceptible to the 3D effect than high H_σ clouds. The stratified clouds in Figure 2.6 have better agreement with this theory. The trend of A_{diff} values with increasing Θ as a function of SZA is significantly larger for high H_σ clouds than for low H_σ clouds. Note that we consider only one definition of cloud heterogeneity, and a different definition may lead to different results (Grosvenor and Wood 2014).

The microphysical ice particle habit distribution changes with latitude, dynamical environment, and temperature (McFarquhar and Heymsfield 1996; Bailey and Hallett 2004; Baran 2009) could impact the trend of A_{diff} values with increasing Θ at different latitudes as well. In the thick homogeneous cloud regime (Figure 2.8), not all models show different trends of A_{diff} values with Θ in different latitudes compared to global clouds (Figure 2.4). In addition, high latitudes frequently have ice clouds with a lower cloud top height (Sassen et al., 2008). If we remove clouds with cloud-top temperatures >233K in the data filtering process, some ice clouds at high latitudes are probably removed because the tropopause is lower there. It is interesting to note that for the thick homogeneous cloud regime, the larger differences of χ^2 values between the models enable some discrimination between values of surface roughness. The best-fit particles are more roughened in the tropics than extra-tropics in thick homogeneous clouds.

The limited and variable range of available Θ measurements might be one source of uncertainty for computing the A_{diff} value. Only limited Θ ranges can be sampled by the MISR sensor, but the whole Θ range must be used in retrievals to compute reflectance. It means that there is insufficient data to know how the phase function in the undetectable Θ range changes in each latitude, and to evaluate how large the influence of the phase function in the undetectable Θ are to our results. The range of available Θ values from MISR varies systematically with SZA (Figure 2.2). McFarlane and Marchand (2008) also suggested that the retrieved ice particle habit depends on the minimum observed Θ. Not only the Θ range but also the pixel frequencies in each Θ-latitude bin changes with latitude. Because of varying sun-earth-satellite viewing geometry, it is not straightforward to evaluate these factors on the computed A_{diff} value.

The consistency of six ice models (R0001, R003, R014, R05, R10, and R35 model) is compared to MISR measurements at different latitudes. Our results, based on the fused MODIS-MISR dataset, can be used to estimate the latitudinal (or SZA) bias in retrievals of MC6 operational products because the MC6 operational ice cloud property retrievals assume that the same R05 model applies globally. Our analysis shows that the R05 model works very consistently with global MISR measurements but there may need to be more roughened particles in the tropics.

In the bi-spectral shortwave technique (Nakajima and King 1990), a large asymmetry factor ice particle model causes a higher retrieved τ and lower reff (King 1987). The asymmetry factors of the R05 and R014 models are the lowest of the six models, and the R35 model has the largest asymmetry factor. As noted earlier, the extreme

randomly distorted particle surface facets of the R35 model may increase the amount of forward scattering as an artifact of the numerical modeling. Since the best-fit model is hard to define in the tropics because of the rather small differences in χ^2 values, the ice cloud τ and effective radius could have large uncertainties by assuming the best-fit model from MISR measurements in the retrieval.

2.5. Summary and Conclusion

This study examines the latitudinal dependence of ice particle models, based on the MISR-MODIS fused dataset on December solstices from 2012 to 2015. To evaluate the latitudinal consistency of ice particle models with MISR measurements, we apply the SAD method to the fused dataset by using the ice particle habit of the MODIS Collection 6 (MC6) ice model (R05 model) with six different assumptions of ice particle surface roughness: σ2 = 0.001, 0.03, 0.14, 0.5, 1.0, and 3.5 (referred to as R0001, R003, R014, R05, R10, and R35 models, respectively).

Of the six models used in this study, the R05 model is one of the most consistent in comparison with the MISR measurements globally but has a similar consistency with other models at lower latitudes. The results of computing the residual sum of squares of mean A_{diff} (χ^2) show that all six χ^2 are much higher at >30°N than all other latitudes. For thick homogeneous clouds, the consistency among models is significantly greater in both the tropics and extra-tropics, and the larger differences of χ^2 values between the models enable some discrimination between values of surface roughness. The optimal particle model should have rougher ice particles in the tropics than in the extra-tropics. Specifically, the MC6 model and less roughened models fit thick homogeneous clouds

better than more roughened models in the zonal means for latitudes between 20°S–60°S and 30°N–60°N; for latitudes between 20°S and 30°N, more roughened models produce better fits among the six.

Comparisons of computed A_{diff} values in latitude bands show that the trend of A_{diff} values with increasing Θ for each ice model changes with latitude, or more precisely, these variations are primarily a function of SZA. This result demonstrates the latitudinal variation of the best-fit model because of the relationship between SZA and latitude (e.g., the SZA in high latitudes is large). The variation of A_{diff} values with Θ also appears to change with SZA. However, homogenous clouds (low H_σ values) do not show the change of A_{diff} trend with SZA. In addition, for the classified results, the sign of A_{diff} changes with increasing H_σ, but not with increasing τ, as only the magnitudes of the A_{diff} values increase with increasing τ.

Because MISR provides reflectances over a wider Θ range than MODIS, the collocated MODIS and MISR data/products provide an unprecedented opportunity to identify the optimal ice particle model for retrievals. The variations of the χ^2 value with latitude found in this study suggest that the invariant ice particle shape assumption for retrieving ice particle properties needs to be reconsidered.

3. ICE CLOUD OPTICAL THICKNESS, EFFECTIVE RADIUS, AND ICE WATER PATH INFERRED FROM FUSED MISR AND MODIS MEASUREMENTS BASED ON A PIXEL-LEVEL OPTIMAL ICE PARTICLE ROUGHNESS MODEL[*]

The Multi-angle Imaging SpectroRadiometer (MISR) provides measurements over a wider scattering-angle range for a given location than a cross-track scanning sensor such as the MODerate resolution Imaging Spectroradiometer (MODIS). Based on a full year (2013) of fused MISR-MODIS datasets, we develop a variable surface roughness model for ice particles with the goal of identifying the optimal degree of roughness in the ice model for a given pixel containing single-layer ice clouds. For the MISR-MODIS observations over oceans, severe roughness values are often selected for a pixel when optical thickness (τ) and particle effective radius (Reff) are large in conjunction with larger cloud heterogeneity index ($H\sigma$) or a warmer cloud top temperature.

Furthermore, τ, R_{eff}, and ice water path (IWP) are retrieved with the optimal model and compared to operational MODIS Collection 6 (MC6) products that assume a constant roughness. In general, the retrievals based on the present optimal model lead to greater consistency with MISR measurements, and results in larger median τ by 10.1% and smaller median R_{eff} by 6.5% but almost identical IWP in comparison with the MC6 counterparts. The higher average τ value is caused by a slightly larger number of large τ

[*] Edited and reprinted with permission from "Ice cloud optical thickness, effective radius, and ice water path inferred from fused MISR and MODIS measurements based on a pixel-level optimal ice particle roughness model" by Yi Wang, Ping Yang, Souichiro Hioki, Michael D. King, Bryan A. Baum, Larry Di Girolamo, and Dongwei Fu, 2019. Journal of Geophysical Research: Atmospheres 124, no. 22 (2019): 12126-12140. Copyright [2019] American Geophysical Union.

cases, but the smaller average R_{eff} value is due to the shifting of the retrieved R_{eff} value toward smaller values by approximately 2-4 μm in comparison to the MC6 distribution over all seasons. Both τ retrievals have similar regional and monthly variations, but a larger annual cycle of R_{eff} is associated with the optimal model.

3.1. Introduction

Accurate estimation of ice cloud optical thickness (τ) and cloud particle effective radius (R_{eff}) is fundamental for parameterizing and constraining cloud radiative effects in global climate models (GCMs) (Liou and Yang, 2016; Platnick and Oreopoulos, 2008; Baran, 2009; Loeb et al, 2018) and for understanding the Earth's radiation budget (Liou, 1986; Stephens et al., 1990; Chen et al., 2000; Yang et al., 2015). In particular, the product of optical thickness and the effective particle size is proportional to the ice water path (IWP) (Hansen and Travis, 1974; Yang et al. 2018). To infer these parameters from satellite sensor data, an ice particle model is necessary for the forward light scattering calculations involved in generating the look-up tables (LUTs) in implementing a retrieval algorithm. Recent studies indicate that the adoption of a forward ice cloud optical property model has a significant impact on cloud property retrievals (Mishchenko et al., 1996; Baum et al., 2005; Baran, 2009; Zhang et al. 2009; Platnick et al. 2017; Loeb et al., 2018; Yang et al., 2018).

Because of the sensitivity of satellite retrievals to an assumed ice cloud particle habit model in the forward light scattering computations, defining an optimal ice particle model for global operational retrievals could have a significant impact on the use of the products in various problems in atmospheric research. At present, most satellite-based

retrievals assume ice particle habits without considering spatial and temporal variations (Baum et al., 2005; Letu et al., 2016; Platnick et al., 2017; Loeb et al., 2018). However, both field campaign experiments and laboratory measurements have confirmed that the ice particle habits and sizes vary with supersaturation, temperature, and the ambient dynamics, implying that an optimal ice particle habit model may have geospatial dependence (Heymsfield et al., 2010, 2013; Bailey and Hallett 2004, 2009). Thus, it is important to understand the geospatial distribution of an optimal ice habit model for its application to satellite-based cloud property retrievals, and to the assessment of the potential biases caused by the invariant ice habit model assumption.

A recent study examined the agreement between Multi-angle Imaging SpectroRadiometer (MISR) sensor measurements and radiative transfer simulations based on an ice habit model in conjunction with a varying degree of surface roughness. The surface roughness was found to be an important parameter in inferring ice cloud properties due to a latitudinal dependence that varied seasonally with the thermal equator annual cycle (Wang et al., 2018). The MISR cameras view a wide range of scattering angles for a given pixel containing an ice cloud and provide valuable data for determining a variable ice habit model that specifies an optimal value of the degree of ice particle surface roughness in fitting measurements at the pixel level.

This study addresses two questions that are important for global retrievals of ice cloud properties from satellite data: 1. what are the optimal values of ice particle surface roughness in different cloud regimes for MISR measurements, and 2. what are the resulting differences in the cloud properties inferred with the optimal roughness values

compared to those obtained based using a constant degree of surface roughness? To address these questions, we test a varying ice particle surface roughness model using a fused MISR and Moderate Resolution Imaging Spectroradiometer (MISR-MODIS) dataset for 2013. Furthermore, we compare present τ, R_{eff} and ice water path (IWP) retrievals against the MODIS Collection 6 (MC6) counterparts in multiple cloud regimes towards a better understanding of the seasonal variations of the differences between the two retrievals.

3.2. Data and Methods

In this study, one full year (2013) of MISR and MODIS data is fused based on cloud-top properties detailed in Liang et al. (2009) and Liang and Di Girolamo (2013), with updates in Wang et al. (2018). There was no strong signal from El Nino nor La Nina in 2013, based on the ENSO index. The MISR and MODIS datasets are fused by registering the MODIS radiances and MOD06 cloud products reported at 1km resolution onto the MISR 1.1km Space-Oblique Mercator (SOM) grid. Both satellite sensors are onboard NASA's Terra satellite platform that is sun-synchronous with a daytime equator-crossing at 10:30am local time. As originally discussed in Liang et al. (2009), the fusion process begins by registering small groups of MISR pixels (3 × 3 pixels identified as cloudy) using the feature matcher M2 (Muller et al., 2002) to track clouds across MISR's 9 cameras, and pairing radiance viewed by each of non-nadir cameras with the radiance viewed by the nadir camera for the chosen cloud element. MODIS radiances and cloud retrievals are registered to the MISR nadir-camera grid. In all, the MISR-MODIS co-registered dataset includes collocated MISR camera bidirectional reflectance factors

(BRF) at 0.86 μm, MODIS band 2 and 7 reflectances (0.86 and 2.13 μm, respectively), MOD06 cloud products (which includes τ, R_{eff}, cloud heterogeneity index (Hσ), cloud top height, cloud thermodynamic phase, cloud top pressure, and cloud top temperature), MISR sun-view geometry, and the MISR stereo-cloud top height retrievals. All these parameters are at 1.1km spatial resolution in the fused dataset.

Index Hσ from MC6 dataset is defined as the standard deviation of the 16 subpixel reflectances with 250 m resolution in the 1-km pixels divided by reflectance (Liang et al., 2009; Platnick et al., 2015, 2018). The occurrence of large subpixel standard deviations in cloud optical thickness result in high Hσ values, and this index is widely used to study three dimensional (3D) cloud effects (Di Girolamo et al., 2010; Zhang and Platnick, 2011; Liang and Di Girolamo, 2013).

The reflectances from fused MISR 0.86 and MODIS dataset are filtered using a set of criteria summarized as follows. The MISR sensor provides reflectances for a cloud target at up to 9 different scattering angles (Diner et al., 1998; Diner et al., 2002). To minimize the potential influence of 3D radiative effects on the viewing angle dependence of the retrievals (Liang and Di Girolamo 2013), only the three close-to-nadir viewing MISR cameras (AA: near-aft camera, AN: nadir camera, and AF: near forward camera) are used in this study. If the glint angle from any camera is < 35°, the reflectance is assumed to be impacted by sunglint. Only pixels with at least 2 views that are unaffected by sunglint are selected for further analysis. Furthermore, the analysis is limited to overcast MODIS pixels over ocean within the MISR swath, for which cloud thermodynamic phase is determined to be ice based on the MC6 infrared (IR) cloud phase

flag (Platnick et al., 2018). The pixel locations are restricted to 60°N-60°S to avoid the effects of snow and sea ice on the measured reflectance. Compared to Wang et al. (2018), we add an additional quality-control step to remove potential multilayer clouds (McFarlane and Marchand, 2008; Naud et al., 2002). Specifically, we identify the potential presence of multilayer clouds as occurring when the MISR stereo height values and MODIS cloud top height values differ by more than 2000 m (Mueller et al., 2017).

For the fused MISR-MODIS dataset that has been filtered as described above, a variable ice particle surface roughness model is developed as follows. The model adopts the MC6 roughened hexagonal ice aggregate habit in conjunction with 12 values of the degree of ice particle surface roughness (σ^2) for a given pixel. The surface roughness parameter (σ^2) is used to compute the single-scattering properties of ice particles, and is defined as the standard deviation of a two-dimensional Gaussian distribution of the tilting of ice particle surface facets (Yang and Liou, 1998). In particular, $\sigma^2 = 0$ denotes that ice particles have smooth surfaces. A higher value of σ^2 denotes rougher surfaces that generally result in a smoother phase function. Light scattering by smooth ice particles produces strong peaks in the phase functions that correspond to halos that do not appear frequently in reality (Mishchenko et al., 1999). By considering ice particle surface roughness, the halo peaks in the phase function are smoothed. The MC6 model considers a constant roughness value (σ^2=0.5), while this study uses 12 values ranging from $\sigma^2 = 0$ to 3.5. The phase functions corresponding to the selected values of the degree of roughness are shown in Fig. 3.1 and the corresponding asymmetry factor values are listed as well. More detailed descriptions of the ice crystal habits and associated degrees of surface

roughness can be found in the literature (e.g., Mishchenko et al. (1996), Yang and Liou (1998), Yang et al. (2013), Liou and Yang (2016)). Related studies on retrievals of ice cloud parameters by ice crystal models with different shapes and surface roughness can be found in the literature (Platnick et al., 2003; Xie et al., 2012; Hioki et al., 2016; Platnick et al., 2017; Letu et al., 2019).

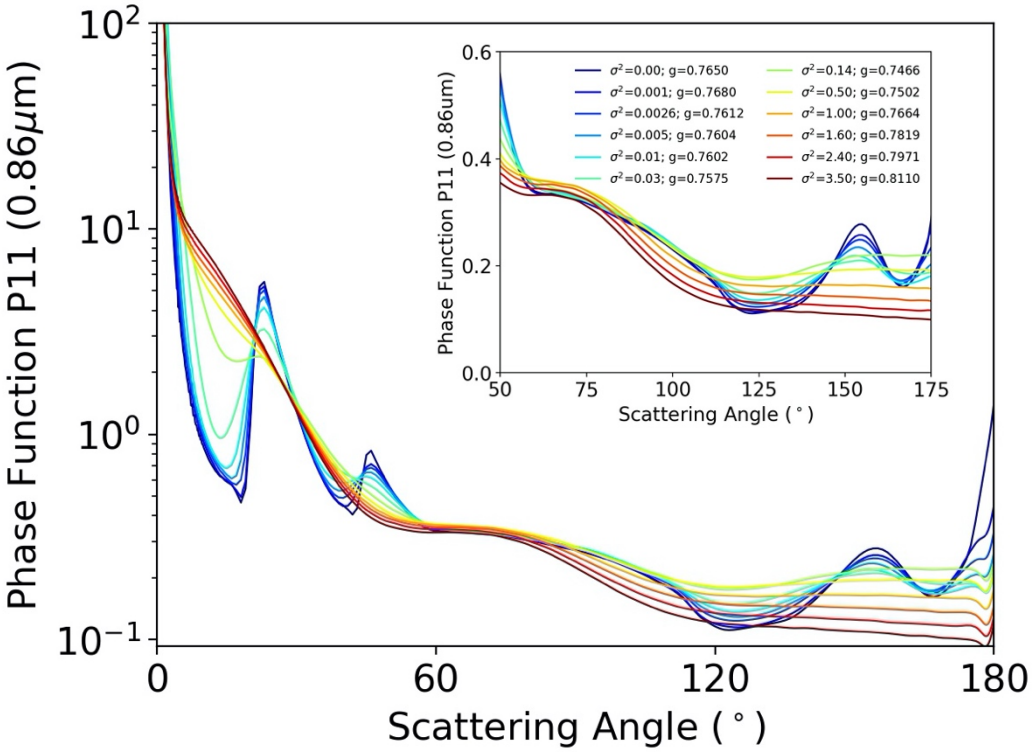

Figure 3.1 The phase functions of the MODIS Collection 6 (MC6) ice cloud model consisting of aggregate columns having an effective radius of 30 μm for 12 different degrees of surface roughness (σ^2) at 0.86 μm. The asymmetry factor (g) of each roughness value is also listed in the inset panel.

The scattering angle range of MISR measurements is primarily at side- and back-scattering angles, due to the solar-satellite camera viewing configuration. Figure 3.2 shows the normalized frequencies at every scattering angle sampled by three MISR cameras (i.e., AA, AN, and AF) for the entire measurements in 2013 between 60°N and 60°S. As seen in Fig. 3.2, the range with scattering angles smaller than 70° is not sampled.

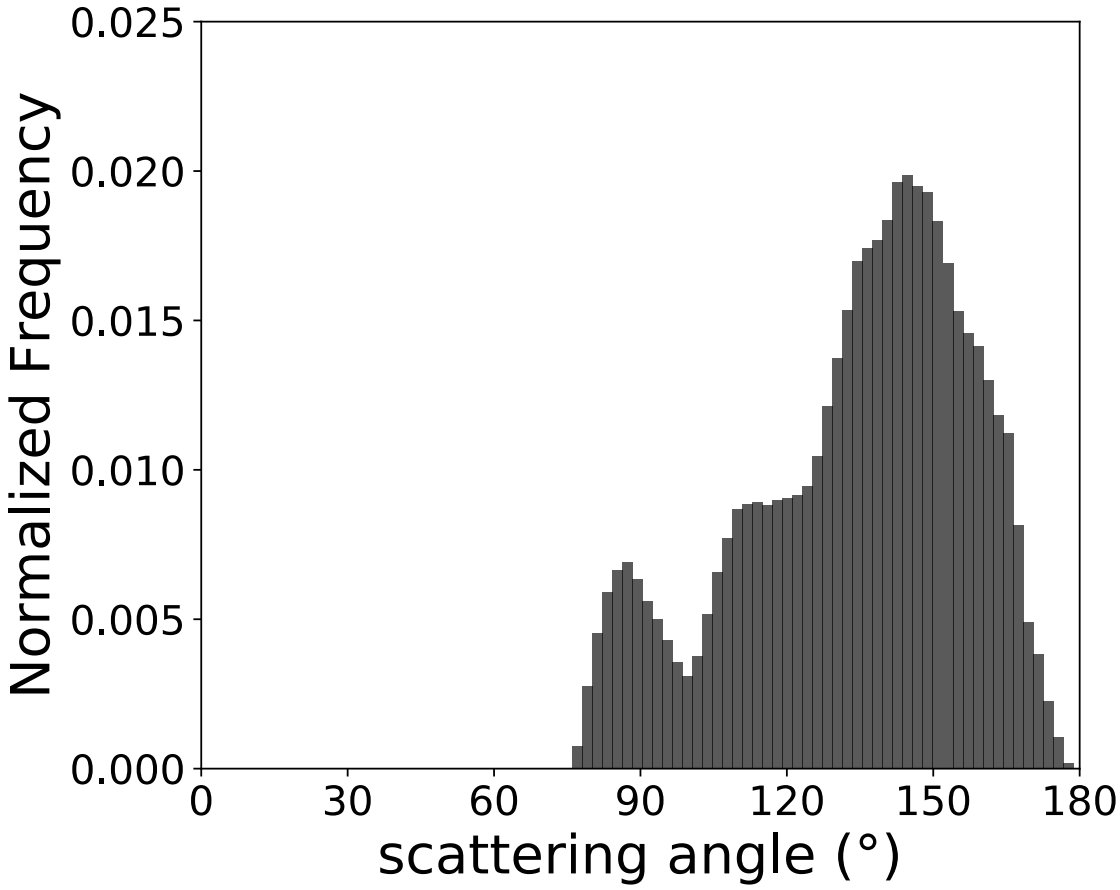

Figure 3.2 The normalized frequency of scattering angle sampled by three MISR cameras (i.e., AA, AN, and AF) for the entire measurements in 2013 between 60°N and 60°S.

The filtered pixel radiances are analyzed using the spherical albedo difference (SAD) method developed by Doutriaux-Boucher et al. (2000), which was applied to a MISR dataset in our previous study (Wang et al., 2018). To use the SAD methodology, an adding-doubling radiative transfer model (Huang et al., 2015) is used to compute the spherical albedos in conjunction with the use of the 12 roughness values. The spherical albedo is a variable that is independent on satellite viewing geometry and is a nonlinear function of τ. τ is not fixed in the computation of spherical albedo; more details are in Wang et al. (2018). The SAD values for a roughness model are computed from the differences of the computed spherical albedo values and the average spherical albedo of all applicable angles (i.e., the scattering angle measured among AA, AN, and AF). If the assumed model perfectly captures the roughness characteristics of the measurements, the SAD values would be zero at all scattering angles.

To identify an optimal ice particle surface roughness value for a pixel, we define χ^2 as the standard deviation of the SAD values for all cameras in conjunction with the 12 roughness values. An optimal value of particle surface roughness is selected in accordance with the smallest χ^2 value. A lower χ^2 value means that the reflectances generated with assumed ice particle model are closer to measurements than those with a higher χ^2 value. Based on the SAD method, the optimal value for the degree of ice particle surface roughness is the value that leads to the best agreement between the simulated radiances and the multi-angle measurements in the fused data set.

In our previous study (Wang et al., 2018), MISR measurements were applied to identify the optimal degree of ice particle roughness. In this study, we further analyze the

differences in the cloud properties (i.e., τ, R_{eff}, and IWP) that are obtained from use of the optimal ice particle model. Based on the identified optimal degree of ice particle roughness, τ and R_{eff} are retrieved using a bi-spectral shortwave technique (Nakajima and King, 1990) implemented with two MODIS bands centered at 0.86 and 2.13 μm. Figure 3.3 shows the schematic data flowchart in this study. Comparisons are made between our computed τ and R_{eff} values with those in the MC6 data products and are shown in Chapter 3.3.2 and 3.3.3.

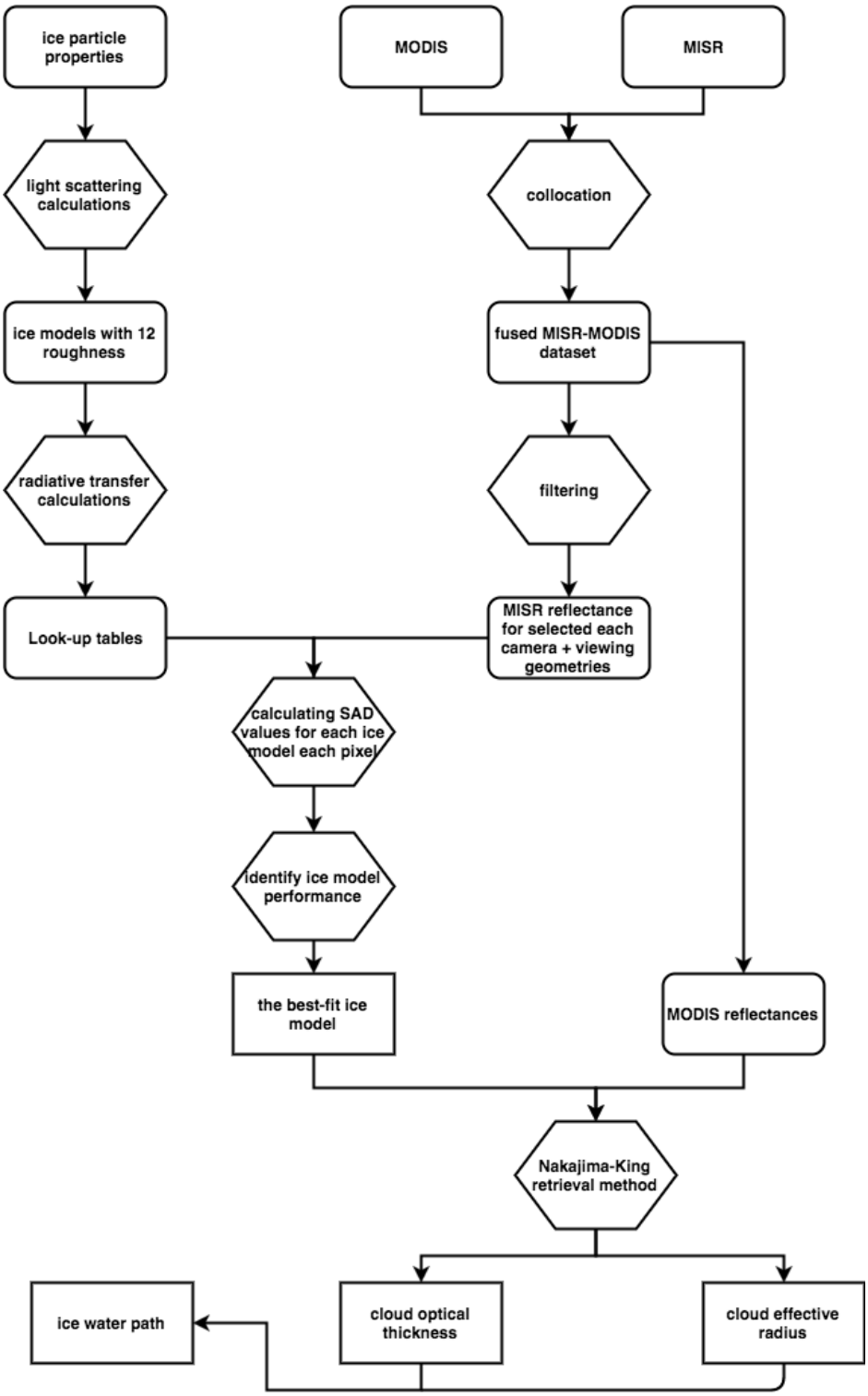

Figure 3.3 The schematic data flowchart in the retrieval system.

To better understand the performance of the present method in this study, Fig. 3.4 shows a sensitivity study of the response of the present retrievals to radiance values containing prescribed random noise. With viewing geometries extracted from MISR normalized radiances and optical thickness values extracted from MODIS Collection 6 products, we generate synthetic radiances at the pixel level for 20 March 2013. The noise is generated by assuming a Gaussian distribution and added to the radiances. The synthetic radiances are generated for each of the 12 surface roughness values and are shown in Fig. 3.4. The ordinate denotes the retrieved degree of roughness. The value for a given bin shows the normalized frequency of the retrieved roughness value based on the synthetic data. The agreement between the retrieved and assumed roughness increases significantly by reducing the noise level from 0.5% (Fig. 3.4a) to 0.1% (Fig. 3.4b).

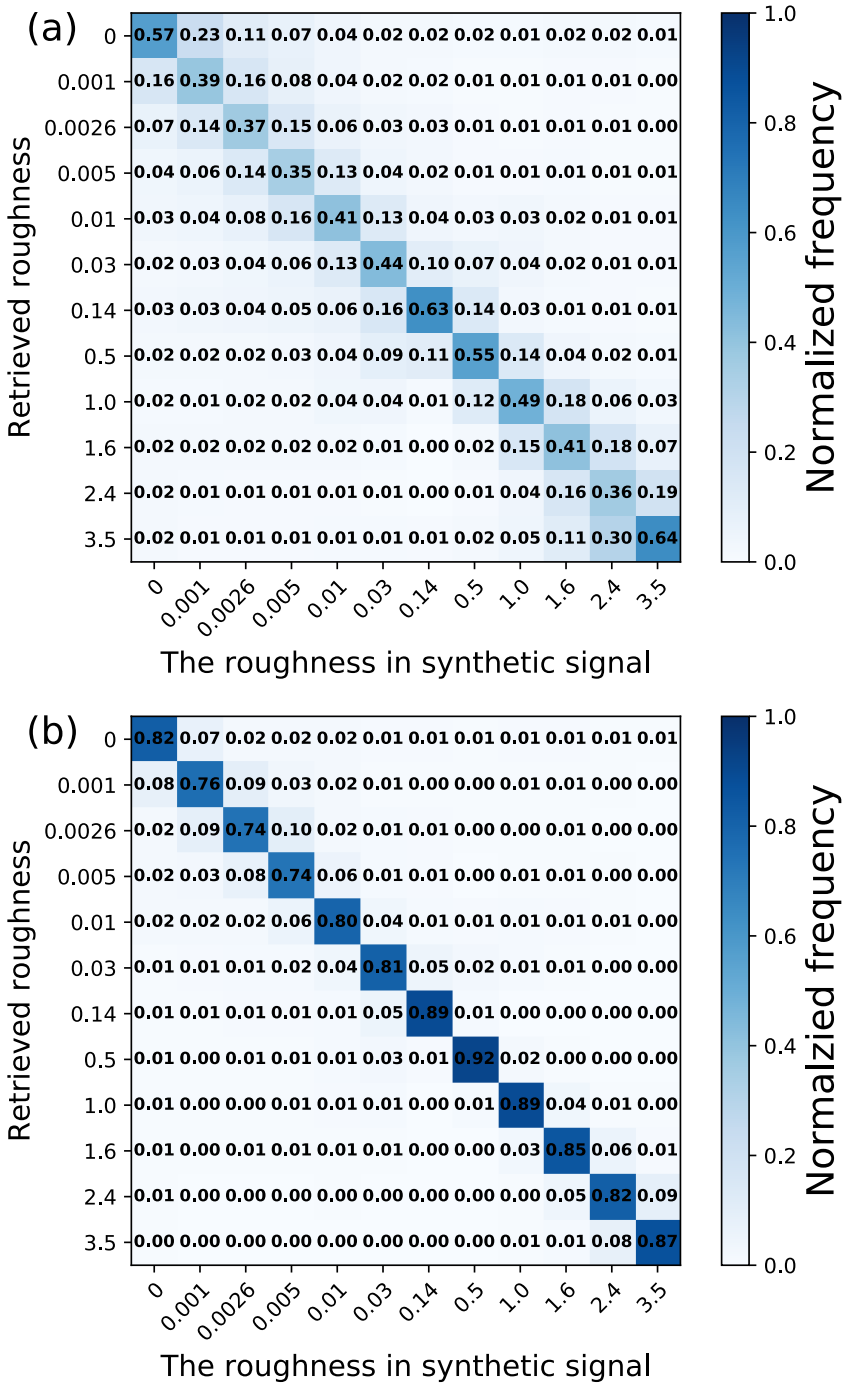

Figure 3.4 The response of the retrieval system based on analysis of synthetic data for each degree of roughness (abscissa) with (a) 0.5% noise, and (b) 0.1% noise, as shown in a distribution of the roughness parameter (ordinate). The values in each bin are the fractions for each degree of roughness; the values in each column sum to 1.

3.3. Results and Discussions

3.3.1. Global statistics of the optimal ice model for different cloud regimes

In this section, the relationships between the optimal ice particle model and several cloud properties (i.e., τ, R_{eff}, $H\sigma$, and the cloud top temperature) are investigated. To show how often different parameters occur, the normalized probability density distributions of these four cloud properties from the 1-year combined MISR and MODIS datasets over the ocean are displayed in Fig. 3.5. The results in Fig. 3.5 are come from MODIS products directly, not using the optimal ice particle model.

We first examine the proportion of an optimal surface roughness value (i.e., a value corresponds to the lowest SAD value from the 12 surface roughness values in Fig. 3.1) for several key cloud parameters inferred from the filtered MISR-MODIS dataset over ocean (Fig. 3.6), including τ (Fig. 3.6a), R_{eff} (Fig. 3.6b), the cloud heterogeneity index ($H\sigma$, Figure 3.6c) and cloud top temperature (Fig. 3.6d). For each of these four parameters, Fig. 3.6 shows the color contours describing the cumulative proportion of the optimal roughness value obtained over a range of the parameter values labeled on the abscissa. The ordinate is the cumulative fraction of an optimal roughness value ranges from $\sigma^2 =0$ (dark blue) to $\sigma^2 =3.5$ (brown) for all analyzed pixels in every bin of the stated variable value along the abscissa. The magenta curve shows the normalized probability of number of pixel in every bin.

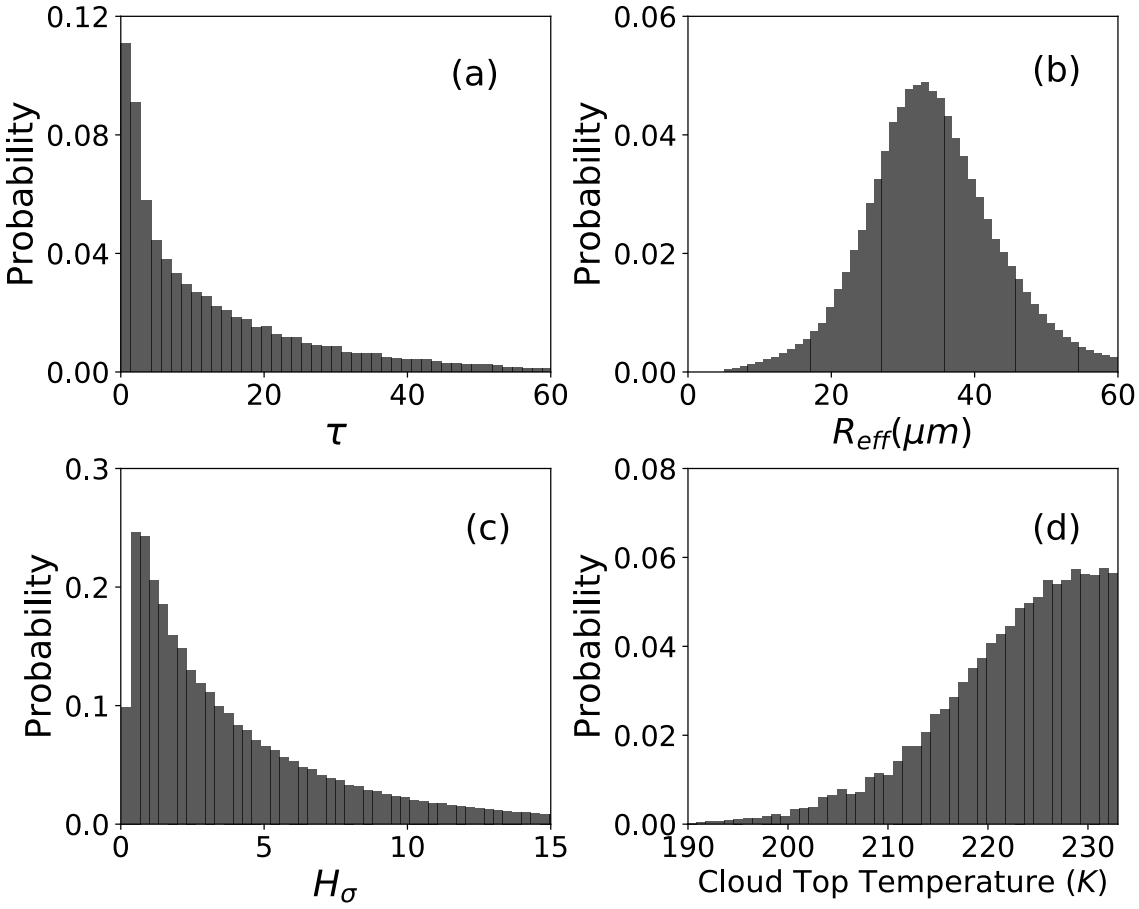

Figure 3.5 The normalized probability density distributions of four ice cloud property variables over the ocean: (a) ice cloud optical thickness (τ), (b) cloud particle effective radius (R_{eff}), (c) cloud heterogeneity index (H_σ), and (d) cloud top temperature.

In Figs. 3.6a and 3.6b, the distribution of the optimal roughness values is shown as a function of τ and R_{eff} values. The σ^2=0.14 case dominates as an optimal roughness value in more than 30% of the pixels over the range of optical thickness and effective radius values. Note that the model with a roughness of σ^2 =0.14 has the lowest asymmetry factor of all the models (see Fig. 3.1). As τ increases, the percentage of severely roughened ice particles ($\sigma^2 > 1.0$) increases, while the percent of essentially smooth ice particles ($\sigma^2 < 0.01$) decreases. Specifically, a rapid increase in the percent of severely roughened particles is noticed for optically thin clouds ($\tau < 3$), while it remains relatively constant when $\tau > 3$. Pristine ice particles tend to form in environment of low updraft velocities, such as in synoptic cirrus. Clouds with a larger optical thickness tend to occur in a more dynamic environment with stronger updraft velocities and water vapor transport. These results demonstrate the difficulty in finding a single ice model that can capture the complexities of ice clouds globally.

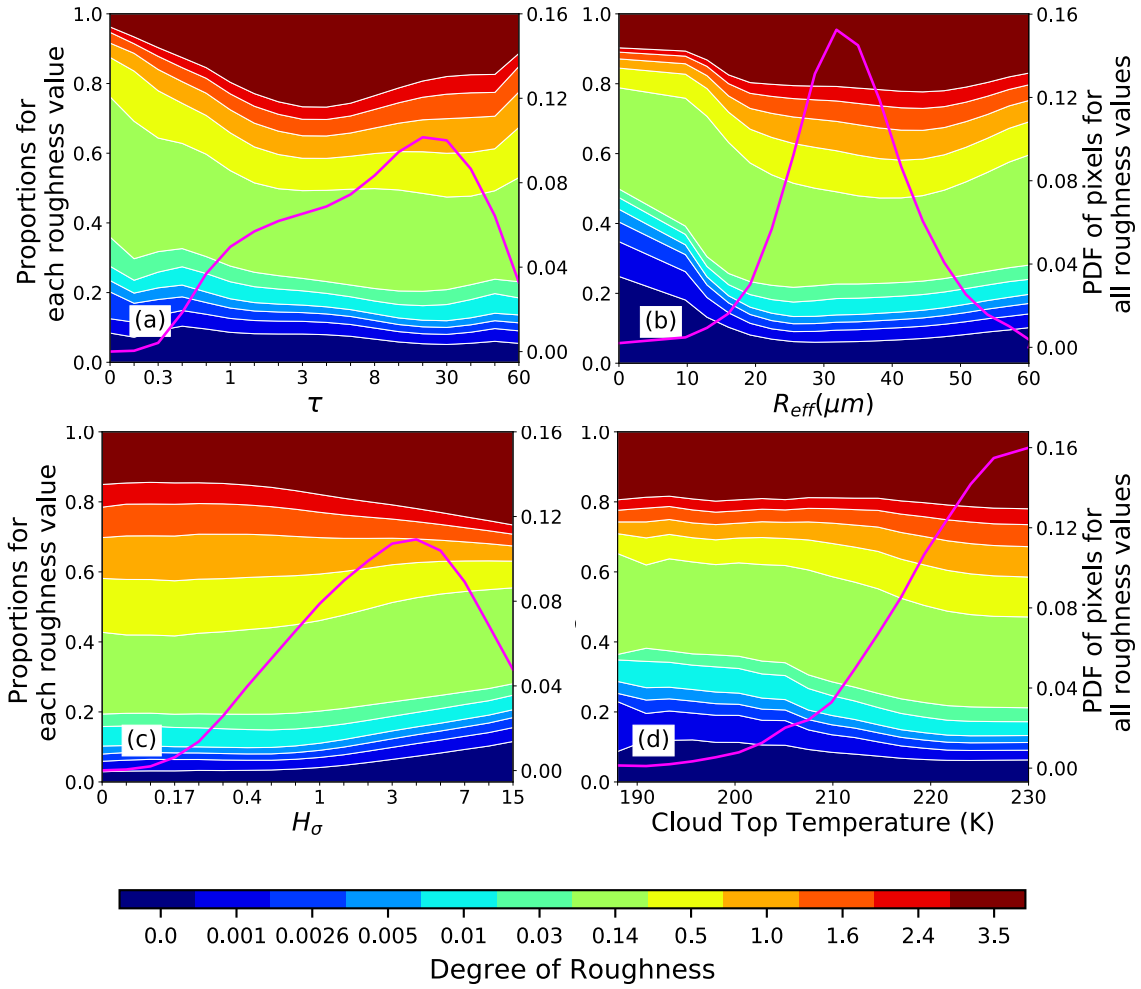

Figure 3.6 The percentages of retrieved best-fit ice particle roughness models are shown for ranges of four ice cloud property variables over the ocean: (a) ice cloud optical thickness (τ), (b) cloud particle effective radius (R_{eff}), (c) cloud heterogeneity index (H_σ), and (d) cloud top temperature. The magenta curve shows the normalized probability of the number of pixels in every bin.

Similar to the case in Fig. 3.6a, the inferred optimal surface roughness value also varies with the effective particle radius in Fig. 6b. Severe roughening (σ^2 >1.0) dominates when the R_{eff} > 10 μm. Since ice particles become less pristine as they grow (Pfalzgraff et al., 2010), the degree of particle surface roughness as R_{eff} increases may be related to the ice particle growth process. It is interesting to note that the percentage of relatively smooth ice particles significantly increases as R_{eff} decreases below 20 μm, which occurs generally when cloud particles grow from their initial small sizes in an environment of low water vapor and with small updraft velocities.

The MODIS products provide cloud top pressure and cloud top height, and these two variables show similar proportions of the particle roughness distribution. Only cloud top temperature is considered here. Figures 6c and 6d show the proportion of the optimal roughness values based on the MODIS values of Hσ and cloud top temperature. The σ^2 =0.14 case is chosen for most pixels as Figs. 3.6c and 3.6d. In Fig. 3.6c, the proportions of every particle roughness cases are almost constant when Hσ < 1, but when Hσ > 1, the proportions of particles with the highest and lowest values of roughening increase with Hσ. In Fig. 3.6d, the proportion of smoother particles increases as cloud top temperature decreases. A higher cloud top is generally colder, and more pixels are identified as containing smooth particles. There are more pixels identified as corresponding to smooth particles at high altitudes than low altitude ice clouds. It should be pointed out that the radiometric signals for the retrievals in all these cases are largely from the top of the cloud. Lower portions of optically thick ice clouds are expected to have different properties than the cloud tops.

Figure 3.7 shows that the use of the optimal ice model in retrievals improves the consistency between model reflectance and measured reflectance in every bin. The blue vertical bars denote the 25 to 75 percent range of computed χ^2 for the pixels within each bin for each parameter discussed in Fig. 3.6. The blue dots denote the median χ^2 value computed with the MC6 model. The red bars and dots denote the 25 to 75 percent range of computed χ^2 for the pixels within each bin computed using the optimal model. The magnitudes of χ^2 vary with every variable, but all χ^2 values based on the optimal model are smaller than the MC6 results. This means that the model reflectances generated based on optimal model have better consistency with measurements.

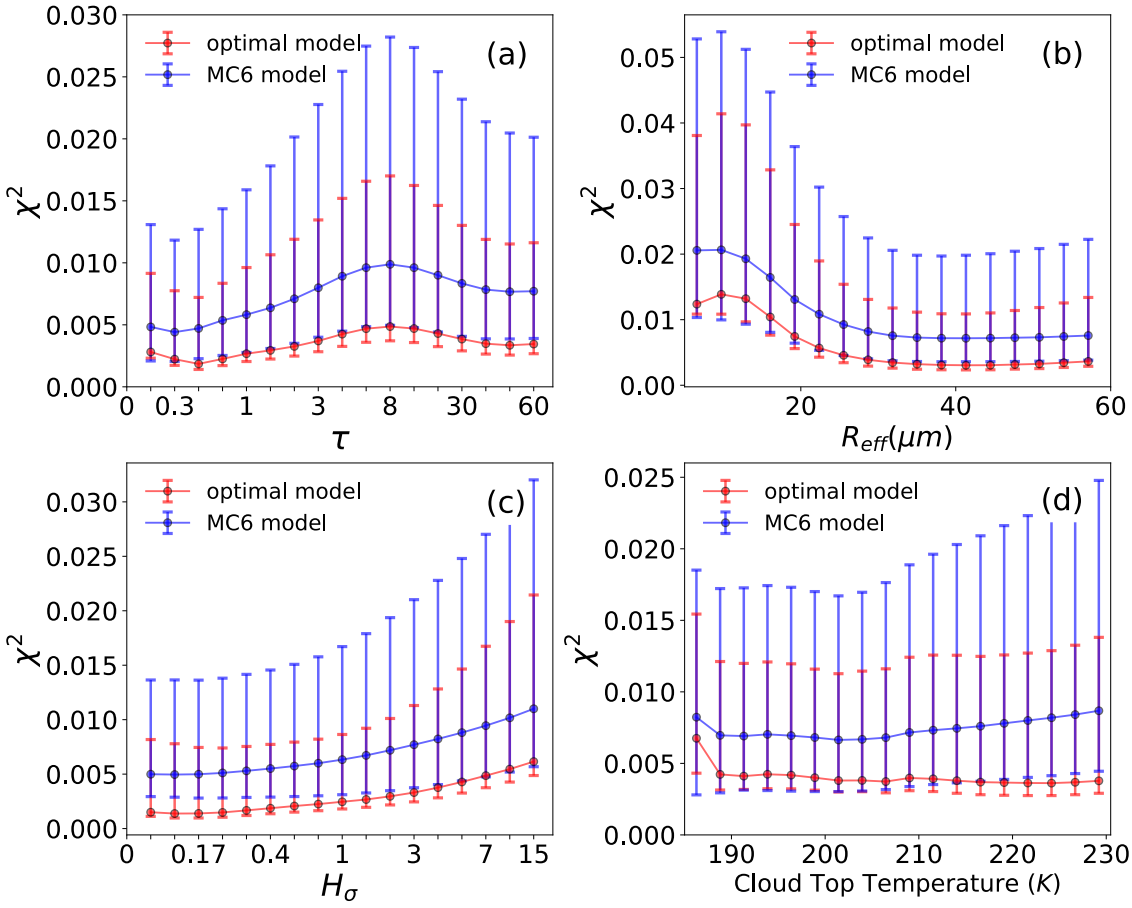

Figure 3.7 The standard deviations (in quadrature) between measured reflectance and model reflectance (χ^2) obtained using the optimal model and MC6 model for (a) ice cloud optical thickness (τ), (b) effective radius (R_{eff}), (c) cloud heterogeneity index (H_σ), and (d) cloud top temperature.

In Fig. 3.7a, χ^2 generally increases with increasing τ up to a peak value at τ ~8, after which it decreases. For R_{eff} (Fig. 3.7b), χ^2 generally decreases with increasing R_{eff}. In comparing the results of Fig. 3.7b with Fig 3.6b, the R_{eff} bin with the maximum χ^2 values occurs in the same range where the optimal ice particle model becomes slightly roughened. The high χ^2 values of both the MC6 and optimal models for $R_{eff} < 20$ μm indicate that neither model leads to consistency with measurements. Because the χ^2 values decrease when $R_{eff} > 20$ μm, it may be a rational hypothesis that the hexagonal aggregate ice particle habit better reproduces the observed reflectivities in regions of larger R_{eff} values.

Figure 3.7c shows that χ^2 increases as Hσ increases. It was noted earlier that the proportions of both the most and least roughened particles increase with increasing Hσ, (Fig. 3.6c). High values of Hσ suggest that 3D effects could be important.

In Fig. 3.7d, χ^2 values increase slightly with increasing ice cloud top temperatures when the MC6 model is used, but is invariant for the case of the optimal model. Note that the results in Fig. 3.6d show that the percent of roughened particles slightly increases with increasing cloud top temperature, with the largest percentage of smooth particles occurring at the coldest temperatures. Our results suggest that colder clouds tend to have fewer roughened particles. A rougher ice particle surface results in a smoother phase function over the scattering angle range covered by the MISR cameras as mentioned in Chapter 3.2. In addition to ice particle surface roughness, other factors (such as air bubbles) can also smooth the phase function (Tang et al., 2017). Therefore, more ice particles are smooth in colder ice clouds may not be the only reason to explain these features. Ice

crystals containing air bubbles in colder clouds may be able to show similar characteristics as Figs. 3.6d and 3.7d.

To summarize the results of Fig. 3.7, the χ^2 values based on the optimal model are always lower than those based on the MC6 model. Clouds with high heterogeneity bear further investigation as the χ^2 values increase. Furthermore, the high χ^2 values at low values of R_{eff} suggest that further improvements in the model may be necessary. In addition, the camera selection also has an effect on retrievals (Liang and Di Girolamo, 2013; Miller et al., 2018). With the different viewing zenith angle of each camera, the selected range of scattering angle in retrieval changes with different camera selection, but not measurements at every scattering angle are able to effectively distinguish the different ice models. Therefore, the percent of retrieved roughened ice particles could be affected by the camera selection.

3.3.2. Retrievals with the optimal ice model

This section focuses on cloud property retrievals using the optimal roughness model, and specifically with looking at the variability of τ, R_{eff}, and IWP as a function of $H\sigma$ and cloud top temperature. For each pixel, the degree of roughness that is most consistent with MISR measurements is employed to retrieve ice cloud optical thickness (best-fit τ) and effective radius (best-fit R_{eff}) using the Nakajima-King bispectral retrieval algorithm. The ice water path (IWP) is computed from the retrieved τ and R_{eff}. Here, the IWP is defined in Equation (3.1) (Horváth and Davies, 2007):

$$IWP = \frac{4\rho\tau R_{eff}}{3Q_e} \quad 3.1)$$

where ρ is the density of ice, and Qe is the average extinction efficiency for ice. Here, we have assumed ρ of 0.93 g cm-3 and Qe is set to 2. For the same samples analyzed from the fused MISR-MODIS data product, the corresponding MC6 τ and Reff retrievals are examined as a reference.

We first examine the relation between Hσ and cloud top temperature (Fig. 3.8). Figure 3.8a shows that the highest percentage of pixels occurs with the warmest cloud top temperatures. The vertical profile of Hσ in Fig. 3.8b shows that Hσ is fairly constant but decreases when the cloud top temperature < 190 K, which could be a factor related to low sampling. The median Hσ is around 3 except at extremely low cloud top temperatures < 190K, which suggests that Hσ is not dependent on latitude.

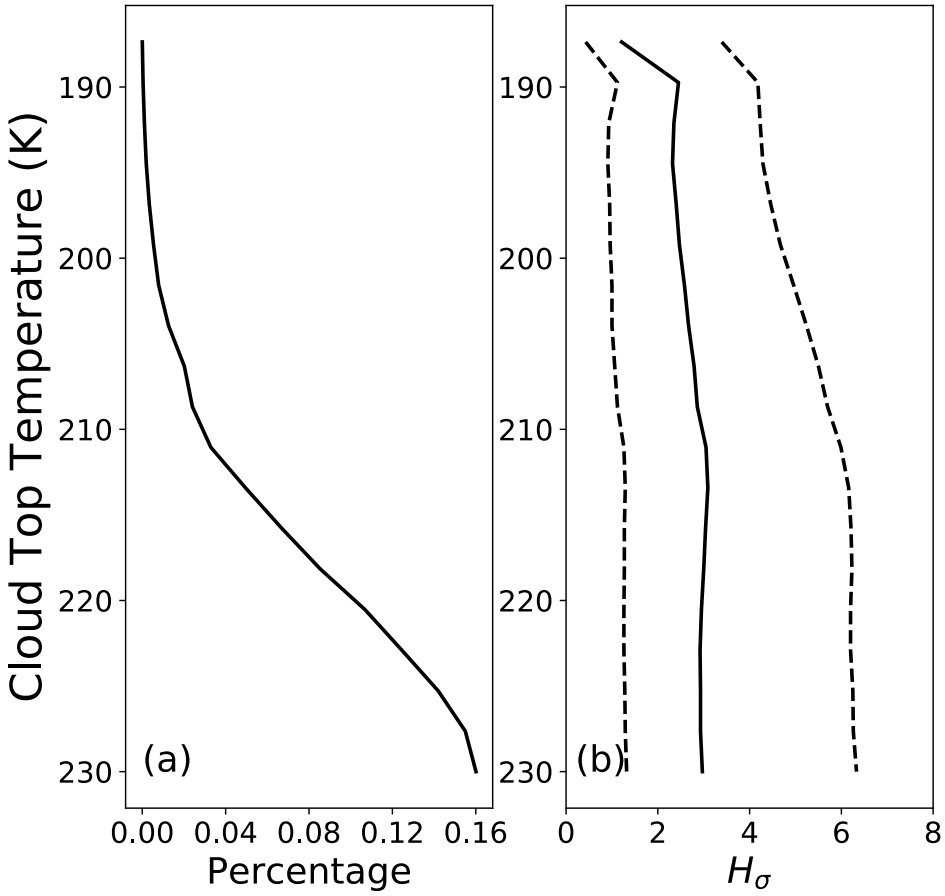

Figure 3.8 (a) The proportion of ice cloud pixels, and (b) the median cloud heterogeneity index (H_σ) value (solid is median and dashes are upper and lower quartiles) as a function of cloud top temperature.

Figure 3.9 shows the retrievals (i.e., τ, Reff, and IWP) based on the optimal and MC6 models for multiple Hσ regimes (left column) and cloud top temperature (right column). Clouds with high Hσ values are likely to have lower τ and low IWP, although we note that the R_{eff} is largely invariant with Hσ. The retrievals do not show significant variations in cloud top temperatures except extremely cold clouds. For all bins in both regimes, the optical thickness retrieved by the optimal model is higher than retrieved by the MC6 model, and their absolute differences increase with higher optical thickness and lower Hσ regimes. The median value of τ of all pixels using the optimal model is higher than with the MC6 model by 10.1%. The median value of R_{eff} using the optimal model is 2 μm lower than with the MC6 model for almost all cases. The median value of R_{eff} of all pixels using optimal model is smaller by 6.5%. The impact on IWP is fairly small, which is reasonable considering it is a product of τ and R_{eff}.

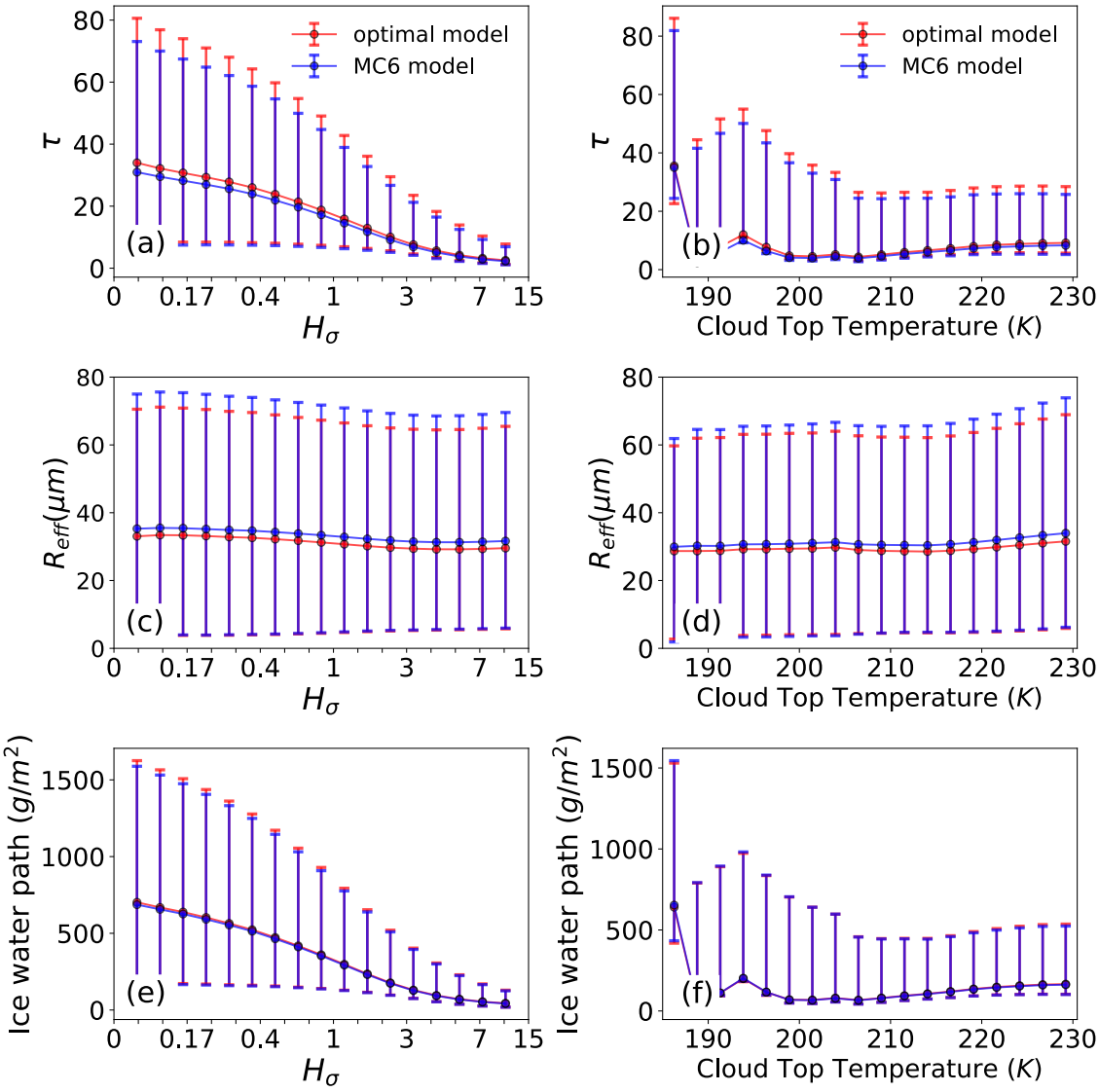

Figure 3.9 The median retrieved ice cloud optical thickness (τ), cloud particle effective radius (R_{eff}), and ice water path using the optimal model and MC6 model over the range of values for the cloud heterogeneity index (H_σ) and cloud top temperature.

Fig. 3.9a shows that the retrieved τ decreases with increasing Hσ. This indicates that the thin clouds are likely to have high Hσ values. In other words, the different Hσ regimes are similar to the optical thickness regimes. As shown in Fig. 3.8b, clouds with different cloud top temperatures have similar Hσ distributions, suggesting that the high Hσ clouds mainly come from optically thin clouds with large reflectance variations. This also explains why Fig. 3.6c has a roughly inverse roughness distribution in comparison with the case in Fig. 3.6a.

3.3.3. Seasonal Cycles of Retrievals and its Potential Implications

Recent studies of seasonal differences show inconsistent annual cycles using different ice particle models for the retrievals (Zhang et al., 2009; Zeng et al., 2012). As mentioned in Section 2, χ^2 value quantifies the difference between the simulations and the multi-angle imaging measurements for an ice particle model. In this section, we investigate the seasonal cycle of retrievals using the optimal model.

The seasonal cycles (monthly averages in 2013) over the ocean of τ, R_{eff}, and IWP are shown in Fig. 3.10, separately for the tropics (0°-30° latitude) and the mid-latitudes (30°-60° latitude) in each hemisphere. The seasonal cycles are calculated using both the optimal model (red) and the MC6 model (blue). The optical thickness retrievals from the two models have similar regional and monthly variations, but τ from the optimal model is slightly higher than MC6 in all months (Figs. 3.10a and 3.10b). The τ values from the optimal model are both higher in local summer than other seasons in most cases, and lower in the tropics than in the mid-latitudes for each hemisphere. However, the seasonal characteristics in the Southern and Northern Hemispheres are not completely symmetrical.

Note that τ is higher in the mid-latitudes of the Northern than the Southern Hemisphere in most months, but is similar across the tropical region of both hemispheres.

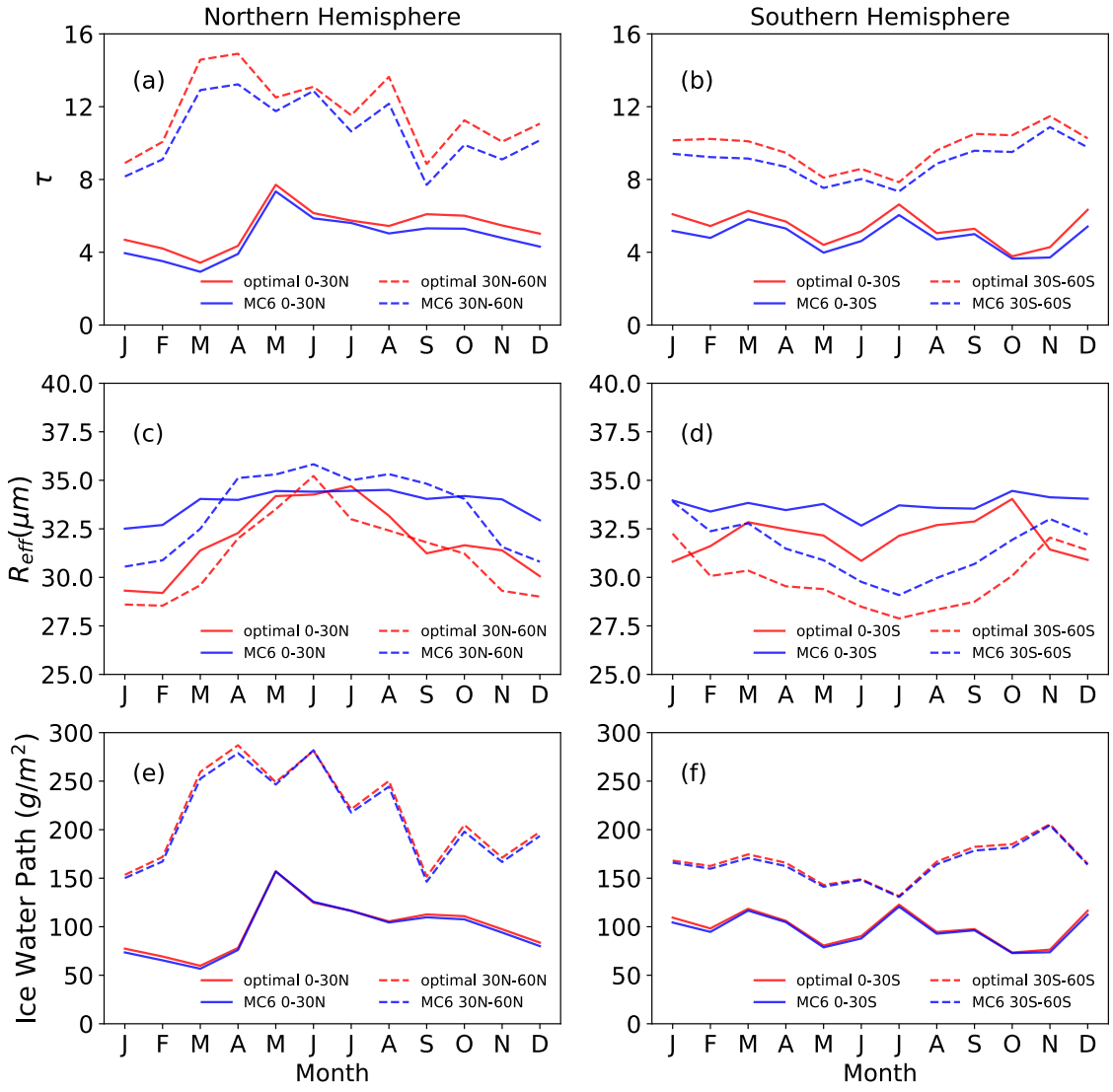

Figure 3.10 The annual cycles (monthly averages in 2013) of retrieved ice cloud optical thickness (τ), cloud particle effective radius (R_{eff}) and ice water path using the optimal model and MC6 model averaged over the tropics (0-30° latitude) and the mid-latitudes (30°-60° latitude) for both hemispheres.

Figures 3.10c and 3.10d show retrievals of R_{eff} in the same form as in Figs. 10a and 10b. The optimal model retrievals have a smaller R_{eff} than the MC6 retrievals in most cases. The R_{eff} from both models tend to be higher in the spring and summer than in winter for each hemisphere in most regions, but the best-fit R_{eff} have larger seasonal variations than the MC6 model. For IWP (Figs. 3.10e and 3.10f), the differences between these two ice model retrievals are insignificant. Both retrievals have a higher IWP in local summer as expected due to increased convection, and have a higher IWP values in mid-latitudes than the tropics.

Figure 3.11 shows the normalized frequency distributions of the retrieved τ and R_{eff} associated with the MC6 model and the optimal roughness model for the four meteorological seasons over the ocean, Mar-May (MAM), Jun-Aug (JJA), Sep-Nov (SON), and Dec-Feb (DJF). The averaged distributions of τ and R_{eff} indicate that there are minimal differences in each season. However, the maximum frequency distributions produced with the MC6 model and the optimal model have some systematic differences. The distribution of τ does not shift, but the maximum of the distribution for the best-fit τ peak has a lower frequency by approximately 10% in comparison with the MC6 results for all seasons, compensated for by a slightly higher tail in the large τ direction for the best-fit τ. This feature may be explained by a slightly larger number of cases with large τ. The histogram distributions of the best-fit R_{eff} are systematically smaller (2-4 μm) than for the MC6 counterpart in all seasons.

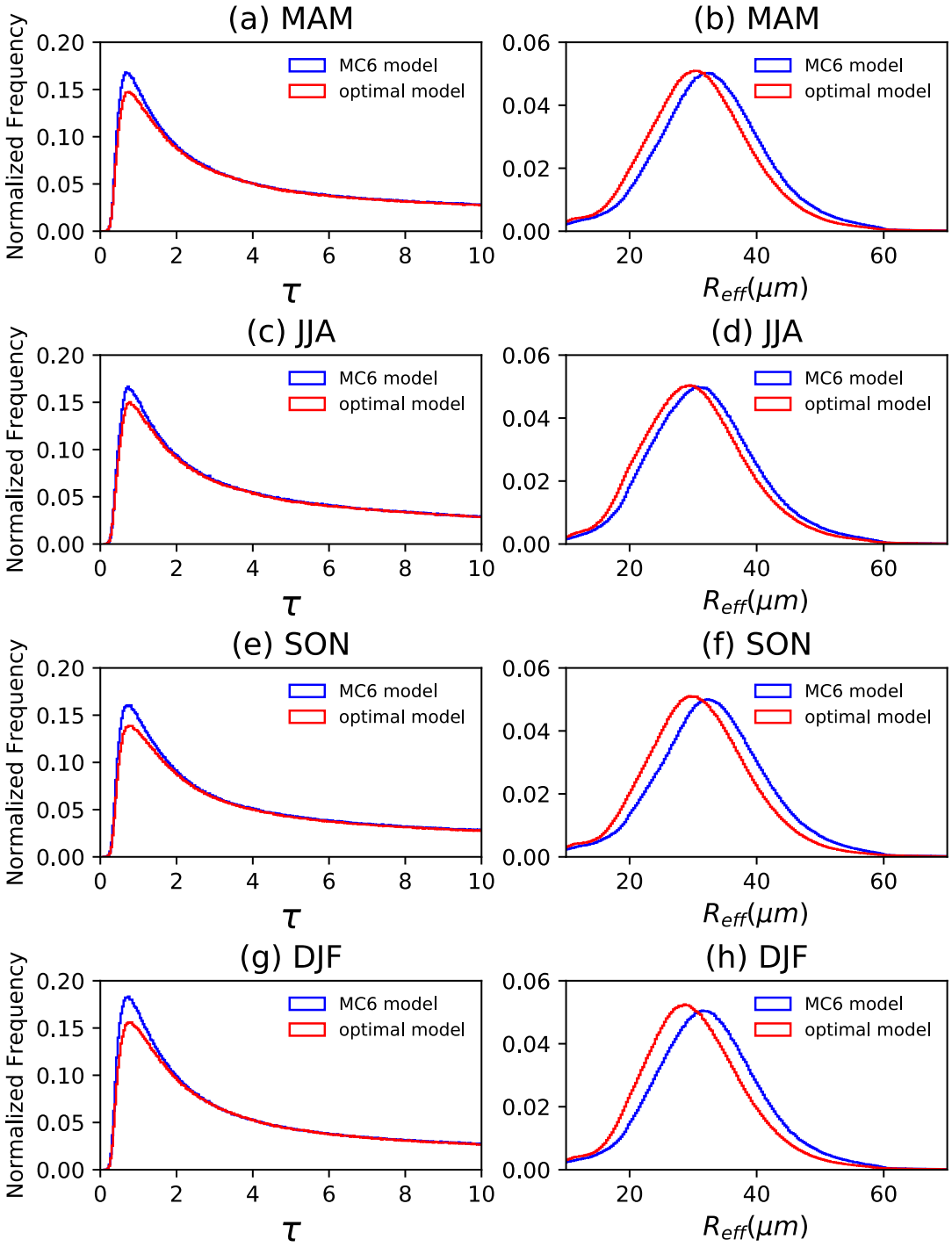

Figure 3.11 The seasonal normalized frequencies of retrieved ice cloud optical thickness (τ) and cloud particle effective radius (R_{eff}) obtained from the optimal model and MC6 model. The results are averaged globally for each season (MAM: Mar-May, JJA: Jun-Aug, SON: Sep-Nov, and DJF: Dec-Feb).

The bi-spectral shortwave technique for retrieving τ and R_{eff} is sensitive to the asymmetry factor (King, 1987) and the details of the scattering phase function (Doutriaux-Boucher et al., 2000; Zhang et al., 2009). Therefore, the retrieved τ and R_{eff} are dependent on the assumed ice particle model, and the selection of an optimal ice particle model is critical to robust cloud property retrievals using a visible band and a shortwave infrared band. As stated above, most cloud products assume a single ice model in retrieval, but cause inconsistency with measurements if using an invariant ice particle model. In this study, optimal model retrievals using a pixel-level variable ice model show more consistency with the multi-angle direction measurements than retrievals using the invariant ($\sigma 2 = 0.5$) MODIS MC6 model. Because of the better consistency, retrievals based on the variable roughness model in conjunction with multi-angle measurements leads to a better fit to cloud properties at the pixel level. Therefore, the differences between optimal model retrievals and the operational MODIS satellite retrieval products provide a possible approach to the retrieval biases.

As seen in Fig. 3.10 and Fig. 3.11, different seasonal variations and normalized frequencies exist in the comparison of τ and R_{eff} retrieved using the variable roughness model and the invariant roughness MODIS MC6 model. Since τ and R_{eff} play a significant role in cloud albedo and transmittance (Platnick and Oreopoulos, 2008), the inconsistency of τ and R_{eff} among different remote sensing retrievals will impact assessing the cloud radiative forcing, and is also an important quantity in climate study.

3.4. Summary

This study investigated the retrieved ice cloud optical thickness (τ), effective radius (R_{eff}) and ice water path (IWP) over ocean under different τ, R_{eff}, cloud heterogeneity index (Hσ) and cloud top temperature regimes, and computes their annual cycles in different latitude bands using a full year (2013) of fused MISR-MODIS data with a varying ice particle roughness model. A varying roughness model is used to choose the optimal roughness value for a given pixel, leading to a better delineation of the variations of optical and microphysical properties over the wide range of scattering angles measured by MISR. In particular, the retrievals in this study provide a better understanding of retrieved ice cloud τ and R_{eff} in MC6 products, computed by assuming an invariant ice particle model in the retrieval algorithm.

Measurements are better explained by assuming severely roughened ice particles for many pixels when τ and R_{eff} are large, a larger cloud heterogeneity index (Hσ), and warmer ice cloud-top temperatures. The proportion of severely roughened particles increases rapidly with increasing τ in thin cloud regimes, but not for thick clouds. The proportion of smooth particles significantly decreases when $R_{eff} > 20$ μm. Compared to the MODIS C6 operational retrievals, the retrievals in this study with the varying roughness model improve the consistency between model reflectances and measurements, and have a larger value of τ and a smaller value of R_{eff} in most cloud regimes. The median value of τ of all pixels is larger by 10.1% than the MC6 counterparts and median value of R_{eff} is smaller by 6.5%. However, IWP does not show significant differences between these two retrievals.

The zonal median values of the retrieved τ and R_{eff} using the variable roughness model in this study are different from the MC6 constant roughness model, and the differences vary with the season. The retrievals of τ from the two models have similar regional and monthly variations. However, a larger annual cycle appears in R_{eff} in the optimal model retrievals than in the MC6 retrievals. The normalized frequency distributions of τ by these two retrievals show that the peak location of best-fit τ is close to that of MC6 τ, but the peak frequency of best-fit τ is lower by approximately 10% in all seasons. The normalized frequency distribution of the best-fit R_{eff} is systematically shifted toward a smaller value of R_{eff} by 2-4 μm in comparison with the results for the MC6 R_{eff} in all seasons.

4. REMOTE SENSING ICE PARTICLE MODEL FOR CIRRUS CLOUDS: METHODOLOGY AND VIEWING ANGLE DEPENDENCE IN RETRIEVALS USING AIRBORNE MULTI-ANGLE POLARIZATION MEASUREMENTS

We present an improved remote sensing technique to infer an optimal habit/shape model for ice particles in cirrus clouds using multi-angle polarimetric measurements made by the Airborne Multi-angle SpectroPolarimeter Imager (AirMSPI) instrument. The common method of ice model inference is not appropriate for inferring thin ice models (i.e., cirrus clouds) using polarization measurements. This improved method is able to infer an ice model in clouds with optical thicknesses smaller than 5. The improvement is made by assuming the optical thickness retrieved using total reflectivity and then computing polarized reflectivity and generating look-up tables of simulated polarized reflectances computed for cirrus clouds in conjunction with eight ice particle models. The ice particle model that leads to the closet fit to measurements is regarded as the optimal ice particle model. Meanwhile, an alternative method without considering polarized reflectivity is also applied. Both methods are applied to a case of measurements of cirrus clouds to retrieve an optimal ice particle model. The hexagonal column aggregate model works for most pixels both with and without considering polarized reflectivities. The number of camera pairs selected has a smaller effect on ice particle habit retrievals than the effect of selecting forward or aft cameras. Specifically, when camera pairs with large zenith angles are excluded, the inconsistency between observations and simulated total or

polarized reflectivity significantly decreases and the inferred ice particle model does not change in this study case.

4.1. Introduction

The selection of an appropriate ice particle habit model and subsequent generation of the corresponding bulk single-scattering properties are critical to the implementation of cirrus cloud property retrievals and, subsequently, to the assessment of the cirrus radiative forcing effect (Mishchenko et al., 1996; Baran et al., 2009; Yang et al., 2015; Loeb et al., 2018). To infer appropriate ice particle model(s) in ice cloud property retrievals, satellite or airborne multi-angle imaging sensors including the POLarization and Directionality of the Earth's Reflectances (POLDER) and Multi-angle Imaging SpectroRadiometer (MISR) instruments as well as similar airborne instruments are commonly applied. These sensors use fixed cameras to view a given pixel at multiple angles along the satellite or airplane path. This sampling configuration provides the unprecedented opportunity to evaluate the reconcilability between ice particle model and measurement over a range of scattering angles.

Based on these unique directional viewing characteristics from multi-angular observations, retrieval techniques using total reflectivity from multi-angular observations have been implemented to validate ice habit models and surface morphology such as roughening (Doutriaux-Boucher et al., 2000; McFarlane et al. 2005; Xie et al. 2012; Wang et al., 2018). Meanwhile, polarimeter measurements from multi-angular observations have been applied to infer ice particle habits (Chepfer et al., 2001; Sun et al., 2006; Baran and C.-Labonnote, 2007; van Diedenhoven et al., 2012; Cole et al., 2014; Hioki et al., 2016).

The polarimetric reflectivities are able to predict all elements of the scattering matrix instead of P11 element only for cloud properties. In employing this method, assuming a constant optical thickness of 5 or larger is necessary to generate look-up tables (LUTs) in doing retrievals. The reason for this is that polarimetric reflectivities saturate at an optical thickness of approximately 5 (Masuda and Takashima, 1992; also see Section 2.2), beyond which multiple scattering swamps the signal. This treatment clearly distinguishes ice particle habit signals for optically thick ice clouds, but does not work well for ice clouds with optical thicknesses less than the polarization saturation threshold. Since the typical optical thickness of cirrus is less than 3, it is necessary to improve the conventional retrieval method that only considers thick ice clouds.

The primary goal of this paper is to demonstrate an algorithm to determine ice particle models for optically thin ice clouds using multi-angular polarimetric reflectivity data, which overcomes the constraints on the optical thickness. In doing so, this study also assesses camera selection in a multi-angular retrieval technique. Commonly, satellite products are retrieved based on all available cameras, since more cameras carry more information, and the viewing geometries (i.e., viewing zenith angle and viewing azimuth angle ranges) of each camera are not the same with different multi-angular imaging satellites. Several studies indicate that viewing geometries may influence cloud retrievals due to various factors, such as varying influences of the cloud 3D effect on each camera and variable sensitivity of the ice model to viewing geometries (McFarlane and Marchand 2008; Liang and Di Girolamo, 2013; Zhang et al., 2009; Wang et al., 2018). Therefore, it is necessary to understand the impact of selecting cameras on retrievals.

4.2. Methodology

4.2.1. Ice Habit Models

Four ice particle habits are chosen in this study, including a bullet rosette, an aggregate of 10 plates, a solid hexagonal column, and an aggregate of 8 hexagonal columns. Details of ice particle habits are defined in Yang et al. (2013). For each ice particle habit, two ice particle models with different single scattering properties are computed, one assuming a smooth particle (σ^2=0) and the other for a roughened particle (σ^2=0.5). Roughness is the random tilting of ice particle faces with a Gaussian distribution and is denoted by σ (see Yang and Liou (1998) for the detailed explanation of the physical meaning of this parameter). The addition of roughness to the ice particle surface results in a featureless phase function, thereby leading to a reduction of the halo peaks. Several studies (Baran 2009; Wang et al., 2018) demonstrate that rough ice cloud models are able to achieve spectral consistency in the retrieved ice cloud optical thickness. Note that a roughness factor of σ^2=0.5 is used for operational MODIS (Moderate Resolution Imaging Spectroradiometer) Collection 6 (MC6) products, and the roughened 8 hexagonal column aggregate ice habit in this study is the same as that used for the MC6 ice model. The effective variance is 0.1 and an effective radius is 30 μm in computing bulk scattering properties with integrating single-scattering properties over a Gamma distribution for all 8 ice particle models. In addition, three liquid water models are used in this study to distinguish the cloud phase. The three water models are computed with the Lorenz-Mie theory with respect to three different effective radii (R_{eff} = 4 μm, 8 μm, and 16 μm). The

nonzero scattering phase matrix elements (P11 and P12/P11) of the 11 cloud particle models (8 ice models and 3 water models) in this study are shown in Figure 4.1.

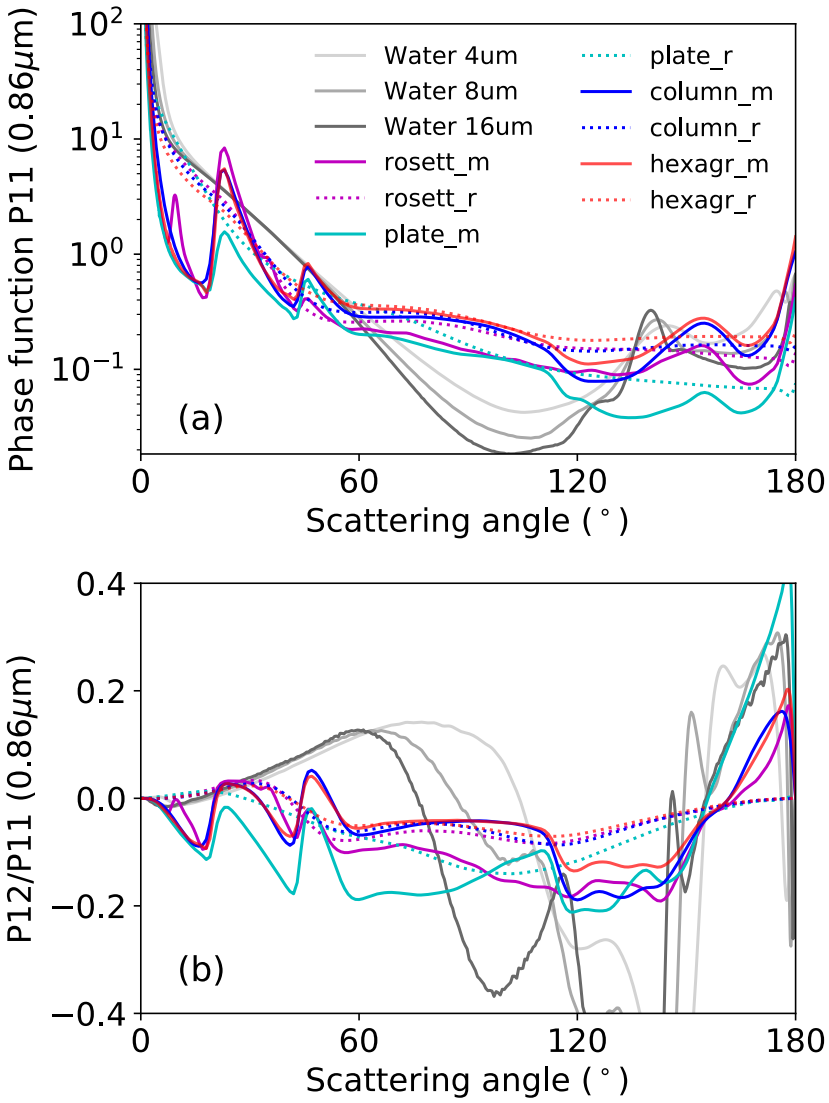

Figure 4.1 The a) phase function and b) P12/P11 phase matrix elements as functions of scattering angle for 8 ice particle models and 3 liquid water models with different effective radii (R_{eff} = 4 μm, 8 μm, and 16 μm) used in this study. The 8 ice particle models are 4 ice particle habits, which are bullet rosette (rosett in the figure), 10 plates aggregate (plate), solid hexagonal column (column), and 8 hexagonal columns aggregate (hexagr) with smooth surface (m) and roughened surface (r) particles computed separately for each habit.

4.2.2. Algorithm

The reflectivity (R; also named total reflectivity) is defined as:

$$R(\mu, \mu_0, \varphi, \varphi_0) = \frac{\pi \cdot d^2 \cdot I(\mu,\mu_0,\varphi,\varphi_0)}{\mu_0 \cdot E_0} \quad 4.1)$$

where $I(\mu, \mu_0, \varphi, \varphi_0)$ is the radiance, E_0 is the solar irradiance at 1 astronomical unit (AU), and d is the Earth-Sun distance relative to 1AU. φ and φ_0 are viewing azimuthal angle and solar azimuthal angle. The factors μ and μ_0 are the cosines of the viewing zenith angle and solar zenith angle, respectively.

In a similar manner, the polarized reflectivity (L) is defined as:

$$L(\mu, \mu_0, \varphi, \varphi_0) = \frac{\pi \cdot d^2 \cdot \sqrt{Q(\mu,\mu_0,\varphi,\varphi_0)^2 + U(\mu,\mu_0,\varphi,\varphi_0)^2}}{\mu_0 \cdot E_0} \quad 4.2)$$

where Q and U are the second and third Stokes parameters, respectively.

In radiative transfer theory, total reflectivity has a one-to-one relationship with optical thickness. However, the polarized reflectivity no longer changes with optical thickness when $\tau > 5$, i.e., the signal reaches saturation (Masuda and Takashima, 1992). Figure 4.2 shows the total reflectivity and polarized reflectivity as a function of optical thickness, corresponding to the typical scattering geometry of the AirMSPI nadir camera (000N; see Chapter 4.3.1) applied here. The total reflectivity increases with τ in Figure 4.2a, but in Fig 4.2b, the polarized reflectivity increases with optical thickness (τ) until τ=2, and then decreases. This feature indicates not all scattering geometry polarized reflectivities have a monotonically increasing relationship with cloud optical thickness. After $\tau > 5$, the polarized reflectivity has no obvious variations. The polarized reflectivity shows significant differences among ice models when $\tau > 5$, and many studies use this

feature to investigate ice particle habit (Sun et al., 2006; van Diedenhoven et al., 2012; Cole et al., 2014; Hioki et al., 2016). Because the polarized reflectivity changes with τ when $\tau < 5$, it is not appropriate to assume a constant optical thickness in the study of cirrus clouds. Therefore, in this study, the computed optical thickness for both $\tau < 5$ and $\tau \geq 5$ is updated with the optical thickness inferred from the total reflectivity. A similar treatment is implemented by van Diedenhoven et al. (2012) to infer the aspect ratio and the degree of the surface roughness of ice particles for $\tau < 5$.

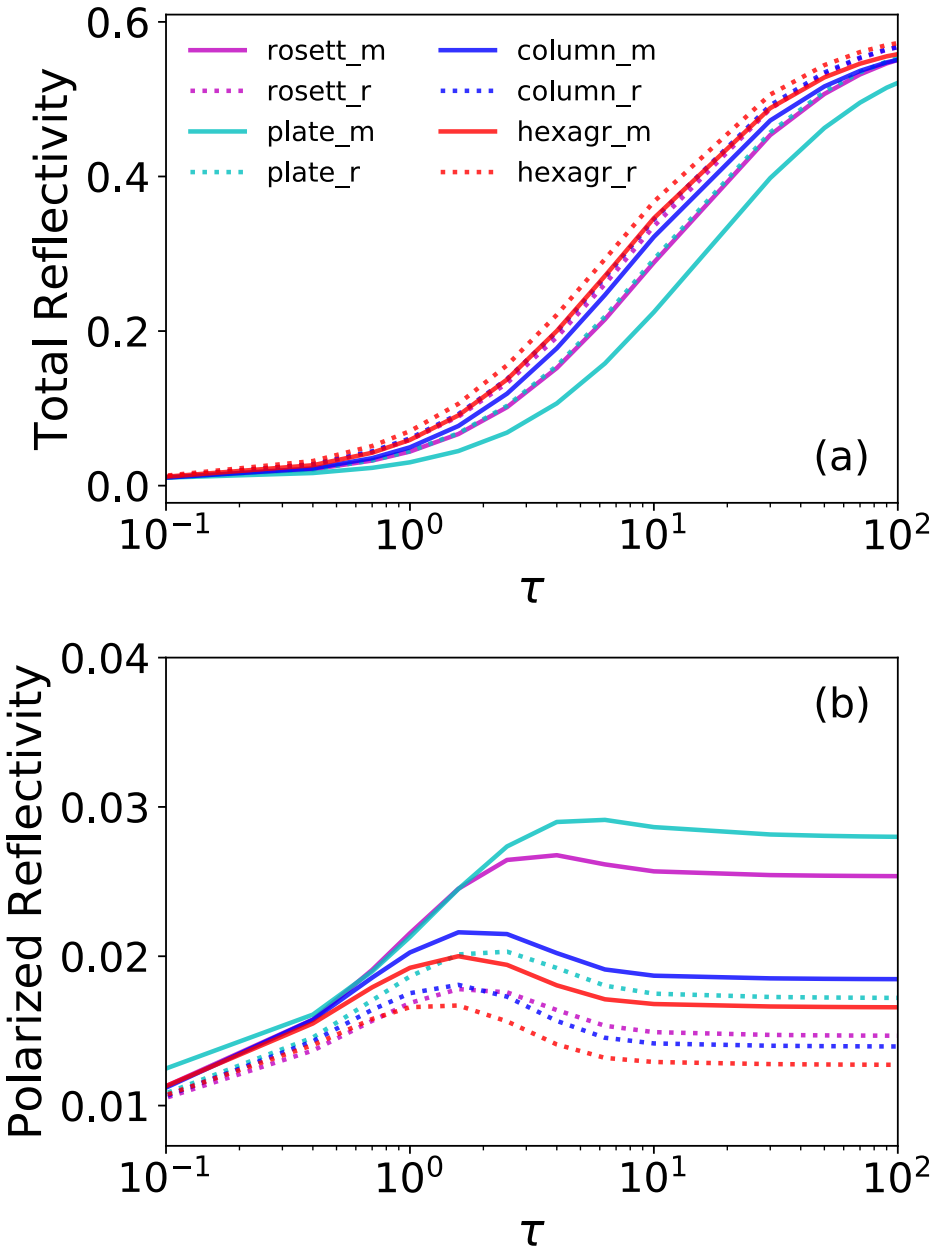

Figure 4.2 The a) total reflectivity and b) polarized reflectivity as functions of cloud optical thickness for ice particle models used in this study. The geometry angles (solar zenith angle of 51.5°, viewing zenith angle of 0°, and relative azimuthal angle of 130°) of the AirMSPI nadir camera (000N) in the chosen case study are assumed here.

Figure 4.3 shows the flow chart for inferring an optimal ice particle model in this study using both two retrieval methods. Look-up tables (LUTs) are computed for each cloud model by using an adding-doubling radiative transfer model with polarization capability (Huang et al., 2015). This retrieval system assumes a single homogenous cloud layer, considers atmospheric molecular scattering, but neglecting aerosols. The ocean surface reflection is computed based on a rough ocean surface model (Cox and Munk, 1954). Given the scattering geometry (i.e., solar zenith angle, viewing zenith angle, and relative azimuth angle) for each camera, total reflectivity and polarized reflectivity as a function of optical thickness are calculated and stored in each LUT. Due to the one-to-one relationship between optical thickness and total reflectivity, the optical thickness in every LUT is retrieved using the measured total reflectivity from each camera. By assuming the retrieved optical thickness, the polarized reflectivity is computed for each camera using the LUTs.

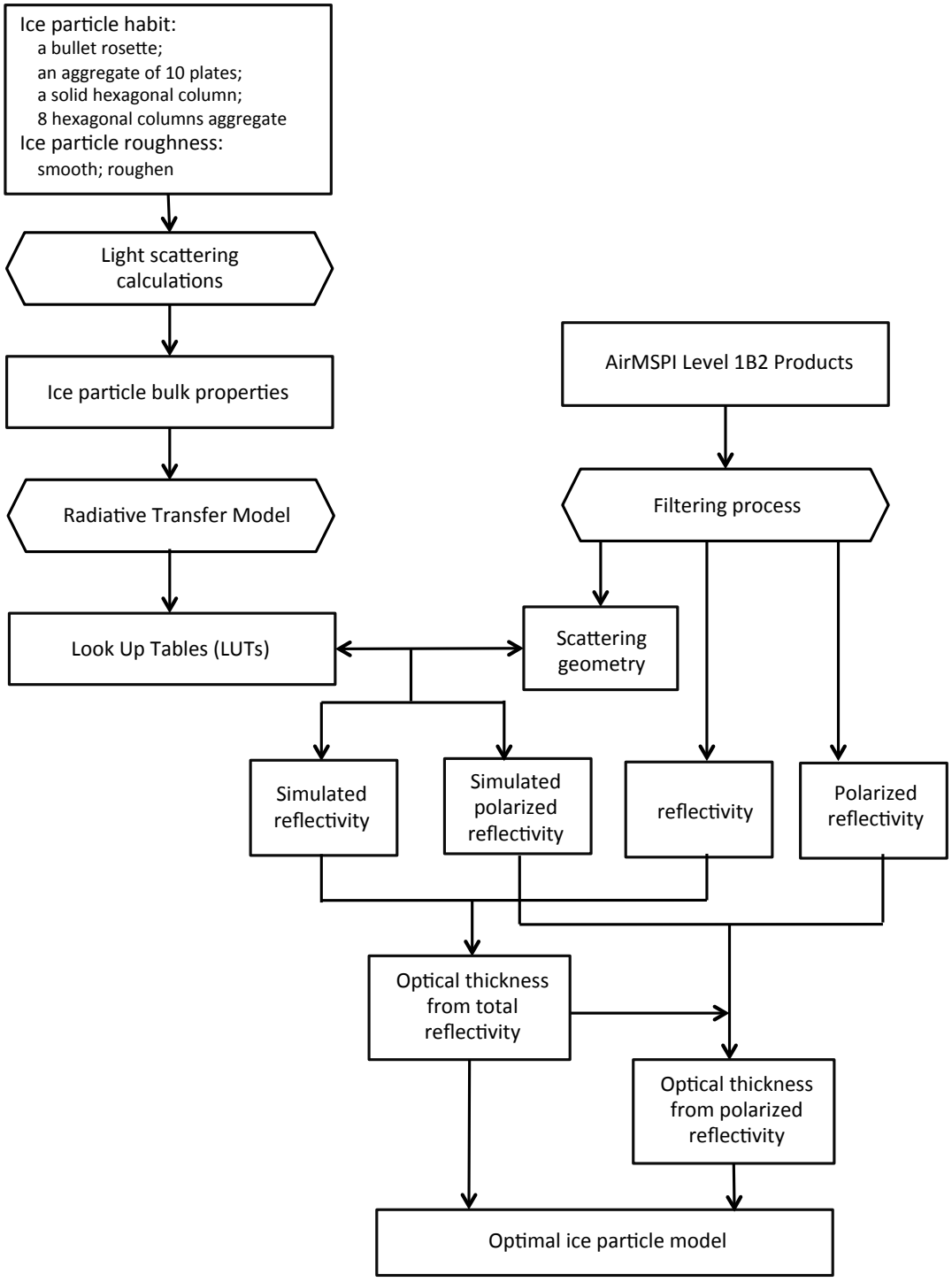

Figure 4.3 The flow chart for inferring optimal ice particle models of cirrus clouds in this study

Furthermore, the optimal ice particle shape is inferred using both total reflectivity and polarized reflectivity measurements. The core idea of evaluating ice model is that the retrieved optical thickness when assuming appropriate ice model should be the same or nearly invariant versus scattering angle. Therefore, the optimal model inferred using total reflectivity is defined as the model that provides the minimum value of the standard deviation of optical thickness retrieved from all selected cameras (s2total).

$$s^2_{total,i} = \sqrt{\frac{1}{N}\sum_{j=1}^{N}(\tau_i - \bar{\tau}_i)^2} \quad 4.3)$$

where i is the selected ice particle model, j is the number of cameras, and N is the number of selected cameras in each pixel. The averaged value of optical thickness (τ) in each pixel is $\bar{\tau}$. A similar method is developed by Doutriaux-Boucher et al. (2000) using the spherical albedo difference method. The spherical albedo difference is the spherical albedo value minus the averaged spherical albedo value of all selected cameras. Here, we apply the optical thickness difference instead of the spherical albedo difference value to see more clearly the optical thickness distributions over the range of scattering angles, since our goal is to develop a methodology that works from optically thin to optically thick ice clouds. Similarly, for polarized reflectivity, the optimal ice particle model is the model with the lowest relative root-mean-squared difference (s2pol).

$$s^2_{pol,i} = \sqrt{\frac{1}{N}\sum_{j=1}^{N}(L_{s,i} - L_m)^2} \quad 4.4)$$

The subscript s indicates the simulation, and the subscript m indicates the measurement.

Because the cloud thermodynamic phase information is not available in the dataset involved in this study, we infer cloud phase and remove water cloud pixels. Specifically, each pixel is retrieved by both ice and water models. If the best-fit model of the pixel is water model, that pixel is identified as water clouds and is removed. To avoid potential complications due to ocean surface reflections, a pixel is removed if its optical thickness based on the nadir camera is less than 0.1.

4.3. Case Study

4.3.1. Observations

The data we used in this study are from Airborne Multi-angle SpectroPolarimeter Imager (AirMSPI) Level 1B2 products. The AirMSPI instrument is fully described in Diner et al. (2013), but briefly, it is a pushbroom camera deployed on NASA's ER-2 high-altitude research aircraft. The camera provides radiometric and polarimetric observations in the ultraviolet, visible, and near-infrared channels. The instrument uses two measuring modes to acquire data: step-and-stare and Sweep. In this study, we only use the data from the step-and-stare mode, which provides measurements with 10 m spatial sampling resolution at 9 viewing angles for each pixel. In the Step-and-stare mode, the camera is pointed at the same target at multiple viewing angles step by step. The 9 directional images are 661F, 589F, 478F, 290F, 000N (camera at nadir), 291A, 478A, 589A, and 661A. The naming convention provides the viewing angle, e.g., 661F means that the camera points in the forward direction with viewing angle of about 66.1° and 661A means that the camera points in the aft direction with a viewing angle of 66.1°.

In the present analyses, the total reflectivity from the 661A camera is much higher than from other cameras, which leads to an extremely high optical thickness in the retrieval process. To avoid potential biases, the 661A camera is not considered in the computation process. Because the 865 nm channel is less affected by a varying ice particle effective radius and corresponds to weak ice absorption, this channel is selected for detailed analysis. Pixels corresponding to viewing angle and sunlight direction within 15° cone are removed to avoid potential sunglint contamination.

Since most studies in the AirMSPI project focus on liquid water clouds, there are few cirrus cases in the AirMSPI dataset. The cirrus case we found in this study occurred at 21:20 UTC January 28, 2013 off the coast of Southern California. For the case presented in this paper, the cirrus is located at latitudes between 31.62°N - 31.68°N and at longitudes between 122.59°W-122.68°W over the ocean.

Figure 4.4 shows the zenith angle and azimuth angle range of the sun and each AirMSPI camera for all pixels in the selected case in this study. The azimuth angle is plotted in degrees clockwise from north. The vectors of both the solar azimuth angle and viewing azimuth angle in AirMSPI are defined as pointing in the direction of photon travel. To better depict the relation between sun location and viewing geometry, the plotted angle is the solar azimuth angle plus 180°. This treatment is for solar azimuth angle only, not for the viewing azimuth angle. The radial distances reflect the zenith angle (solar zenith angle or viewing zenith angle). The color map plots the scattering angle for each pixel. The scattering angle is the propagation direction of the incident light after being scattered by ice particles to the AirMSPI camera. The aft cameras have larger scattering

angles closer to backscattering than the forward cameras because the aircraft flew toward the WNW in this data sample. The scattering angle is smaller for a forward camera with a high viewing zenith angle. However, the ranges of scattering angles overlap for each aft camera, and most aft camera scattering angles are between 130° and 150°.

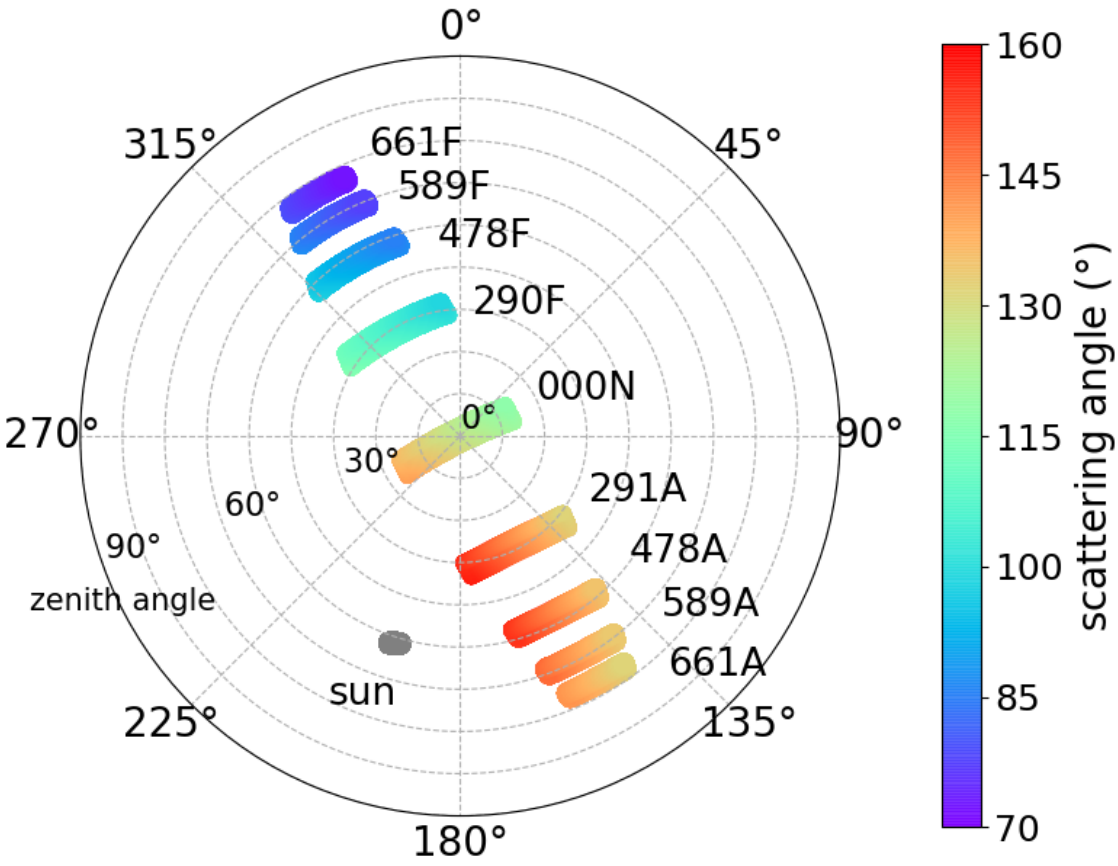

Figure 4.4 The geometry angle range of the sun and AirMSPI camera views in the selected case in this study. The azimuth angle range (solar azimuth angle plus 180° or viewing azimuth angle) and zenith angle (solar zenith angle or viewing zenith angle) are plotted clockwise from north (0°) and radial distance (angle from vertical), respectively. The color bar shows the solar scattering angle for each pixel.

4.3.2. Inference of ice particle shape

We now apply the method proposed in Chapter 4.2.2 to infer the optimal ice habit model. The optimal inferred ice particle shape produced by each camera selection case is shown in Figure 4.5. The ice particle habits in Figure 4.5a and Figure 4.5b are retrieved using total reflectivity and polarized reflectivity in this study case, respectively.

As noted earlier, the viewing geometry angles (i.e., viewing zenith angle, viewing azimuth angle, and scattering angle) are not the same for each camera. The selection of cameras is critical because each camera produces a different satellite retrieval (Liang and Di Girolamo, 2013). To investigate the effect of camera selection on retrievals, the results in Figure 4.5 are retrieved using 10 different camera selection cases. The camera selection of 10 camera cases is listed in Table 4.1. The first four cases include all cameras, but progressively remove the forward and aft pairs with the largest viewing angles. Since each pair of cameras has a different viewing zenith angle, these first four cases demonstrate the viewing zenith angle influence. The first case includes all cameras (except 661A), and the fourth case excludes all cameras with viewing angles > 30°. The other 6 cases focus on the influence of forward and aft camera selections. Cases 5, 6, and 7 use 4, 3, or 2 cameras up to 589F, and cases 8, 9, and 10 use 4, 3, or 2 cameras up to 589A. Case 5 includes the nadir camera and the forward cameras up to 589F, and case 8 uses the nadir camera and the aft cameras up to 589A.

Table 4.1 The camera selection in each group. Cameras with a plus sign are included in a group, and with a minus sign are not included.

Case index	Camera selection								
	661F	589F	478F	290F	000N	291A	478A	589A	661A
1	+	+	+	+	+	+	+	+	-
2	-	+	+	+	+	+	+	+	-
3	-	-	+	+	+	+	+	-	-
4	-	-	-	+	+	+	-	-	-
5	-	+	+	+	+	-	-	-	-
6	-	+	+	+	-	-	-	-	-
7	-	+	+	-	-	-	-	-	-
8	-	-	-	-	+	+	+	+	-
9	-	-	-	-	-	+	+	+	-
10	-	-	-	-	-	-	+	+	-

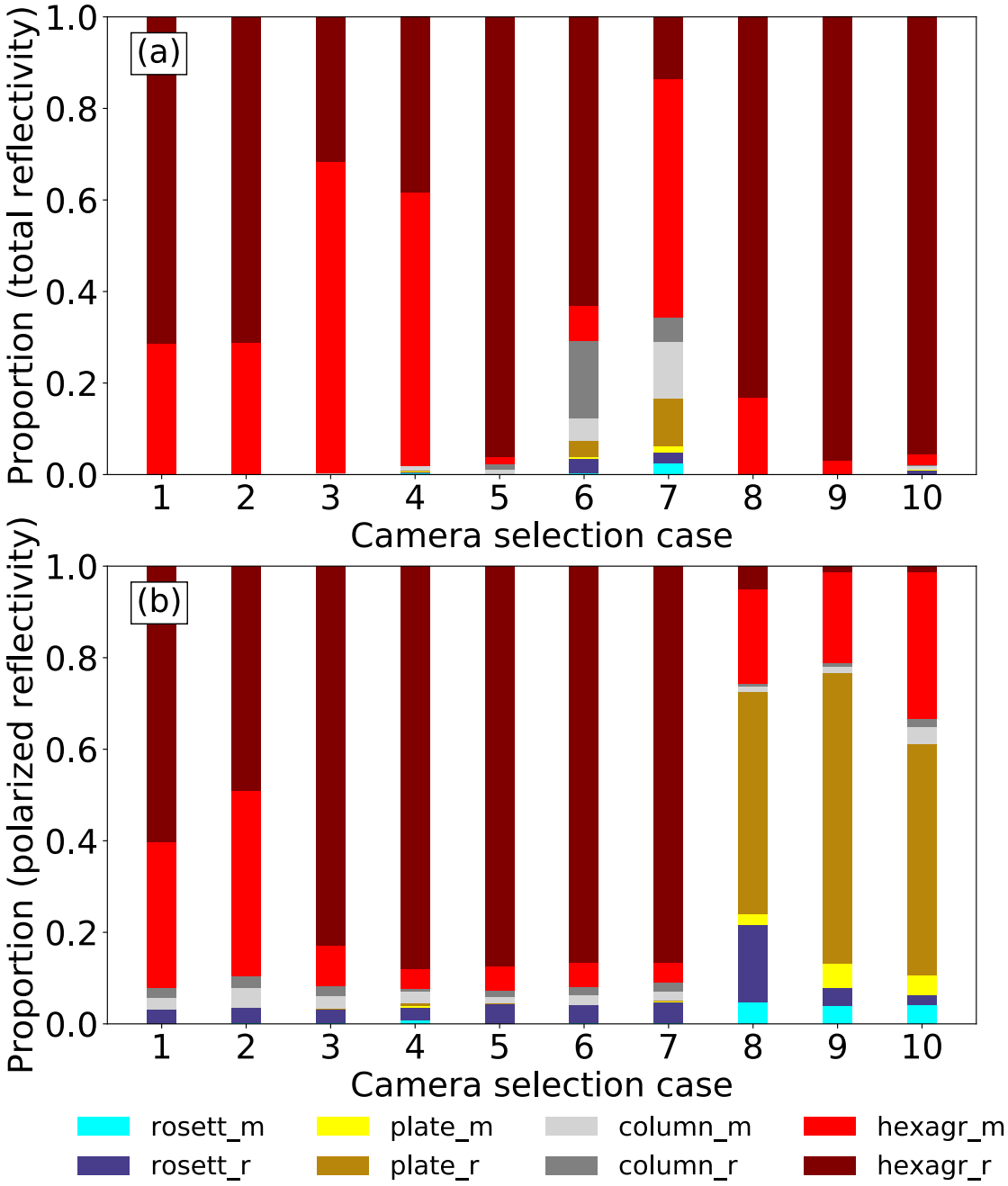

Figure 4.5 The proportion of inferred ice particle shapes in different camera selection cases using a) total reflectivity and b) polarized reflectivity.

When retrievals use total reflectivity (Figure 4.5a), the hexagonal column aggregate habit (either smooth or roughened particles) is chosen for the most pixels in all camera selection groups. The proportions of smooth particles in cases 3 and 4 are larger than in cases 1 and 2. These higher proportions mean that more pixels are being selected that have roughening when only smaller viewing zenith angles are selected. Comparison of the retrievals between forward camera cases (cases 5-7) and aft camera cases (cases 8-10) indicates that the optimal ice particle shapes are more diverse in forward camera cases (especially 6 and 7). From Case 5 to Case 7, as the nadir and 290F cameras are removed, the range of observed scattering angles also decreases, and the proportion of hexagonal aggregate habits decreases as well. Unlike the forward camera cases, the proportions of each ice model are quite stable among the three aft camera cases. While the number of cameras is different in each aft camera case, the range of scattering angles is similar in each case.

With the polarized reflectivity results in this case study shown in Figure 4.5b, the hexagonal aggregate habit is chosen more often for most camera selections (except the aft camera groups, 8 to 10). Unlike the retrievals using total reflectivity, in the first 4 groups more ice pixels are explained by the roughened hexagonal shape when the number of camera pairs is reduced. For forward camera cases (5, 6, and 7), the proportions of pixels explained by various ice models are almost identical in each group. The majority of pixel habit retrievals result in the roughened hexagonal shape in selection groups 3-7. The proportions of the optimal ice particle shape in aft camera cases (8 to 10) are significantly different than in the other 7 cases. In the aft camera cases, most pixels are identified as the

roughened plate, but the variation of the optimal ice particle habit is high in every case. This is because the measured polarized reflectivity is significantly smaller than the simulated polarized reflectivity when using forward cameras than when using the aft cameras or the nadir camera. Among those cameras, five models (smooth column, roughened column, smooth hexagonal, roughened hexagonal, and roughened bullet rosette shapes) provide similar low polarized reflectivities. For aft cameras, the simulated polarized reflectivities with smooth and roughened plate models are both close to measured polarized reflectivities. This feature causes the plate habit to explain most pixels in aft camera selection cases but not in other selection groups in this study case.

The hexagonal aggregate column habit explains most pixels in both total reflectivity and polarized reflectivity retrievals in this study case, as shown in Figure 4.5. This is consistent with a previous study (Cole et al., 2014) that was applied to ice clouds with optical thickness larger than 5. Note that the roughened hexagonal aggregate model is also the ice model used in MODIS Collection 6. That implies the polarization properties of the MODIS Collection 6 model are consistent with the case in AirMSPI measurements.

The inconsistency (s^2) between the simulated and measured reflectivity in each camera selection case is shown in Figure 4.6. The inconsistency in Figure 6a is defined as the standard deviation of retrieved optical thickness among selected cameras. The inconsistency is computed by Equations (4.3) and (4.4) for total reflectivity and polarized reflectivity, respectively. In Figure 4.6a, the inconsistency is smaller with fewer pairs of cameras (compare cases 2 to 4), and aft camera cases (8 to 10) have larger inconsistency than forward camera cases (5 to 7). The retrieved optical thickness values among forward

cameras are low, but much higher using aft cameras. Thus, the large inconsistency in Figure 4.6a is likely caused by retrieved high optical thickness values in aft cameras. The inconsistency in Figure 4.6b using polarized reflectivity is also sensitive to the camera selection as Figure 4.6a using total reflectivity. However, the differences in the polarized reflectivity have larger inconsistencies when forward cameras are involved.

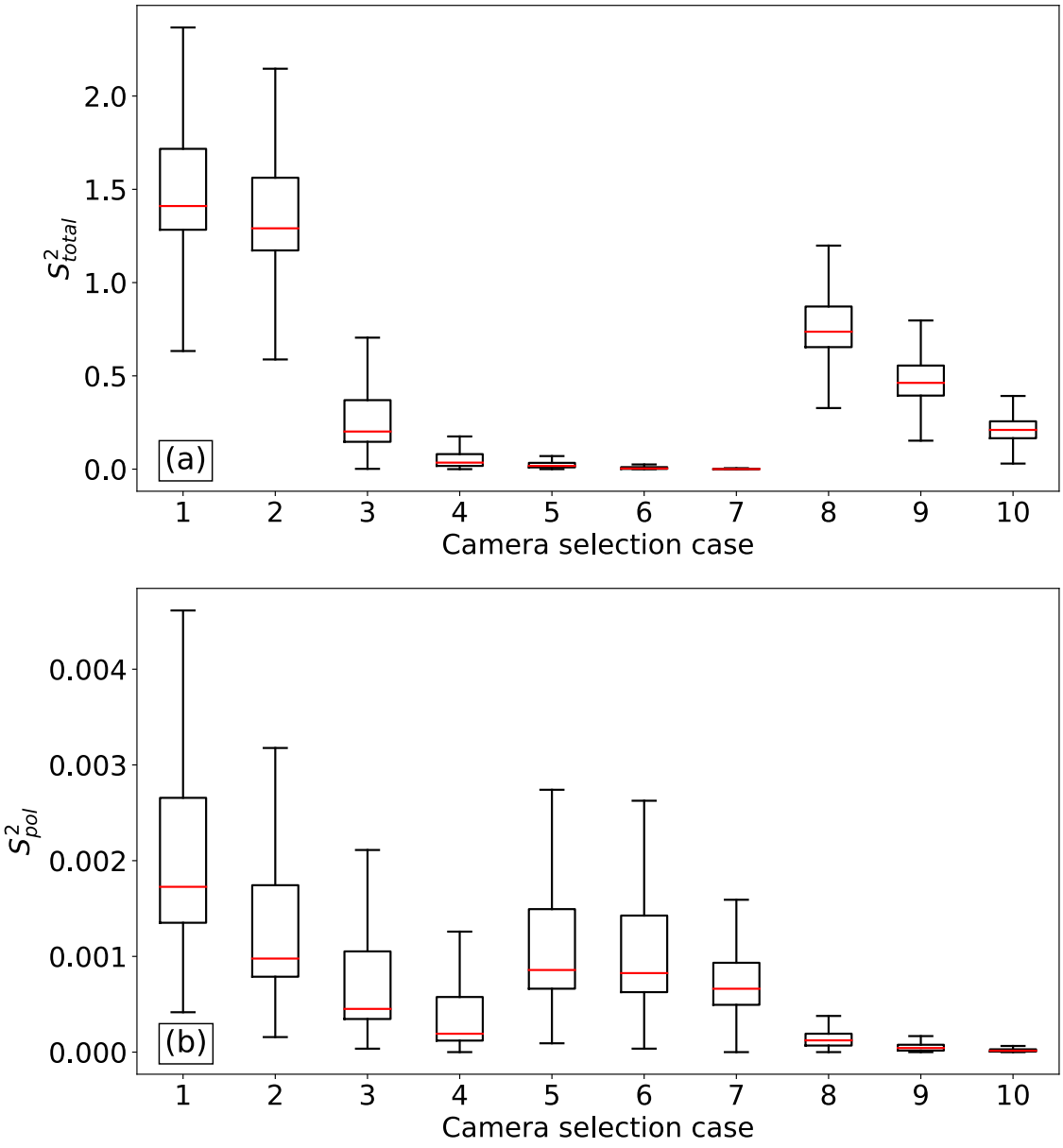

Figure 4.6 The inconsistency between model reflectivity with inferred ice particle models and measurement from a) total reflectivity and b) polarized reflectivity, for each different camera selection case.

The inconsistency in both total reflectivity and polarized reflectivity is reduced with fewer camera pairs with smaller viewing zenith angles (nearer to nadir). This means that the larger zenith angle camera measurements introduce larger inconsistency. A comparison of the forward and aft camera cases indicates that the inconsistency of forward camera cases is significantly lower than for aft camera cases in polarized reflectivity, but inconsistency is higher in total reflectivity. Note that the diversity of the optimal ice models is higher with forward camera cases in Figure 4.6a, but higher with aft camera cases in Figure 4.6b. This indicates that the variation of the optimal ice models increases when there is an inconsistency between simulations and measurements.

4.4. Summary and Conclusions

In this study, we developed a remote sensing technique to infer the optimal ice particle models using polarimetric observations of cirrus clouds. Briefly, during ice particle model inference, the optical thickness retrieved from total reflectivity is assumed in computing polarized reflectivity. This improvement in retrieval system provides better consistency to measurement of cirrus clouds, since typical optical thickness of cirrus clouds is less than 5. In doing so, we avoid the common treatment that the ice cloud optical thickness is assumed to be larger than 5 in inferring ice particle shape model for cirrus clouds. We applied this method to Airborne Multi-angle SpectroPolarimeter Imager (AirMSPI) measurements to infer optimal ice particle models for cirrus clouds. In addition, the influence of different camera selections on the resulting optimal ice particle model from total reflectivity and polarized reflectivity is assessed.

The hexagonal aggregate column habit (with either smooth or roughened particles) explains most pixels in both total reflectivity and polarized reflectivity retrievals in this study case. The optimal ice model in different camera selection groups shows that zenith angle dependence (cameras viewing closer to or farther from nadir) has less effect on ice particle shape retrievals than selecting forward or aft viewing cameras. The inferred ice particle habit does not change much as the number of selected cameras increases, but a smooth particle model works for more pixels in total reflectivity retrievals and a roughened particle model works better for polarized reflectivity retrievals. However, when reducing the number of selected camera pairs, or with fewer camera pairs, the inconsistency is significantly decreased. The smallest inconsistency exists using forward cameras in the total reflectivity retrievals or using aft cameras in the polarized reflectivity retrievals. Furthermore, the cases having the smallest inconsistencies also have the largest diversity of the optimal inferred ice model. These findings point to the fact that a large inconsistency of polarization properties exists between simulated and measured ice cloud reflectivities.

As an airborne instrument, AirMSPI provides higher resolution data than satellite sensors for the multi-angle imaging measurements. It is still useful to infer optimal ice particle models for cirrus clouds using such fine resolution polarized measurements. However, since the AirMSPI project is not mainly focused on ice clouds, the observations that contain cirrus clouds are really rare. Therefore, future research should apply this technique to large volume datasets, like POLDER, to further evaluate the effect of camera selection on retrievals.

5. THE RETRIEVALS OF ICE CLOUD OPTICAL THICKNESS USING MULTI-ANGULAR AND MULTI-SPECTRAL TECHNIQUES

5.1. Introduction

Measurements from multiple channels are often used to infer the ice particle shape in remote sensing. This chapter focuses on using shortwave and thermal infrared (IR) bands to retrieve ice cloud properties. The shortwave bands have been extensively used as we mentioned in previous chapters. However, the differences of cloud property retrievals based on different ice crystal models are smaller in the IR bands than in shortwave bands, because ice crystal shape has a smaller impact on retrievals in the thermal IR spectral regime than in the shortwave regime. However, an optimal ice model should produce consistent shortwave and thermal IR cloud retrievals. Therefore, both shortwave and thermal IR bands should be used to test ice particle shape models to determine an optimal ice crystal model assumed for satellite retrievals.

In this chapter, data from MODIS (Moderate Resolution Imaging Spectroradiometer) is applied to retrieve optical thickness using both shortwave and thermal infrared bands. By comparing the difference between two retrieval methods (shortwave and thermal infrared bands), the optimal ice particle shape among selected models is determined. Two ice particle models are applied in this chapter to each retrieval method. One is the operational MODIS Collection 6 model, and the other is the Two Habit Model. In order to compare the results of the optimal ice particle shape used in previous chapters, the multi-angular retrieval algorithm is also applied to the same granule data but

using MISR (Multi-angle imaging spectroradiometer) measurements. Both MISR and MODIS are on board NASA's Terra spacecraft, which provides a good opportunity to investigate the retrieved ice cloud properties from an additional perspective.

5.2. Data and Methods

The multi-spectral retrievals in this study are based on both shortwave and thermal infrared bands. The core idea is to retrieve optical thickness from these two bands with different retrieval algorithms, and then evaluate the performance of ice particle models by checking the consistency of these two retrieved optical thicknesses from different algorithms.

5.2.1. Thermal infrared retrievals

This study performs thermal infrared retrievals by the split-window method, which retrieves optical thickness using brightness temperature measurements in thermal infrared channels at 11 and 12 μm (MODIS bands 31 and 32) are used here. The correlated-K method is applied in the forward model to account for gas absorption, and the DISORT model is applied to simulate radiance. The atmospheric profile and ocean surface temperature data are provided by the ERA-interim reanalysis dataset.

5.2.2. Multi-angle retrievals

The multi-angle retrievals are based on MISR-MODIS fused data (Liang and Girolamo, 2013; Liang et al., 2009). The MODIS and MISR satellite sensors are onboard NASA's Terra platform, with a local equator-crossing-time around 10:30 am. The MISR observed reflectance at 0.86 μm is selected here because this channel is least affected by ozone and ice absorption. The MISR sensor provides up to 9 reflectances for each pixel

with different viewing directions, each corresponding to a different scattering angle. MISR has 9 cameras at fixed angles, including one nadir camera (AN), four cameras (AF, BF, CF, DF) pointing forward along the orbital track, and four cameras (AA, BA, CA, DA) pointing aft. The Viewing Zenith Angles (VZAs) for the AA/AF, BA/BF, CA/CF, DA/DF cameras are 26.1°, 45.6°, 60.0°, and 75.0°, respectively, and the AN camera views at nadir (VZA = 0°). Because of these 9 cameras, the scattering angles of MISR data have a wider range than most satellite sensors with a nadir camera only.

The purpose of the multi-angle retrieval algorithm used in this study is to check the consistency of retrieved optical thickness from multi-angle measurements. A perfect ice particle model should produce the same value of optical thickness at all scattering angles. Considering computational stability, we replace the optical thickness by spherical albedo. The spherical albedo represents an integral value of the reflection function over all viewing and solar zenith and azimuth angles, and it has a non-linear one-to-one relation to optical thickness. This algorithm is fully detailed by Wang et al. In brief, following an algorithm by Doutriaux-Boucher et al. (2000), an adding doubling radiative transfer model (Huang et al., 2015) with several different ice particle models computes the spherical albedo corresponding to each MISR camera observed reflectance at 0.86 μm. The spherical albedo difference value is the spherical albedo at any angle minus the average spherical albedo in all available angles (a pixel may have fewer than nine suitable camera views). If the assumed model is correct, SAD values should be zero at all scattering angles. Therefore, the ice particle model generating the smallest total SAD departures over all cameras is the best-fit for that pixel.

5.2.3. Shortwave retrievals

The data used in the shortwave retrievals are from MODIS measurements onboard the Terra satellite. Two bands at 0.86 and 2.13 μm are selected to retrieve optical thickness and effective radius.

The retrievals of τ in shortwave bands are based on a bi-spectral shortwave technique (Nakajima and King, 1990) in conjunction with two MODIS bands centered at 0.86 and 2.13 μm. The theoretical foundation of this technique is that a conservative scattering channel (e.g., visible bands and the channel centered at 0.86 μm) contains information that is primarily dependent on optical thickness. However, the reflectivity in a weakly absorbing band (e.g., 2.13 μm) depends on both optical thickness and effective radius, especially with a small optical thickness. As optical thickness increases, the reflectivity is mostly a function of effective radius.

The look-up table strategy is applied in this study to retrieve both optical thickness and effective radius. Briefly, for each wavelength band, the reflection functions are first calculated using a rigorous radiative transfer model, for a large range of values of optical thickness and effective radius. Then, the reflection functions for each wavelength band are stored in a look-up table at closely spaced intervals of three geometrical angles (solar zenith angle, view zenith angle, and relative azimuthal angle). The determinations of optical thickness and effective radius are obtained from MODIS measurements of reflectance at 0.86 and 2.13 μm by entering the measured reflectances into the look-up table with the corresponding three geometrical angles, and searching for the best-fitting combination of optical thickness and effective radius.

5.2.4. Data selection

We use the MODIS cloud products to filter and stratify ice cloud pixels in this study. To avoid cloud pixels containing liquid particles, pixels are selected by applying the following criteria: (1) MODIS infrared cloud phase is ice; (2) cloud top pressure is less than 900 hPa; and (3) cloud top temperature is less than 233K. To avoid any effect of variable land reflectance, and to reduce the complexity of radiative transfer computations, only observations over ocean are used. Effects of sunglint are avoided by removing each MISR camera measurement with sunglint angle less than 35°. Suspected multilayer clouds are removed by identifying pixels with MISR stereo height values and MODIS cloud top height values differing by more than 2000m. The theory and algorithm details can be found in McFarlane and Marchand (2008) and Naud et al. (2002). All pixels in this study are overcast.

This study performs a case study of the different retrievals using collocated MISR-MODIS fused data over tropical oceans at September 02, 2013. The atmospheric profiles are downloaded from the European Centre for Medium-Range Weather Forecasts (ECMWF) Interim Re-Analysis (ERA-Interim) (Dee et al. 2011) with a spatial resolution of 0.5 degree times 0.5 degree and time resolution is 6 hours.

5.2.5. Ice model

Two widely-used ice particle models were selected in this study. One is the ice particle model in the MODIS Collection 6 operational products. The MODIS Collection 6 ice particle model (MC6) uses a roughened hexagonal ice aggregate habit with ice particle surface roughness of 0.5. The surface roughness in this study, briefly, is a

parameter used to adjust single scattering properties of ice particles in the light scattering calculation, and is defined as the standard deviation of a random 2-D Gaussian surface tilting distribution of small "facets" on the surface of ice particles (Yang and Liou, 1998).

The other ice particle model is called the Two-Habit Model (THM) from the Cloud and the Earth's Radiant Energy System (CERES) Edition 5 (Loeb et al., 2018). The THM is a mixture of 2 different habits, with the proportions of the habits depending on the cloud top temperature and the average particle size. One habit is an ensemble average of 20 distorted hexagonal column aggregates and the other habit is the roughened hexagonal column.

Both of these ice particle models are applied in all retrieval algorithms (shortwave retrievals, infrared band retrievals, and multi-angle retrievals) to compare the ice particle models in both multispectral and multi-angular approaches.

5.3. Results and discussions

Figure 5.1 compares the retrieved optical thicknesses using shortwave and thermal IR methods in conjunction with MC6 and THM models. From the comparison, the retrieved optical thickness from two different methods in conjunction with these two ice particle models are generally spectrally consistent, in agreement with Yang et al. (2018). The optical thicknesses retrieved with the split window technique in the thermal IR band are systematically higher than the solar band counterparts for both ice particle models, especially when the optical thickness is larger, likely because the thermal infrared channel is not sensitive to the lower portion of thick clouds (Saito et al., 2017; Yang et al., 2018).

This slight difference leads the MC6 to display a slightly worse spectral consistency than THM.

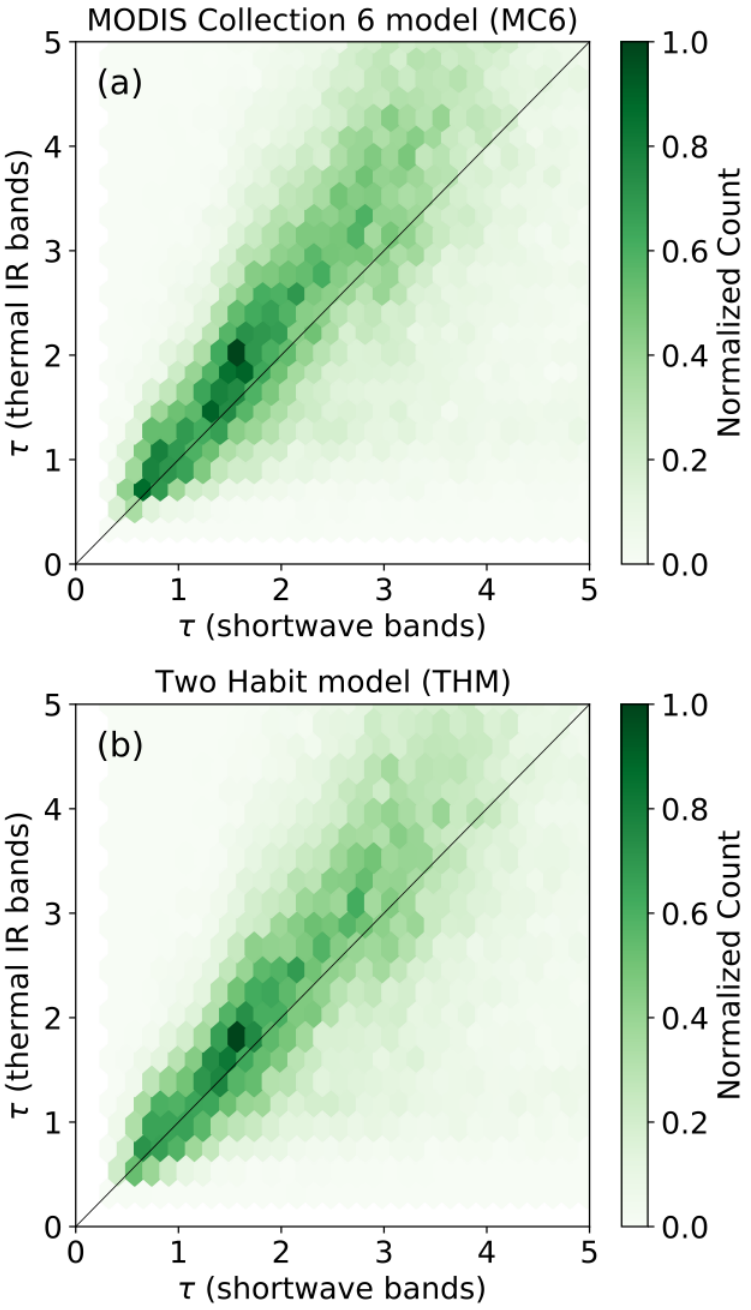

Figure 5.1 Comparison of the retrieved optical thickness from applying the split window method in shortwave and thermal IR bands, assuming each ice particle model, (a) MC6 model, (b) Two Habit Model.

To better understand the effect of different scattering geometries on retrieved optical thickness, Fig 5.2 shows the deviation of spherical albedo values (spherical albedo difference) with assuming MC6 and THM, based on the same cases used in Fig 5.1. Each spherical albedo value is computed from a single satellite camera under a specific scattering angle, and each spherical albedo difference is the difference from the average spherical albedo based on up to 9 cameras viewing that pixel. Due to the satellite orbit, all accepted camera views in this example have scattering angles (in 5° bins) from 65 to 170°. The spherical albedo differences in both of these figures have negative values in the backward scattering directions (i.e., scattering angle larger than 150°), meaning that the values of computed phase functions for these ice particle models are probably too small for scattering angles larger than 150°. Under forward scattering directions, the values of spherical albedo difference are positive for both ice particle models, but positive values for MC6 are lower than for THM. The relatively lower positive values for MC6 indicate that assuming the MC6 ice particle model instead of THM is likely to produce spherical albedo retrievals having better consistency with MISR multi-angular measurements.

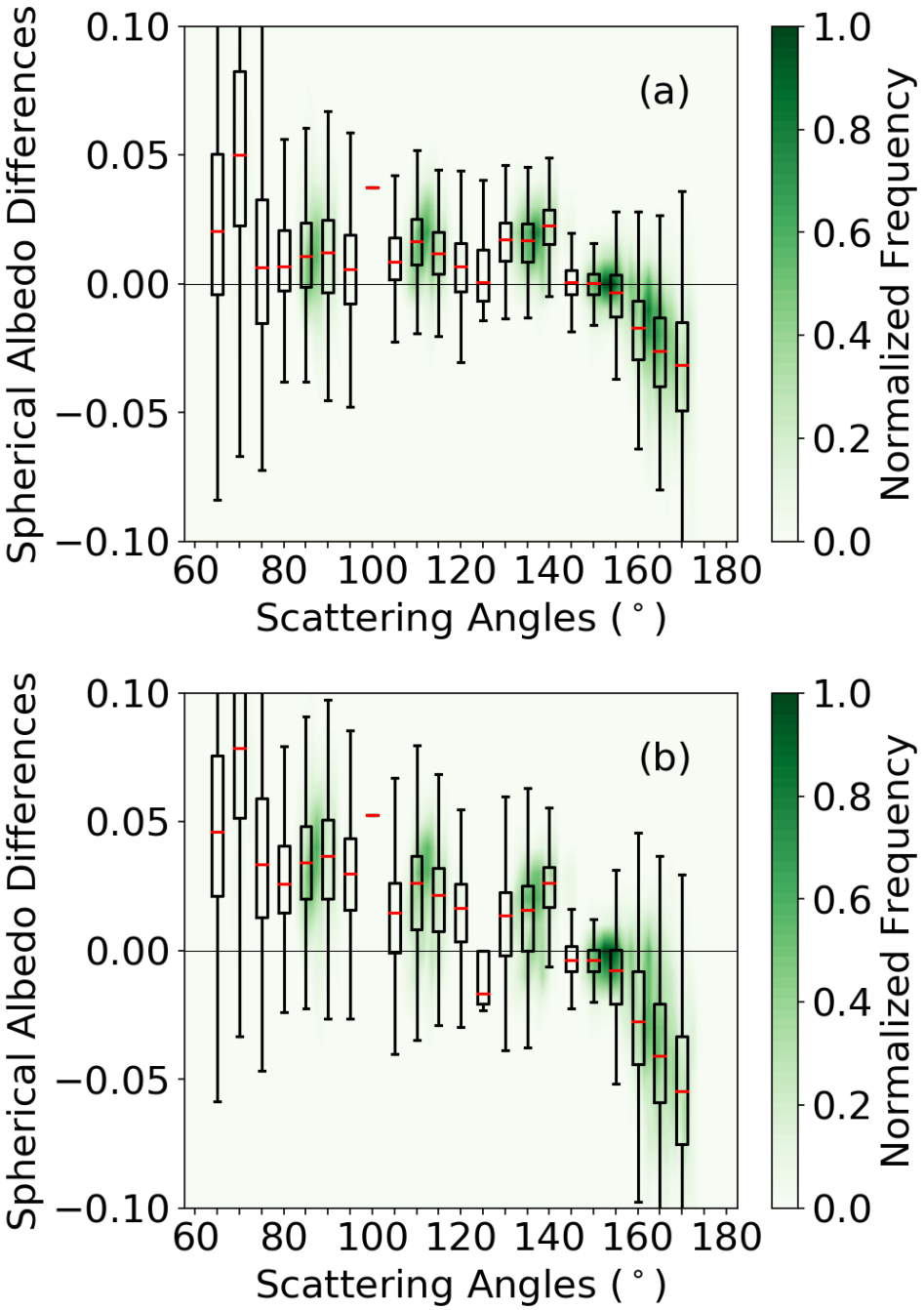

Figure 5.2 The deviation of spherical albedo values from the average over all scattering angles (spherical albedo difference) with assuming ice particle model (a) MC6 and (b) THM.

Figure 5.3 shows the proportions of pixels where the MC6 and THM ice particle models produce the “best” fit in these multi-spectral and multi-angular optical thickness retrievals. Whether the multi-spectral or multi-angular retrieval method is used, MC6 produces the best-fitting optical thickness retrievals for about 70% of the pixels, which is consistent with the results in Fig 5.1 and Fig 5.2.

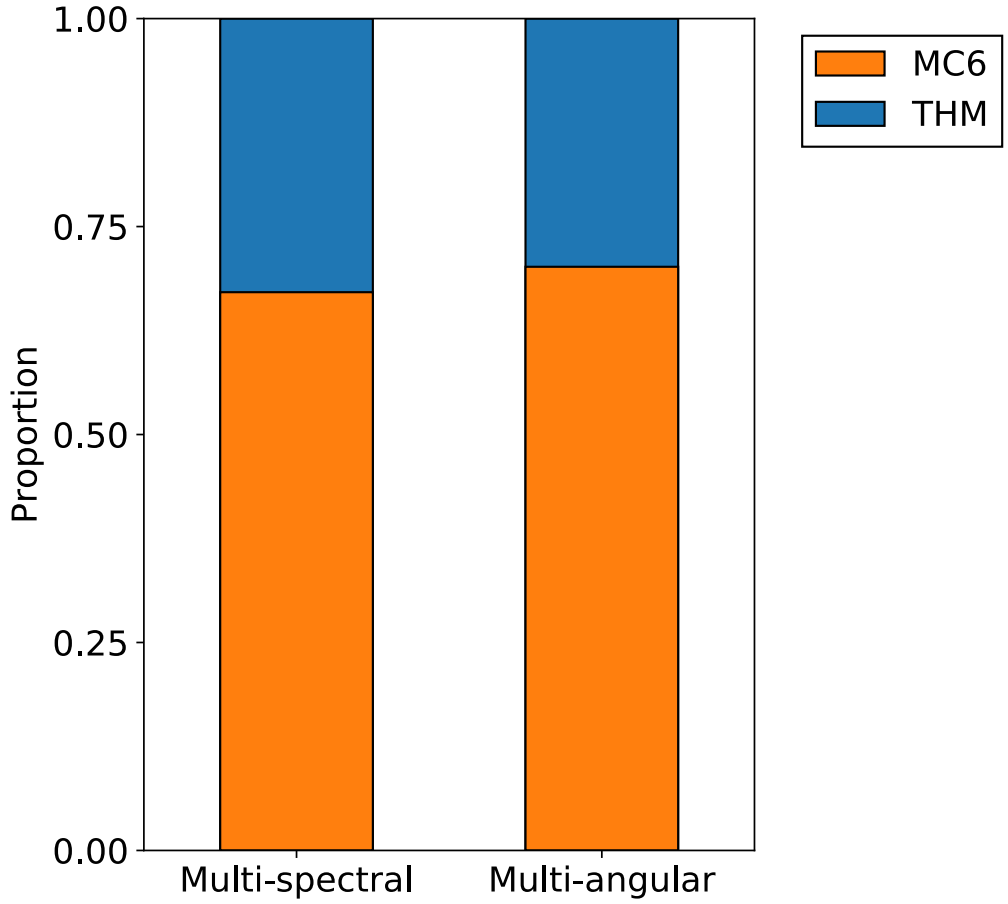

Figure 5.3 The proportions of pixels where the MC6 and THM ice particle models produce the best fitting optical thickness retrievals with both multi-spectral and multi-angular retrieval methods.

Figure 5.4 shows histograms of the best-fit ice particle model (MC6 or THM) for each pixel in two different cloud regimes when either the multi-spectral or multi-angular retrieval methods is used. In Fig 5.4a, with a multi-spectral retrieval, THM is most likely to produce the best optical thickness retrieval with a thin ice cloud and MC6 is likely to be the best with a thicker cloud. In Fig 5.4b, with a multi-angular retrieval, THM produces the best retrievals with optical thickness ~1 to 2, but MC6 is slightly favored with lower or higher optical thickness. In Fig 5.4c-d, with either retrieval method, there is no clear advantage for which ice particle model produces the best fit as the ice cloud top height varies.

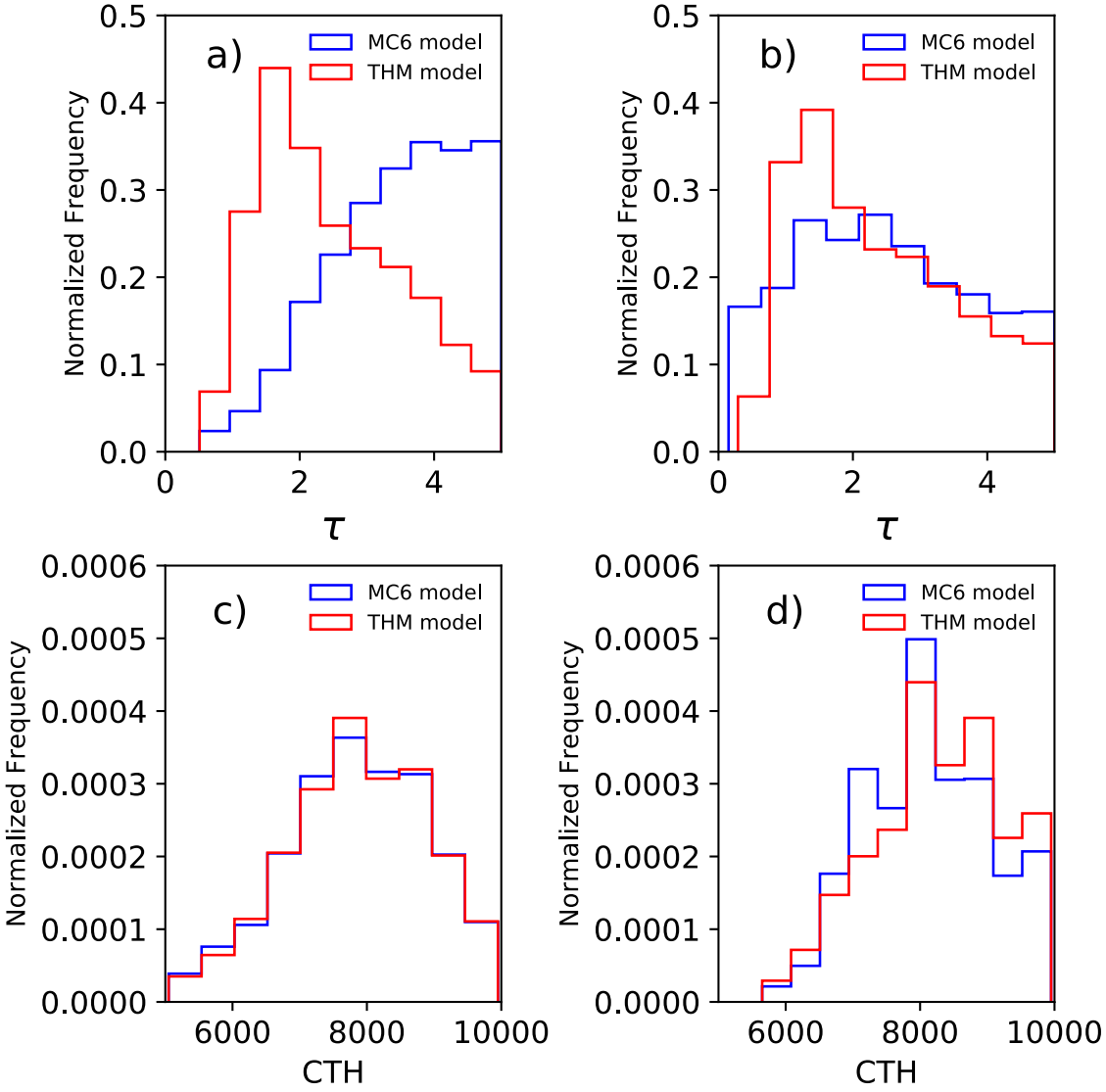

Figure 5.4 The histogram of cloud optical thickness for different cloud regimes (top row: optical thickness from 0 to 5, and bottom row: cloud top from 5000 to 10000 m) from (left panels) multi-spectral and (right panels) multi-angular retrieval methods.

The study case in this chapter provides a good opportunity to better understand the cloud properties using multi-angular and multi-channel retrieval methods. It is noted that cloud property varies depending on time and location. The results are limited in this study case area.

Current satellite measurements emphasize the phase function for scattering angles larger than 50 degrees, a limitation caused by the current satellite instrument characteristics. With the rapid development of drone techniques, more precisely the Unmanned aerial systems (UAS), a scattering angle of less than 50 degrees might be observed by remote sensing techniques in the future by mounting the sensor on the top of the UAS and sampling under the ice cloud layers. Furthermore, advanced computer vision techniques also can provide a new capability to detect cloud characteristics, such as the shape of the cloud layer, which may be useful in the computation of the 3D effect.

6. CONCLUSIONS

Remote sensing is widely used for investigating ice cloud properties and downstream applications such as climate effects and hydrology resource estimations. Most retrieval algorithms for remote sensing of ice clouds are based on the radiative properties of ice clouds and therefore the algorithm is commonly highly dependent on the assumed ice particle model. Since applying a different ice particle model will lead to different retrievals, selecting the appropriate ice particle model is of vital importance in remote sensing of ice clouds.

With light scattering calculation improvements in recent years, ice particle models with complex shapes and fine textures, such as degree of roughness, are available. Therefore, the different ice particle models need to be validated to investigate which model of these ice particle models best represents reality.

Chapter 2 investigated the optimal degree of ice particle roughness and its latitudinal variations. Compared to previous studies using cross-track scanning sensor data, this section improved an algorithm to process multi-angular satellite sensor measurements. The optimal degree of roughness shows a latitudinal dependence related to the solar zenith angle. In cloudy scenarios indexed by cloud heterogeneity, the optimal model for thick homogeneous clouds corresponds to more roughened ice particles in the tropics than in the extra-tropics. These results demonstrate that the consistency between multi-angular sensor measurements and an assumed single ice particle model varies on a

global scale. This inconsistency potentially leads to ice particle retrievals which could differ from geospatial distributions of particle shapes in reality.

Chapter 3 assessed the differences in retrievals of different ice particle models by building and applying a dynamic ice particle model on the pixel level. This dynamic model always selects the optimal degree of roughness that best fits the multi-angular sensor measurements. The retrievals based on a full year of global satellite observations indicate that the dynamic ice particle model produces a larger median optical thickness by 10.1% and smaller median effective radius by 6.5% compared to the operational MODIS Collection 6 product. Both the larger optical thickness and smaller effective radius increase the brightness in albedo retrievals. The brighter albedo is likely caused by the cloud 3D effect. Specifically, the multi-angular sensor measurements could better capture the horizontal scattering of radiation from cloud sides with a nearly vertical sun than the cross-track scanning sensor.

Chapter 4 developed a retrieval algorithm to validate the optimal ice particle model using a prototype multi-angular sensor with polarimetric measurement, the NASA next generation satellite Multi-Angle Imager for Aerosols (MAIA). This algorithm is tested using data from a prototype sensor installed on a research aircraft. The results show the camera selections for retrievals need to be paid attention to when the multi-angular camera measurements include polarized radiances. Chapter 5 compares the optimal ice particle model identified by using both multi-angular techniques and multi-channel techniques.

This doctoral research project contributes to better understanding of ice particle models used in the remote sensing of ice clouds, and develops an improved ice particle

model, compared to the current operational satellite products that use a single ice particle model.

REFERENCES

Bailey, M., and J. Hallett (2004), Growth rates and habits of ice crystals between -20° and -70°C, J. Atmos. Sci., 61(5), 514–544.

Bailey, M., and J. Hallett (2009), A comprehensive habit diagram for atmospheric ice crystals: Confirmation from the laboratory, AIRS II, and other field studies, J. Atmos. Sci., 66(9), 2888–2899.

Baran, A. J. (2009), A review of the light scattering properties of cirrus, J. Quant. Spectrosc. Radiat. Transfer., 110(14-16), 1239–1260.

Baran, A. J. P. N. Francis, L. C.-Labonnote, M. A. Doutriaux-Boucher (2001), scattering phase function for ice cloud: Tests of applicability using aircraft and satellite multi-angle multi-wavelength radiance measurements of cirrus. Quart. J. Roy. Meteor. Soc., 127, 2395–2416.

Baran, A. J., L. C.-Labonnote (2006), On the reflection and polarisation properties of ice cloud. J. Quant. Spectrosc. Radiat. Transf., 100, 41–54.

Baran, Anthony J. (2009), A review of the light scattering properties of cirrus, J. Quant. Spectrosc. Radiat. Transfer., 110.14-16, 1239-1260.

Baran, Anthony J., and L-C. Labonnote, (2007), A self-consistent scattering model for cirrus. I: The solar region, Quart. J. Roy. Meteor. Soc., 133.629: 1899-1912.

Baum, B. A., A. J. Heymsfield, P. Yang, and S. T. Bedka, (2005), Bulk scattering properties for the remote sensing of ice clouds. Part I: Microphysical data and models, J. Appl. Meteor., 44(12), 1885–1895.

C.-Labonnote, L., G. Brogniez, M. Doutriaux-Boucher, J. C. Buriez, J. F. Gayet, H. Chepfer (2000), Modeling of light scattering in cirrus clouds with inhomogeneous hexagonal monocrystals. Comparison with in-situ and ADEOS-POLDER measurements. Geophys. Res. Lett., 27, 113–116.

C.-Labonnote, L., G. Brogniez, J. C. Buriez, M. Doutriaux-Boucher, J. F. Gayet, A. Macke (2001), Polarized light scattering by inhomogeneous hexagonal monocrystals: Validation with ADEOS-POLDER measurements. J. Geophys. Res., 106, 12139–12153.

Chen, T., W. B. Rossow, and Y. Zhang (2000), Radiative effects of cloud-type variations. J. Climate, 13(1), 264–286.

Chepfer, H., P. Goloub, J. Riédi, J. F. De Haan, J. W. Hovenier, P. H. Flamant (2001), Ice crystal shapes in cirrus clouds derived from POLDER/ADEOS-1. J. Geophys. Res., 106, 7955–7966.

Cole, B.H., P. Yang, B. A. Baum, J. Riedi, L. C.-Labonnote, (2014), Ice particle habit and surface roughness derived from PARASOL polarization measurements. Atmos. Chem. Phys., 14, 3739–3750.

Cox, C., W. Munk (1954), Measurement of the roughness of the sea surface from photographs of the suns glitter. J. Opt. Soc. Am. 1954, 44, 838–850.

Cox, Charles, and Walter Munk (1954), Measurement of the roughness of the sea surface from photographs of the sun’s glitter. Josa 44.11: 838-850.

Dee, D., and Coauthors (2011), The ERA-Interim reanalysis: Configuration and performance of the data assimilation system. Quart. J. Roy. Meteor. Soc., 137, 553–597.

Di Girolamo, L., L. Liang, and S. Platnick (2010), A global view of one-dimensional solar radiative transfer through oceanic water clouds, Geophys. Res. Lett., 37, L18809, doi:10.1029/2010GL44094.

Diner, D.J., Xu, F., Garay, M.J., Martonchik, J.V., Rheingans, B.E., Geier, S., Davis, A., Hancock, B.R., Jovanovic, V.M., Bull, M.A. and Capraro, K. (2013), The Airborne Multiangle SpectroPolarimetric Imager (AirMSPI): a new tool for aerosol and cloud remote sensing. Atmos. Meas. Tech., 6.8 2007-2025.

Diner, D. J., J. C. Beckert, G. W. Bothwell, and J. I. Rodriguez (2002), Performance of the MISR instrument during its first 20 months in Earth orbit, IEEE Trans. Geosci. Remote Sens., 40(7), 1449–1466.

Diner, D. J., J. C. Beckert, T. H. Reilly, C. J. Bruegge, J. E. Conel, R. A. Kahn, J. V. Martonchik, T. P. Ackerman, R. Davies, S. A. Gerstl, and H. R. Gordon (1998), Multi-angle Imaging SpectroRadiometer (MISR) instrument description and experiment overview, IEEE Trans. Geosci. Remote Sens., 36(4), 1072–1087.

Diner, D.J.; J. C. Beckert, G. W. Bothwell, J. I. Rodriguez (2002), Performance of the MISR instrument during its first 20 months in earth orbit. IEEE Trans. Geosci. Remote Sens., 40, 1449–1466.

Doutriaux-Boucher, M., J. C. Buriez, G. Brogniez, L. C-Labonnote, and A. J. Baran (2000), Sensitivity of retrieved POLDER directional cloud optical thickness to various ice particle models, Geophys. Res. Lett., 27(1), 109–112.

Doutriaux‐Boucher, M., Buriez, J.C., Brogniez, G., C.‐Labonnote, L. and Baran, A.J. (2000), Sensitivity of retrieved POLDER directional cloud optical thickness to various ice particle models, Geophys. Res. Lett., 27.1: 109-112.

Geogdzhayev, I.V., B. van Diedenhoven (2016), The effect of roughness model on scattering properties of ice crystals. J. Quant. Spectrosc. Radiat. Transf., 178, 134–141, doi:10.1016/j.jqsrt.2016.03.001.

Grosvenor, D.P.; R. Wood (2014), The effect of solar zenith angle on MODIS cloud optical and microphysical retrievals within marine liquid water clouds. Atmos. Chem. Phys., 14, 7291–7321.

Hansen, J., and L. Travis (1974), Light scattering in planetary atmospheres, Space Sci. Rev., 16, 527–610.

Heymsfield, A. J., C. Schmitt, A. Bansemer, and C. H. Twohy (2010), Improved representation of ice particle masses based on observations in natural clouds, J. Atmos. Sci., 67(10), 3303–3318.

Heymsfield, A. J., C. Schmitt, and A. Bansemer (2013), Ice cloud particle size distributions and pressure-dependent terminal velocities from in situ observations at temperatures from 0° to -86°C, J. Atmos. Sci., 70(12), 4123-4154.

Hioki, S., P. Yang, B. A. Baum, S. Platnick, K. G. Meyer, M. D. King, and J. Riedi (2016), Degree of ice particle surface roughness inferred from polarimetric observations, Atmos. Chem. Phys., 16(12), 7545–7558.

Hioki, S. (2018). Characterizing ice cloud particle shape and surface roughness from polarimetric satellite observations (Doctoral dissertation).

Holz, R.E., S. Platnick, K. Meyer, M. Vaughan, A. Heidinger, P. Yang, G. Wind, S. Dutcher, S. Ackerman, N. Amarasinghe, and F. Nagle (2016), Resolving ice cloud optical thickness biases between CALIOP and MODIS using infrared retrievals. Atmos. Chem. Phys., 16, 5075–5090.

Horváth, Á., and R. Davies (2007), Comparison of microwave and optical cloud water path estimates from TMI, MODIS, and MISR, J. Geophys. Res., 112, D01202, doi:10.1029/2006JD007101.

Huang, X., P. Yang, G. Kattawar, and K. N. Liou (2015), Effect of mineral dust aerosol aspect ratio on polarized reflectance, J. Quant. Spectrosc. Radiat. Trans., 151, 97–109.

King, M. D. (1987), Determination of the scaled optical thickness of clouds from reflected solar radiation measurements, J. Atmos. Sci., 44(13), 1734-1751.

King, M. D., S. Platnick, W. P. Menzel, S. A. Ackerman, and P. A. Hubanks (2013), Spatial and temporal distribution of clouds observed by MODIS onboard the Terra and Aqua satellites, IEEE Trans. Geosci. Remote Sens., 51(7), 3826–3852.

King, M.D. (1987), Determination of the scaled optical thickness of clouds from reflected solar radiation measurements. J. Atmos. Sci., 44, 1734–1751.

Letu, H., H. Ishimoto, J. Riedi, T. Y. Nakajima, L. C-Labonnote, A. J. Baran, T. M. Nagao, and M. Sekiguchi (2016), Investigation of ice particle habits to be used for ice cloud remote sensing for the GCOM-C satellite mission, Atmos. Chem. Phys., 16(18), 12287–12303.

Letu. H, T. M. Nagao, T. Y. Nakajima J. Riedi, H. Ishimoto, A. J. Baran, H. Shang, M. Sekiguchi, and M. Kikuchi (2019), Ice cloud properties from Himawari-8/AHI next-generation geostationary satellite: Capability of the AHI to monitor the DC cloud generation process, IEEE Trans. Geosci. Remote Sens., 57 (6), 3229–3239.

Liang, L., L. Di Girolamo, and S. Platnick (2009), View-angle consistency in reflectance, optical thickness and spherical albedo of marine water-clouds over the northeastern Pacific through MISR-MODIS fusion, Geophys. Res. Lett., 36(9), L09811, doi:10.1029/2008GL037124.

Liang, Lusheng, and Larry Di Girolamo (2013) A global analysis on the view-angle dependence of plane-parallel oceanic liquid water cloud optical thickness using data synergy from MISR and MODIS. J. Geophys. Res., 118.5: 2389-2403.

Liou, K. N. (1986), Influence of cirrus clouds on weather and climate processes: A global perspective, Mon. We. Rev., 114(6), 1167–1199.

Liou, K. N., and P. Yang (2016), Light Scattering by Ice Crystals: Fundamentals and Applications, Cambridge University Press, 460 pp.

Loeb, N. G., P. Yang, F. G. Rose, G. Hong, S. Sun-Mack, P. Minnis, S. Kato, S. H. Ham, W. L. Smith, Jr., S. Hioki, and G. Tang (2018), Impact of ice cloud

microphysics on satellite cloud retrievals and broadband flux radiative transfer model calculations, J. Clim., 31(5), 1851–1864.

Loeb, N.G., R. Davies, (1997), Angular dependence of observed reflectances: A comparison with plane parallel theory. J. Geophys. Res., 102, 6865–6881.

Macke, A., J. Mueller, E. Raschke (1996), Single scattering properties of atmospheric ice crystals. J. Atmos. Sci., 53, 2813–2825.

Masuda, Kazuhiko, and Tsutomu Takashima (1992), Feasibility study of derivation of cirrus information using polarimetric measurements from satellite. Remote Sens. Environ., 39.1: 45-59.

McFarlane, Sally A., and Roger T. Marchand. (2008), Analysis of ice crystal habits derived from MISR and MODIS observations over the ARM Southern Great Plains site. J. Geophys. Res., 113.D7 (2008), 113, D07209, doi:10.1029/2007JD009191.

McFarlane, Sally A., Roger T. Marchand, and Thomas P. Ackerman (2005), Retrieval of cloud phase and crystal habit from Multiangle Imaging Spectroradiometer (MISR) and Moderate Resolution Imaging Spectroradiometer (MODIS) data. J. Geophys. Res., 110.D14, 110, D14201, doi:10.1029/2004JD004831.

McFarquhar, G.M., A.J. Heymsfield, (1996), Microphysical characteristics of three anvils sampled during the central equatorial Pacific experiment. J. Atmos. Sci., 53, 2401–2423.

Miller, D. J., Z. Zhang, S. Platnick, A. S. Ackerman, F. Werner, C. Cornet, and K. Knobelspiesse (2018), Comparisons of bi-spectral and polarimetric retrievals of

marine boundary layer cloud microphysics: case studies using a LES–satellite retrieval simulator, Atmos. Meas. Tech., 11, 3689–3715.

Mishchenko, M. I., and A. Macke (1999), How big should hexagonal ice crystals be to produce halos? Appl. Opt., 38(9), 1626–1629.

Mishchenko, M. I., W. B. Rossow, A. Macke, and A. A. Lacis (1996), Sensitivity of cirrus cloud albedo, bidirectional reflectance and optical thickness retrieval accuracy to ice particle shape, J. Geophys. Res., 101(D12), 16973–16985.

Mueller, K. J., D. L. Wu, A. Horvath, V. M. Jovanovic, J. P. Muller, L. Di Girolamo, M. J. Garay, D. J. Diner, C. M. Moroney, and S. Wanzong (2017), Assessment of MISR cloud motion vectors (CMVs) relative to GOES and MODIS atmospheric motion vectors (AMVs), J. Appl. Meteor. Climatol., 56, 555–572.

Muller, J.-P., A. Mandanayake, C. Moroney, R. Davies, D. Diner, and S. Paradise (2002), MISR stereoscopic image matchers: Techniques and results, IEEE Trans. Geosci. Remote Sens., 40, 1547–1559.

Nakajima, T., and M. D. King (1990), Determination of the optical thickness and effective particle radius of clouds from reflected solar radiation measurements. Part I: Theory, J. Atmos. Sci., 47(15), 1878–1893.

Naud, C., J. P. Muller, and E. E. Clothiaux (2002), Comparison of cloud top heights derived from MISR stereo and MODIS CO2-slicing, Geophys. Res. Lett., 29(16), doi:10.1029/2002GL015460.

Neshyba, S.P., B. Lowen, M. Benning, A. Lawson, P.M. Rowe (2013), Roughness metrics of prismatic facets of ice. J. Geophys. Res., 118, 3309–3318. http://dx.doi.org/10.1002/jgrd.50357.

Pfalzgraff, W. C., R. M. Hulscher, and S. P. Neshyba (2010), Scanning electron microscopy and molecular dynamics of surfaces of growing and ablating hexagonal ice crystals, Atmo. Chem. Phys., 10(6), 2927–2935.

Platnick, S., and L. Oreopoulos (2008), Radiative susceptibility of cloudy atmospheres to droplet number perturbations: 1. Theoretical analysis and examples from MODIS, J. Geophys. Res., 113, D14S20, doi:10.1029/2007JD009654.

Platnick, S., K. G. Meyer, M. D. King, G. Wind, N. Amarasinghe, B. Marchant, G. T. Arnold, Z. Zhang, P. A. Hubanks, R. E. Holz, and P. Yang (2017), The MODIS cloud optical and microphysical products: Collection 6 updates and examples from Terra and Aqua, IEEE Trans. Geosci. Remote Sens., 55(1), 502–525.

Platnick, S., K. G. Meyer, M. D. King, G. Wind, N. Amarasinghe, B. Marchant, G. T. Arnold, Z. B. Zhang, P. A. Hubanks, B. Ridgway, and J. Riedi (2018), MODIS cloud optical properties: User guide for the collection 6/6.1 level-2 MOD06/MYD06 product and associated level-3 datasets—Version 1.1, 146 pp, NASA Goddard Space Flight Center, Greenbelt, Md. [Available at http:// modis-atmosphere.gsfc.nasa.gov/sites/default/files/ModAtmo/MODISCloudOpticalPropertyUserGuideFinal_v1.1.pdf.]

Platnick, S., M. D. King, S. A. Ackerman, W. P. Menzel, B. A. Baum, J. C. Riédi, and R. A. Frey (2003), The MODIS cloud products: Algorithms and examples from Terra, IEEE Trans. Geosci. Remote Sens., 41(2), 459–473.

Platnick, S., S. Ackerman, M. King, G. Wind, K. Meyer, P. Menzel, R. Frey, R. Holz, B. Baum, and P. Yang (2015), MODIS Atmosphere L2 Cloud Product (06_L2), NASA MODIS Adaptive Processing System, Goddard Space Flight Center, USA: http://dx.doi.org/10.5067/MODIS/MOD06_L2.006.

Saito, M., Iwabuchi, H., Yang, P., Tang, G., King, M. D., and Sekiguchi, M. (2017). Ice particle morphology and microphysical properties of cirrus clouds inferred from combined CALIOP-IIR measurements. J. Geophys. Res., 122(8), 4440-4462.

Sassen, K.; Z. Wang, D. Liu (2008), Global distribution of cirrus clouds from CloudSat/Cloud-Aerosol Lidar and Infrared Pathfinder Satellite Observations (CALIPSO) measurements. J. Geophys. Res., 113, D00A12, doi:10.1029/2008JD009972.

Stephens, G. L., S. C. Tsay, P. W. Stackhouse, Jr., and P. J. Flatau (1990), The relevance of the microphysical and radiative properties of cirrus clouds to climate and climatic feedback, J. Atmos. Sci., 47(14), 1742–1754.

Sun, Wenbo, Norman G. Loeb, and Ping Yang. (2006), On the retrieval of ice cloud particle shapes from POLDER measurements. J. Quant. Spectrosc. Radiat. Transfer, 101.3: 435-447.

Tang, G., R. L. Panetta, P. Yang, G. W. Kattawar, and P. W. Zhai (2017), Effects of ice crystal surface roughness and air bubble inclusions on cirrus cloud radiative

properties from remote sensing perspective, J. Quant. Spectrosc. Radiat. Transfer, 195, 119–131.

Van Diedenhoven, B., B. Cairns, I. V. Geogdzhayev, A. M. Fridlind, A.S. Ackerman, P. Yang, and B. A. Baum (2012), Remote sensing of ice crystal asymmetry parameter using multi-directional polarization measurements–Part 1: Methodology and evaluation with simulated measurements, Atmos. Meas. Tech., 5.10: 2361-2374.

Varnai, T., A. Marshak (2007), View angle dependence of cloud optical thicknesses retrieved by Moderate Resolution Imaging Spectroradiometer (MODIS). J. Geophys. Res., 112, D06203, doi:10.1029/2005JD006912.

Várnai, Tamás, and Alexander Marshak. (2001), Statistical analysis of the uncertainties in cloud optical depth retrievals caused by three-dimensional radiative effects, J. Atmos. Sci., 58.12: 1540-1548.

Wang, C. X., P. Yang, A. Dessler, B.A. Baum, Y.X. Hu, (2014), Estimation of the cirrus cloud scattering phase function from satellite observations. J. Quant. Spectrosc. Radiat. Transf., 138, 36–49.

Wang, Y., P. Yang, S. Hioki, M. D. King, B. A. Baum, L. Di Girolamo, and D. Fu, (2019), Ice cloud optical thickness, effective radius, and ice water path inferred from fused MISR and MODIS measurements based on a pixel-level optimal ice particle roughness model. J. Geophys. Res., 124(22), 12126-12140. doi: 10.1029/2019JD030457

Wang, Y., S. Hioki, P. Yang, M. D. King, L. Di Girolamo, D. Fu, and B. A. Baum (2018), Inference of an optimal ice particle model through latitudinal analysis of MISR and MODIS data. Remote. Sens., 10(12), 1981, doi:10.3390/rs10121981.

Xie, Y., P. Yang, G. W. Kattawar, P. Minnis, Y. Hu, and D. L. Wu (2012), Determination of ice cloud models using MODIS and MISR data, Int. J. Remote. Sens., 33(13), 4219–4253.

Yang, P., and K. N. Liou (1998), Single-scattering properties of complex ice crystals in terrestrial atmosphere, Contr. Atmos. Phys., 71(2), 223–248.

Yang, P., K. N. Liou, L. Bi, C. Liu, B. Yi, and B. A. Baum (2015), On the radiative properties of ice clouds: Light scattering, remote sensing, and radiation parameterization, Adv. Atmos. Sci., 32(1), 32–63.

Yang, P., L. Bi, B. A. Baum, K. N. Liou, G. W. Kattawar, M. I. Mishchenko, and B. Cole (2013), Spectrally consistent scattering, absorption, and polarization properties of atmospheric ice crystals at wavelengths from 0.2 to 100 μm, J. Atmos. Sci., 70(1), 330–347.

Yang, P., S. Hioki, M. Saito, C. P. Kuo, B. A. Baum, and K. N. Liou (2018), A review of ice cloud optical property models for passive satellite remote sensing, Atmos., 499, doi:10.3390/atmos9120499.

Yang, P.; G. W. Kattawar, G. Hong, P. Minnis , Y. X. Hu, (2008), Uncertainties associated with the surface texture of ice particles in satellite-based retrieval of cirrus clouds—Part I: Single-scattering properties of ice crystals with surface roughness. IEEE Trans. Geosci. Remote Sens., 46, 1940–1947.

Yang, P., and K.N. Liou, (1998), Single-scattering properties of complex ice crystals in terrestrial atmosphere. Beiträge zur Physik der Atmosphäre (Contrib. Atmos. Phys.), 71, 223–248.

Yang, P., K.N. Liou, L. Bi, C. Liu, B. Yi, and B. A. Baum (2015), On the radiative properties of ice clouds: Light scattering, remote sensing, and radiation parameterization. Adv. Atmos. Sci., 32.1: 32-63.

Zeng, S., C. Cornet, F. Parol, J. Riedi, and F. Thieuleux (2012), A better understanding of cloud optical thickness derived from the passive sensors MODIS/AQUA and POLDER/PARASOL in the A-Train constellation, Atmos. Chem. Phys., 12(23), 11245–11259.

Zhang, Z., and S. Platnick (2011), An assessment of differences between cloud effective particle radius retrievals for marine water clouds from three MODIS spectral bands, J. Geophys. Res., 116, D20215, doi:10.1029/2011JD016216.

Zhang, Z., P. Yang, G. Kattawar, J. Riedi, L. Labonnote, B. Baum, S. Platnick, and H. L. Huang (2009), Influence of ice particle model on satellite ice cloud retrieval: lessons learned from MODIS and POLDER cloud product comparison, Atmos. Chem. Phys., 9(18), 7115–7129.

Zhang, Z. B.; A.S. Ackerman, G. Feingold, S. Platnick, R. Pincus, H.W. Xue (2012), Effects of cloud horizontal inhomogeneity and drizzle on remote sensing of cloud droplet effective radius: Case studies based on large-eddy simulations. J. Geophys. Res., 117, D19208, doi:10.1029/2012JD017655.